NNT: 2016SACLV068

PH.D THESIS

ȘTEFAN CEL MARE UNIVERSITY OF SUCEAVA AND PARIS-SACLAY UNIVERSITY
ELABORATED AT FACULTY OF ELECTRICAL ENGINEERING AND COMPUTER SCIENCE AND AT SAINT QUENTIN EN YVELINES UNIVERSITY OF VERSAILLES

DOMAIN: COMPUTERS AND INFORMATION TECHNOLOGY

BY

CĂTĂLIN MARICEL JURESCHI

SUBJECT:

TEMPERATURE AND PRESSURE SENSORS BASED ON MOLECULAR SPIN TRANSITION MATERIALS

Supervisors:
Prof. Yasser ALAYLI
Prof. Jorge LINARES
Prof. Corneliu Octavian TURCU

NNT: 2016SACLV068

THÉSE DE DOCTORAT
DE
L'UNIVERSITÉ PARIS-SACLAY ET DE L'UNIVERSITÉ ŞTEFAN CEL MARE
PREPARE A L'UNIVERSITE DE VERSAILLES SAINT QUENTIN EN YVELINES
ET LA FACULTÉ DE GÉNIE ÉLECTRIQUE ET SCIENCES INFORMATIQUES

SPÉCIALITÉ: AUTOMATIQUE

PRÉSENTÉE PAR

CĂTĂLIN MARICEL JURESCHI

SUJET:

CAPTEURS DE TEMPÉRATURES ET DE PRESSION A BASE DES MATÉRIAUX MOLÉCULAIRES A TRANSITION DE SPIN

Présentée et soutenue publiquement le 27 Septembre 2016

Devant le jury composé de:

Prof.	Yasser ALAYLI	Université Paris Saclay, UVSQ	Directeur de thèse
Prof. Ass.	Cristian ENĂCHESCU	Université Alexandru Ioan Cuza, Iaşi	Rapporteur
Prof.	Yann GARCIA	Université Catholique de Louvain, Louvain-la-Neuve	Président
Prof.	Jorge LINARES	Université Paris Saclay, UVSQ	Co-directeur de thèse
Prof.	Daniel MOGA	Université Technique, Cluj Napoca	Rapporteur
Prof. Ass.	Vlad MUREŞAN	Université Technique, Cluj Napoca	Examinateur
Prof. Ass.	Aurelian ROTARU	Université Ştefan cel Mare, Suceava	Examinateur
Prof.	Corneliu Octavian TURCU	Université Ştefan cel Mare, Suceava	Co-directeur de thèse
Prof.	Kamel BOUKHEDDADEN	Université Paris Saclay, UVSQ	Invité
Prof.	Pierre Richard DAHOO	Université Paris Saclay, UVSQ	Invité

To my family,
with all my love

Acknowledgements

Firstly, I would like to thank to Prof. Jorge Linares and Assoc. Prof. Aurelian Rotaru for their guidance and patience, for all the time they devoted to me, for their confidence in me and for always motivating me.

My deepest gratitude goes to Professor Yasser Alayli and Professor Corneliu Octavian Turcu for their support, for their advice and flexibility they granted for my research.

With great pleasure I wish to express my gratitude to Prof. émérites Jamil Nasser for his guidance, support and advice and for always motivating me towards improving my technical knowledge.

I am also grateful to Prof. Yann Garcia, Assoc. Prof. Cristian Enachescu, Prof. Daniel Moga and Assoc. Prof. Vlad Mureșan who kindly reviewed this work and accepted to be part of my thesis committee.

I thank all my articles coauthors and especially Prof. Pierre Richard Dahoo, Prof. Kamel Boukheddaden and Dr. Eng. Daniel Chiruta for their fruitful scientific collaboration. I would also like to thank the researchers from ONERA, Dr. Eng. Michel Parlier and Eng. Marie Hélène Ritti, for the fruitful collaboration.

Special thanks to the Chiruta family who assisted and supported me throughout my time spent at Versailles.

I would like to acknowledge the CNCS—UEFISCDI, the research center MANSiD and CHAIR Materials Simulation and Engineering (UVSQ) for their financial contribution.

I want to thank my colleagues from the Faculty of Electrical Engineering and Computer Science from Suceava: Dr. Ionela Rusu, Dr. Andrei Diaconu, Lucian, Constantin, Alin and Simona and to my colleagues from LISV laboratory: Nhat, Moustafa, Amos, Walid and Sidou.

Last but not least, I would like to truly thank my family for their confidence in me and support through both good and difficult times. I want to express my deepest gratitude to my wife, Ioana, for her infinite patience and her unconditional love. Thank you for staying by my side when I was at my lowest and for sacrificing our time so that I could focus on my research.

Résumé

Mots-clés: capteurs, matériaux moléculaires, transition de spin, Monte Carlo Entropic Sampling

Cette thèse concerne les études théoriques et expérimentales de composés à transition de spin (SCO: “spin crossover compounds”) menées pour déterminer la possibilité de les implémenter dans des capteurs de température et/ou de pression. L’analyse théorique a été effectuée en utilisant les deux modèles les plus utilisés dans ce domaine de recherche notamment: le modèle équivalent d’Ising et le modèle de couplage Atom-Phonon. Pour générer les états des systèmes SCO, les méthodes d’échantillonnage entropique de Monte Carlo (MCES: «Monte Carlo Entropic Sampling») et de Monte Carlo Metropolis (MCM) ont été utilisées. La méthode MCES a été utilisée pour étudier les systèmes à basse dimensions réduites et la méthode MCM pour les systèmes de grande taille. Ainsi le rôle de la coopérativité dans un système SCO a été analysé et l’influence des interactions des molécules de surface avec leur environnement local a été étudiée. Il a été montré qu’une transition procédant par plusieurs étapes (« multi step transition ») est pilotée par trois types d’interactions: celles à courte portée, celles à longue portée et celles entre les molécules de surface avec leur environnement. Ces résultats peuvent être utilisés pour assembler les matériaux de type SCO dans des dispositifs technologiques parce-que, comme il a été montré, il est nécessaire de tenir compte des interactions qui peuvent exister entre les molécules de surface et leur environnement. De plus, des résultats importants ont été obtenus en analysant le rôle de l’architecture du système. En considérant des systèmes ayant le même nombre de molécules, il a été montré qu’un système de forme carrée présente un caractère plus coopératif qu’un système de type échelle qui à son tour présente un caractère plus coopératif qu’un système de type chaîne.

Les résultats obtenus en appliquant le modèle de couplage Atom-Phonon ont été comparés en utilisant trois méthodes différentes pour résoudre le Hamiltonien du système: l’approximation du champ moyen, la matrice dynamique et l’approximation parabolique. Ainsi il a été montré que la méthode de l’approximation parabolique est meilleure que la méthode de l’approximation du champ moyen et que les résultats obtenus avec cette méthode sont très proches de ceux obtenus avec des calculs exacts. Ceci est du au fait que cette méthode est très proche de la méthode de calculs exacts.

Les études expérimentales des composés SCO $[Fe(hyptrz)]A_2 \cdot H_2O$ et $[Fe(hyetrz)_3]I_2 \cdot H_2O$ ont révélées leur propriété thermo- et piézo-chromique. Une grande variété de techniques a été employée pour la caractérisation des deux composés. Ainsi les analyses thermiques du premier composé sous l’action d’une pression externe ont été réalisées avec une cellule de pression à gaz. Ce type de cellule a l’avantage de maintenir le caractère hydrostatique sur le domaine entier de température. Le deuxième composé a été caractérisé en utilisant des techniques telles que: caractérisation optique, DSC, spectroscopie Mössbauer et un dispositif micromécanique pour l’application de la pression. Les résultats ont démontré la faisabilité de détection de la pression en utilisant un capteur ou marqueur basé sur un composé SCO fonctionnant à température ambiante. Pour le composé SCO $[Fe(hyetrz)_3]I_2 \cdot H_2O$, une valeur seuil de la pression de contact autour de 30 MPa a été obtenue qui induit de manière irréversible un changement de couleur du matériau moléculaire. Ceci résulte de la transition de l’état HS vers l’état BS. De plus, la possibilité d’une transition qui induit un changement de couleur en sens inverse en utilisant un autre stimulus (température) a été démontrée, ce qui permet de réutiliser le capteur.

A partir de ces résultats, un nouveau type de capteur fonctionnant sur le principe d'une détection optique a été proposé qui permettrait la détection concomitante à la fois de la température et de la pression. Ce nouveau type de capteur est basé sur deux composés SCO qui sont caractérisés par des transitions progressives. En considérant les développements récents dans le domaine SCO cet objectif pourrait être très bientôt atteint.

Abstract

Keywords: sensors, molecular materials, spin transition, Monte Carlo Entropic Sampling

This thesis is result of theoretical and experimental studies on spin crossover compounds (SCO) with the purpose of implementing them in temperature and/or pressure sensors. The theoretical analysis was performed using two of the most employed models in the field namely: the Ising-like model and the Atom Phonon coupling model. For generating the states of SCO systems the Monte Carlo Entropic Sampling (MCES) and Monte Carlo Metropolis (MCM) methods were used. The MCES method was used for small systems and the MCM method for large systems. Thus, we analyzed the role of cooperativity of a SCO system and studied the influence of interactions of the surface molecules with their local environment. We have shown that behind a multi-step transition there are three types of interactions: the short-range interactions, long-range interactions and interactions of surface molecules with their environment. These results are applicable in the construction of SCO materials based devices because, as we have shown, it is necessary to account for the interactions that may occur between the molecules on the surface and their environment. Moreover, important results were obtained by analyzing the role of system's architecture. Considering equal number of molecules systems, we have shown that a square system is more cooperative than a ladder type system which in turn is more cooperative than a chain-type system.

The results obtained using the Atom-phonon coupling model were compared using three different methods to solving the Hamiltonian system: mean field approximation, dynamic matrix and parabolic approximation. Thus it was shown that the parabolic approximation method is better than that of the mean field approximation method and that the results obtained by this method are very close to reality. This is because this method uses exact calculation.

The experimental studies on SCO compounds $[Fe(hyptrz)]A_2 \cdot H_2O$ and $[Fe(hyetrz)_3]I_2 \cdot H_2O$ revealed their thermo- and piezo-chromic character. A variety of techniques have been employed for the characterization of the two compounds. Thus the thermal analysis of the first mentioned compound under the action of external pressure was carried out using a gas pressure cell. This type of cell has the advantage of maintaining the hydrostatic character over the entire range of temperature. The second compound was characterized using techniques such as: optical characterization, DSC, Mössbauer spectroscopy and a micromechanical home-made device for the application of pressure. The results demonstrated the feasibility of pressure detection using a molecular spin crossover based sensor/marker operating at ambient temperature. For the SCO compound $[Fe(hyetrz)_3]I_2 \cdot H_2O$, we obtained a threshold value of the contact pressure of about 30 MPa to irreversibly induce the color change of the molecular material, due to the spin state switching form HS to LS state. Moreover, the possibility of switching back the color using another stimulus (temperature) was demonstrated, making this sensor reusable.

Taking into account the above mentioned results we proposed a new type of sensor with optical detection that would allow the concomitant detection of both temperature and pressure. This new type of sensor is based on two SCO compounds that exhibit gradual transitions. Considering recent developments in the SCO field this objective could be achievable in the near future.

Table of Contents

Table of Figures

Introduction

In the broadest definition "sensor converts input signals of a physical nature into electrical output" [1]. If up until a few years ago sensors were being used for prevention purposes, today's sensors have become core elements in automation systems a sensor can perform while in operation. We can divide them into four general categories as follows:

- Monitoring, controlling and adjusting the system to increase performance;
- Security and alarm in order to enhance system security and to anticipate possible miscues;
- Diagnostics and analysis in order to better understand the operation of the system and find ways to improve it;
- Interface and navigation in order to increase functionality.

Nowadays the most used types of sensors are: transducers, functional sensors and smart sensors. Intelligent sensors distinguish themselves from other types of sensors due to their extra conditioning process control, digital interface and operating system.

It's hard to imagine today's world without automated equipment. From mobile phones, computers or washing machines to cars and airplanes, all contain sensors that make our lives easier and safer. In fact, there are no industrial areas which operate without measuring, testing, monitoring and automation. In all branches of the industry sensors are widely used to automate the production process. With the aid of sensors, the production capacity has been greatly improved and is continuously growing. This is also due to the particular concern, seen in recent years, regarding minimizing energy consumption, miniaturization, easy handling, automation and multiple use of all electronic equipment. In this respect, electronic equipment manufacturers as well as science research groups are constantly working to meet the desideratum. Special consideration is given to the development and optimization of various types of sensors with increased sensitivity and higher technical characteristics, due to the ever growing demand on the electronics market. In this high-tech field Europe, and especially Germany, holds a leading global position, not only in terms of technological standards but also in terms of global market shares. A comparison between commercial studies [2,3] in terms of demand and the results of surveys conducted by the Association for Sensors and Measurement (AMA) [4] on the sensor suppliers market, shows that European suppliers cover about 35 % of the global demand for sensors. The AMA [5] estimates that around 1000 industrial sensors manufacturers are located in Europe as compared to 3000 worldwide.

The continuous development of intelligent electronic devices has led to a significant increase in sensors demand on the market. Fingerprint reader mobile phones and/or the differentiation in tactile pressure on touch screen phones are increasingly being used and evolving. It is expected that, in the near future, handsets will have built in spectrometers in order to measure produce freshness. 8-core processors with 14 nm manufacturing technology and graphics cards with thousands of microprocessors are increasingly being found in computers marketed in recent years.

In 2012, INTECHNO CONSULTING in a report of 1520 pages [6] concerning the sensor elements, sensor modules, sensors and sensor systems, has reported an annual growth rate of non-military world market for sensors of 7.9% between 2006 and 2011 with a worldwide market sensors of 81.6 billion euros in 2006 increasing at 119.4 billion euros in

2011 and forecasted at 184.1 billion euros by the end of 2016. In this report a slight decrease in the percentage of Europe's sensors market in 2016 is noted in Figure 1.

The market for sensor technology is highly heterogeneous and difficult to break down even for those directly involved. However, a noticeable shift from the market for capital goods to the consumer goods market is being observed, with increasing emphasis on the final products. Therefore, the consumer end products sensor market has, in general, a faster growth rate than the measurement focused products and control technologies. New applications, at considerable growth rates, are being found in domestic equipment, safety and security tools, diagnostic and therapeutic medical equipment and automotive engineering. The highest growth rates are being recorded for image sensors, acceleration sensors, pressure sensors, position and proximity sensors as well as biochemical sensors [7]. The use of these sensors on an ever larger scale has resulted in a reduced price and stimulated the increase in production of sensors. A graph of the sensor market developments in the past 10 years is shown in Figure 2. It can be seen that the market grew by 6.3% on average each year albeit with a significant decline in 2008-2009 due to global crisis.

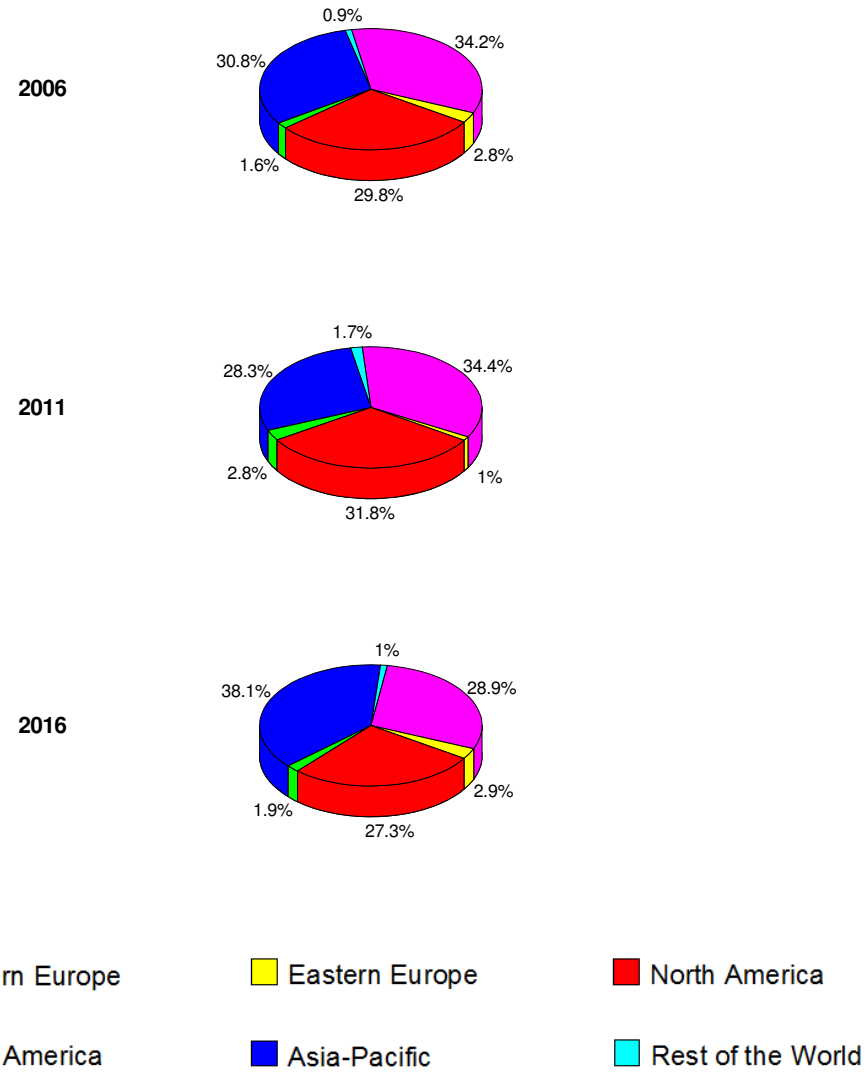

Figure 1 Analysis and Forecast of the World market of sensors until 2016: subdivision by regions [6]

SensorsPortal has published an estimation of sensors market evolution for the next 5 years [8]. The global sensors market is expected to grow from 95.3 billion dollars in 2015 to 154.4 billion dollars by 2020 with an annual growth rate of 10.1% for a period of 5 years, between 2015 and 2020. The growth rate of image, flow and level sensors is expected to increase by 11.7% over the next five years and go from 25.6 billion dollars in 2014, 28.9 billion dollars in 2015 to almost 50.2 billion in 2020. Chemical sensors and bio-sensors, an important segment of the sensor market, is expecting to grow in 2015 to 19 billion dollars. With a growth rate of 11.5%, analysts anticipate a growth to nearly 32.8 billion dollars in 2020. Intelligent sensors market is expected to grow to 10.46 billion dollars in 2020, a 36.25% growth rate from 2014 to 2020. US made sensors market, with a 30% growth rate, is expected to reach 438 million dollars by 2018. An important role in maintaining the stability of this segment of activity is reinvestment by the industry of 10% of its turnover in research, innovation and development.

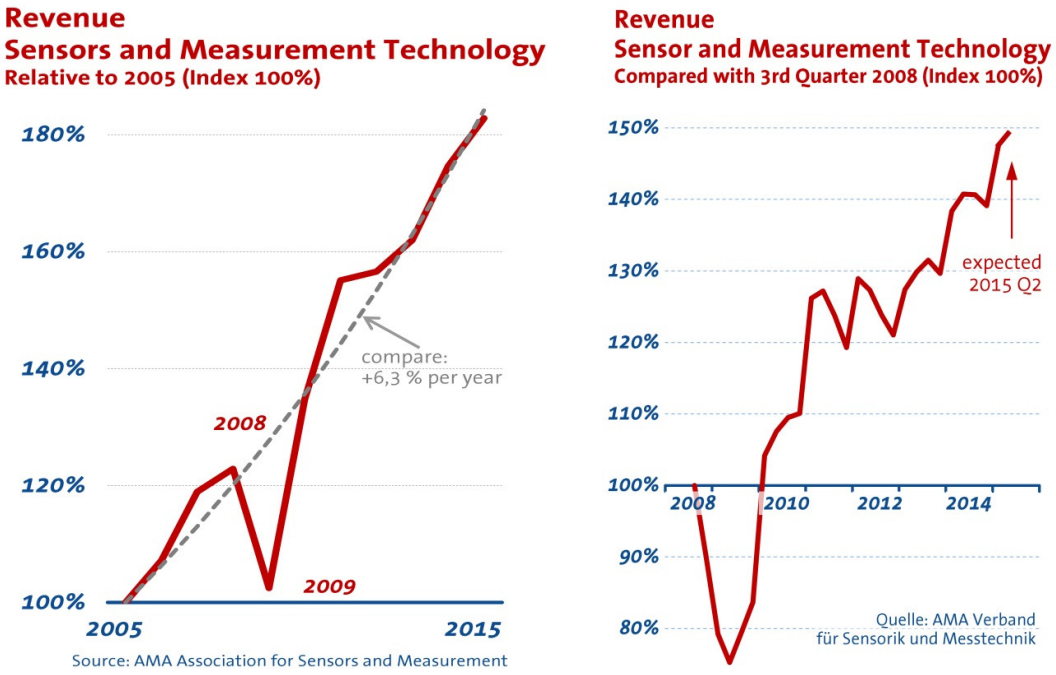

Figure 2 The evolution of sensors market [9]

Depending on the clasification criteria of sensors, start from very simple to very complex sensors. Thus, depending of the errors of measurement, the sensors are classified by deviation and resolution. Other classification criteria for classification sensors are after specifications (price, size, weight, stability, linearity, resolution, switching signal, ...), material (organic, inorganic, conductor, insulator, ...) phenomenon of conversion (thermoelectric, piezoelectric, photoelectric, fotomagnetic, magneto, Termoopt, fotoelastic, electroelastic, chemical, biological, ...), scope (agriculture, construction, automotive, military, marine, ...) stimuli (acoustic biological, chemical, electrical, magnetic, optical, mechanical, thermal, piezo, ...).

An important category of sensors are temperature sensors. These sensors vary from very simple, thermostatic on / off used in domestic devices (eg. water heater) to the semiconductor sensor with a high sensitivity used in complex processes (eg. the control of furnace plant). Also, these sensors can be divided into two basic types:

- sensors which require contact with the object whose temperature it is desired to monitor and are called contact temperature sensors;

- sensors which use convection and radiation to monitor temperature change and are called non-contact sensors.

In turn, these two types of sensors can be subdivided in other basic types: thermocouples, resistive temperature sensors (RTDs - resistance temperature detectors, thermistors), infrared, bimetallic, sensors with liquid dilator, sensors that changes its molecular state and silicon diodes.

Due to its simplicity, the thermocouple is the most common temperature sensor used in the industry. Easy to use, with a rapid response to temperature change, small size, stability [10-12] and a temperature range from -2000^{o}C to + 26000^{o}C, thermocouple consists of two junctions of dissimilar metals joined at one end. The operating principle of the thermocouple is based on direct thermoelectric effect (Seebeck effect). It consists in the appearance of a tensions termoelectromotoare in a closed circuit consisting of two different semiconductors when contacts are maintained at different temperatures.

Resistive temperature sensors are best suited to make accurate and repeatable temperature measurements. RTDs are manufactured from metals whose resistance increases with temperature. This resistance is directly proportional to the length of the metal wire and inversely proportional to the cross-sectional area and increases linearly with temperature. Made from high purity materials (platinum, copper, nickel), RTD's are temperature sensors with a precise and fast response [13]. Operating temperature range of RTD's is between -2000^{o}C to + 6000^{o}C.

The same mode of operation of the RTD's, thermistors are resistive temperature sensors manufactured from solid semiconductors [14] having a positive or negative temperature coefficient. Most used thermistors have a negative temperature coefficient (NTC) which means that the resistance value decreases with increasing temperature. Compared with RTD's and thermocouples, thermistors are weaker in construction and require more attention during installation to prevent crushing.

In the bimetallic devices, two metals with different thermal properties are soldered back to back. When heated, a part of the bimetallic strip deform more than the other. The main advantage of bimetallic devices is portability. Also, another advantage is independence from a power source. As disadvantage, the bimetallic devices are not accurate as the electronic devices. These devices are used in applications "ON / OFF" or "OFF / ON".

Specially manufactured for use in cryogenic temperature ranges, the silicon sensors have good conductivity and linearity in this temperature region. With increased robustness the silicon sensors are designed for repeatable measurements with good accuracy in temperature ranges between 1.4K and 500K [15]. This type of sensor is suitable for use in very high magnetic fields or in radiation medium [16].

Other important sensors are pressure sensors. A pressure sensor can generate an analog output proportional to pressure at it is or has a switching output operating at a predetermined pressure. Depending on the activity, the pressure sensors are classified as follows: vacuum sensors, sensors for medium pressure (10^2 Pa - 10^8 Pa) and sensors for high pressure (> 10^8 Pa) [17]. The most used sensitive elements to measure pressure are embedded diaphragm, plunger with spring, corrugated diaphragm, manometer open cell, closed cell manometer, biconical cell, bellows, Bourdon tube, twisted helical tube, one-eyed tube. The high pressures are measured using the following conversion types: piezoelectric effect and electromechanical oscillator. Sensors that use piezoelectric principle have the advantage of being robust, dynamic and with a response time of milliseconds. Stability and high precision sensors show using electromechanical oscillator principle but require numerical corrections which involve a microprocessor.

Major problems arise when desired to measure the cryogenic or high temperatures at very high pressures. These problems occur due to changes in the properties of materials used in sealing systems. Using sensors that require removal of supply wires and / or of output signals makes it difficult to seal the system and increase the cost of production. The temperature and pressure measurement in hazardous areas is also a problem. A solution to these problems would be to use optical detection sensors. Thus, the problems to sealing wires or the need to introduce the energized wires in explosive environments disappear.

Decrease energy consumption and miniaturization are other requirements of the consumer market. All these requirements and problems can only be solved by developing new materials with significantly improved physical properties. Materials with spin transition (ST), due to the physical differences between their two states, such as different colors, different volume or different electrical conductivity, have captured the attention of many research groups and large companies involved in research. The ever growing interest in these materials is due to their high applicability potential in areas such as temperature and/or pressure sensors, information storage, micro switches and displays.

The purpose of this thesis is to offer new insight regarding the spin transition phenomenon from both points of view theoretical and experimental. Thus, in the first section of **Chapter 1** an introduction in SCO materials and the main perturbation factors that induce the spin transition is presented. In the second part of this chapter the main models and techniques used in characterization of behaviors of these interesting materials are presented.

In **Chapter 2** we describe the behaviors of some SCO compounds and their optical proprieties in the HS and LS states. So, taking into account the different colors of the two states, in the second part of this chapter, new proposed types of sensors involving SCO compounds, are presented. To understand how the behavior can be influenced by the external perturbation factors, architecture or internal interactions, in **Chapter 3**, using the Ising like model [18-20], a theoretical study concerning of these main factors that determine the evolution of SCO behavior is presented. Also, in this chapters, the influence of short and long interactions together with the architecture effect are studied. A new term is introduced in order to account for the interaction of edge molecules with their local environment and simulations were performed to investigate the influence of temperature and pressure.

In **Chapter 4,** using the Atom-phonon coupling model a theoretical analysis of spin crossover nanochains using a parabolic approximation was performed. It is well known that, apart from the system's cooperativity, which influences the hysteretic behavior of SCO complexes, the size of the system also plays a determinant role. The properties of the system are analyzed using a parabolic algorithm as a new method proposed in order to take into account the phonon contribution. Based on exact calculations, this method is more realistic and more efficient than the mean-field approximation (MFA). In particular, both the parabolic algorithm and the dynamic-matrix method are tested and compared and the analysis of the system's behavior shows that large size systems can be treated without generating all the system states. We also analyzed the role of degeneracy, and the thermal variation of both the entropy and heat capacity in the ferromagnetic-like coupling case. These studies play an important role in the choice process of SCO compounds for the desired application.

To highlight the temperature and pressure influence on SCO behavior, in **Chapter 5** we present an experimental analysis of $[Fe(hyptrz)]A_2 \cdot H_2O$ and $[Fe(hyetrz)_3]I_2 \cdot H_2O$ SCO compounds. If for first compound a gas pressure cell was used to illustrate the thermal behavior at different pressures, for the second compound a home-made micromechanical device was used to analyze the pressure influence. The study is accompanied by a theoretical study in the framework of the Ising-like model allowing us to predict the bistability region of these two SCO compounds pertaining to sensor applications. In the end of this chapter, a new type of sensor involving two SCO compounds is proposed. This type of sensor is able to

simultaneously indicate both temperature and pressure at which it is. It is very important to mention that for the fabrication of this sensor type, two SCO materials that exhibit a gradual transition without hysteresis are required.

The manuscript ends with general conclusions and perspectives.

References

[1] J. Fraden, Handbook of Modern Sensors, Springer, 2010.
[2] N. Schroeder, Intechno Consulting Basel (1999).
[3] Decision Etudes Conseil: European Sensor Industry: Technology, Market and Trends 2007-2011 Paris (2008).
[4] AMA Fachverband für Sensorik e.V.: Branche/Wirtschaftliche Bedeutung, http://www.ama-sensorik.de (2010).
[5] A.-A.f.S. Technology, Sensor Trends 2014. http://www.ama-sensorik.de/fileadmin/Pubikationen/AMA_Study_Sensor_Trends[1].pdf, 2014.
[6] N. Schroeder, INTECHNO CONSULTING (2012).
[7] E. Suhir, Springer 2 (2007) 203.
[8] S. Portal. http://www.sensorsportal.com/DOWNLOADS/Media_Planner_2015.pdf, 2015.
[9] A.f.S.T.-. AMA, http://www.ama-sensorik.de/en/association/sector-information/quarterreports-2015/.
[10] H.J. Brown-Shaklee, P.A. Sharma, J.F. Ihlefeld, Journal of Materials Science 50 (2015) 5005.
[11] S. Konstantopoulos, M. Tonejc, A. Maier, R. Schledjewski, J. Reinf. Plast. Compos. 34 (2015) 1015.
[12] D. Kretschmer, J. Odgers, A.F. Schlader, Journal of Engineering for Power 99 (1977) 1.
[13] J.D. Goedel, Fast-responding resistance temperature detector (RTD) assembly for various locations such as inlet air in gas turbine engine has thin-walled RTD unit and support structure that minimizes contact with housing to minimize conduction error. UNISON IND LLC (UNIS-Non-standard), p. 27.
[14] P. Park, D. Ruffieux, K.A.A. Makinwa, Ieee Journal of Solid-State Circuits 50 (2015) 1571.
[15] http://www.lakeshore.com/products/cryogenic-temperature-sensors/silicon-diodes/dt-670/pages/Specifications.aspx.
[16] http://www.cryocon.com/S900/S900ds.pdf.
[17] Modern sensors handbook, ISTE, London W1T 5DX, UK and Newport Beach, CA 92663 , USA, 2007.
[18] J. Wajnflasz, R. Pick, J. Phys. Colloques 32 (1971) C1.
[19] A. Bousseksou, J. Nasser, J. Linares, K. Boukheddaden, F. Varret, Journal De Physique I 2 (1992) 1381.
[20] J. Linares, H. Spiering, F. Varret, European Physical Journal B 10 (1999) 271.

Chapter 1

State of the art

Contents

1 State of the art

1.1 Introduction

Sensors market growth is a consequence of the ongoing development of new equipment and devices that must meet the increasingly stringent requirements of the end user. From miniaturization, multi-functionality and low power consumption, to applications that require high performance computing are some of the criteria in mind of the user when purchasing the desired product. Size reduction of electronic components has led to an increase in production costs due to the expensive equipment and costly components used in production. This is one of the reasons why, in recent years, miniaturization of electronic components reached the economic limit due to production costs. This is associated with the limiting issue in the miniaturization of components due to physical phenomena that occur when the material reaches a critical minimum size. Continuous technological development has led many research groups, including physicists, chemists and engineers, as well as companies to develop new materials with far superior physical properties which can be controlled at the molecular level [1-4]. Implementation of these materials in devices at both the macroscopic level and at the single molecule one, can be done only after a deep comprehensive understanding of the physical and chemical properties of the material. The use of these materials in the manufacturing process of electronic components should result in a reduction of the size of the components by orders of magnitude.

In this context, over the recent years, chemists have developed new techniques for the synthesis of molecular compounds with unique properties. An important category of multifunctional molecular compounds are the spin transition compounds (SCO) that attracted the attention of many research groups because of their potential applications [2,5-9]. First observed in the early 30s by L. Cambi and L. Szego, while studying the temperature dependence of magnetic susceptibility in molecular compounds containing Fe (III) ($3d^5$) centers [10], the phenomenon of spin transition (ST) was later discovered in other compounds containing metallic centers with $3d^4$-$3d^7$ electronic configuration, such as: Fe (II) [11-13], Co (II) ($3D^7$) [14-17], Co (III) ($3d^6$) [18-20], Mn (II) ($3d^4$) [21,22], Mn (III) ($3d^5$) [23-26], Cr (II) ($3d^4$) [27-29]. These materials have a special particularity which is to switch between two stable magnetic states: a diamagnetic low spin state (LS) and a paramagnetic high spin state (HS). The two spin states are characterized by different physical properties such as different colors, different volumes or different electrical conductivities [30-32].

The most studied spin transition compounds so far have as a central ion Fe (II) in an octahedral configuration. The five orbitals of the Fe (II) ion are divided into two subsets [33,34]. A set consisting of t_{2g} (d_{xy}, d_{yz}, d_{zx}) orbitals and the second set consisting of two others e_g orbitals $\left(d_{z^2}, d_{x^2-y^2}\right)$ with an energy higher than the t_{2g} orbitals energy (Figure 1.1). Depending on the strength value of crystal field, represented by the energy gap of the levels t_{2g} and e_g, denoted by δ (10Dq) and the value of the electron pairing energy, Π, the six electrons can occupy the two different groups of orbitals, corresponding to the two following cases: (i) if the ligand field, δ is greater than the pairing energy, Π, $\delta>\Pi$, in violation of Hund's law, the electrons occupy the lowest energy orbitals, t_{2g}. In this case the sum of the spins is minimum (S = 0) and the compound will be in the LS state. For the second case, when $\delta<\Pi$ following Hund's law, electrons will occupy a number of orbitals as high as possible and the sum of the spins is maximum (S = 2), and the compound is in the HS state (Figure 1.2). The transition from one state to another is also characterized by a change in the volume of the molecule, due to the metal-ligand length change, this one being longer in the HS state than in the LS state. The spin transition phenomenon, represented by the transition

from one spin state to the other, occurs when the values of the two energies are approximately equal, $\delta \approx \Pi$.

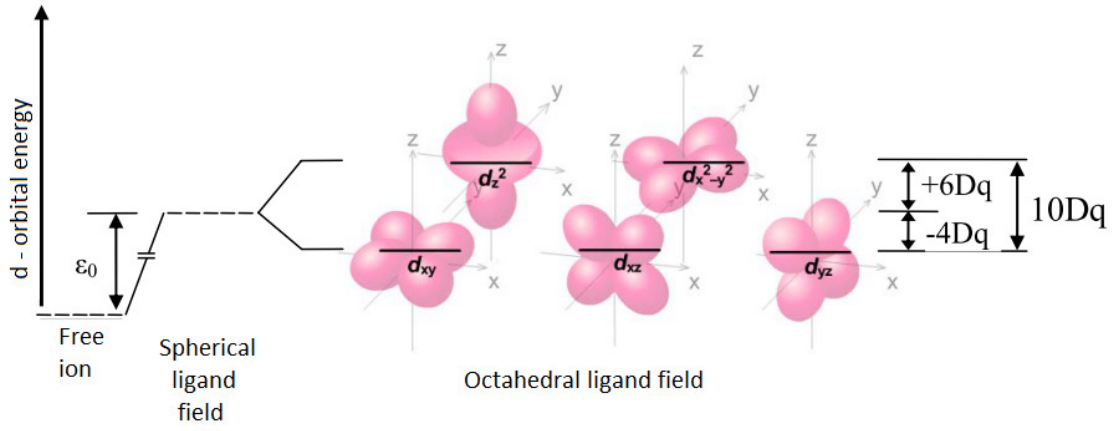

Figure 1.1 Representation of the five 3d orbitals.

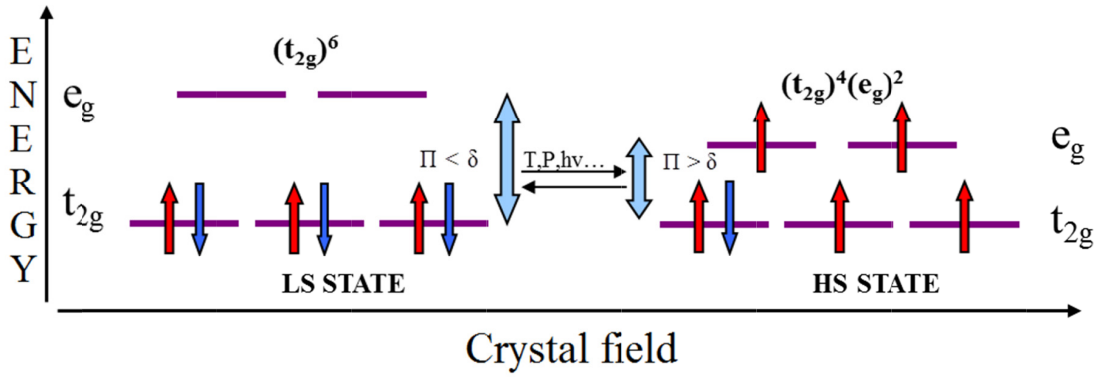

Figure 1.2 Electronic diagram of the HS and LS state for a Fe(II) ion in an octahedral ligand field.

Thus, under the action of external stimuli (temperature variation, pressure variation, applied magnetic or electric fields [2,35-37], light irradiation, etc.), the transition occurs between the diamagnetic LS state and the paramagnetic HS state or vice versa and is typically accompanied by significant changes in color, volume, magnetic state or electrical conductivity of the compound. These changes in physical properties can be observed using different characterization techniques such as: magnetic susceptibility measurements [13,38,39], Mossbauer spectroscopy [40], X-Ray diffraction [41-43], infrared and UV-vis spectroscopy [44,45] Raman spectroscopy [46], calorimetry [47-49], diffuse reflectance [7,50-52], ellipsometry [53,54] or optical microscopy [55].

1.2 The spin transition induced by temperature

One of the most used physical perturbations in order to induce the spin transition is the temperature. Depending on the type and intensity of the interactions between molecules, spin transition compounds may show different magnetic behavior with temperature variation (Figure 1.3): gradual or abrupt [56], two [57-61] or multi-steps [62-64], complete or incomplete [49,65] transitions, with or without hysteresis. The gradual transition is specific to systems characterized by very weak intermolecular interactions or to diluted systems with non-active impurities. Experimentally, for the first time, the two step ST in 1D coordination polymers was observed on the compound $[Fe(NCS)_2(bdpp)]$, (bdpp = 4,6-bis(2',2''-pyridyl)pyrazine) with its selenium analogues $[Fe(NCS)_2(bdpp)]$ and was attributed to the presence of two different crystallographic sites [66]. With a wide plateau (HS-LS) the two step ST was observed in [67,68]. The synergistic effect between intramolecular interactions favoring the mixed-spin state and intermolecular interactions favoring like-spin species domains are on the origin of two step transition in the binuclear iron(II) compound $[Fe(bt)(NCS)_2]_2(bpym)$, (bt = 2,2-bi-2-thiazoline; bpym = 2,2'-bipyrimidine) [57].

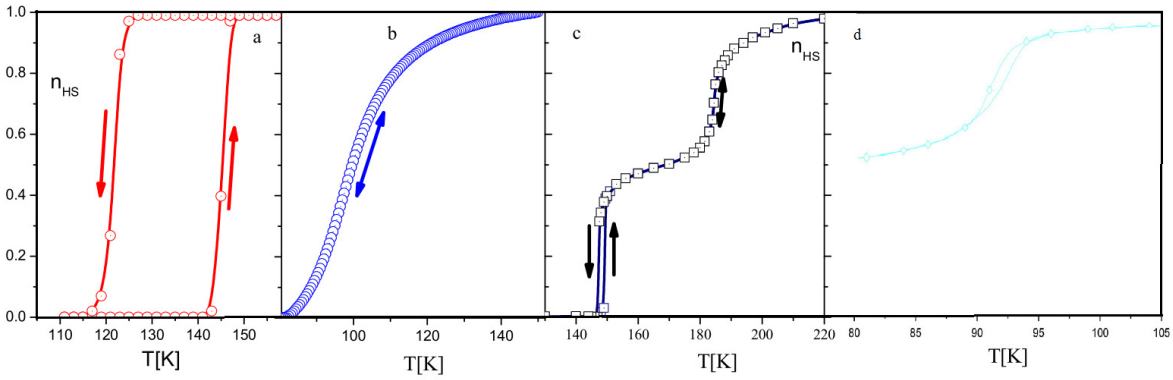

Figure 1.3 Various types of thermal induced spin transition: a) with hysteresis, b) gradual, c) two steps transition, d) incomplete [65,69]

1.3 The spin transition induced by pressure

A second main external perturbation that has been used to induce the spin transition is the application of an external pressure. In 1969 Ewald *et al.* [70] reported the first study on the pressure effect on the spin transition compounds (CTS). The study was carried out on a Co(II) based compound in solution. A few years later Bargeron *et al.* [71] and Slichter *et al.* [72] showed that, by applying an external pressure, the transition temperatures are shifted to higher temperatures, with shifts of about 15-20K/kbar. The research group led by Prof. Varret from Versailles had an important contribution to this topic [73].

From Figure 1.4 it can be seen that, by increasing the applied pressure the metal-ligand distance decreases resulting in the increase of the ligand field energy, Δ, and a decrease in the activation energy E_a. The transition from the LS state to the HS state occurs when the ligand field energy becomes greater than the energy of electron pairing. By applying an external pressure the volume of the molecule is decreased thus favoring the LS state.

CTS behavior under pressure is usually reversible [6,73]. However, in some cases, following the release of pressure the compound no longer returns to its initial state [74,75]. Applying pressure can cause irreversible changes in the electronic structure of the compound as well as in the crystallographic structure [72,76].

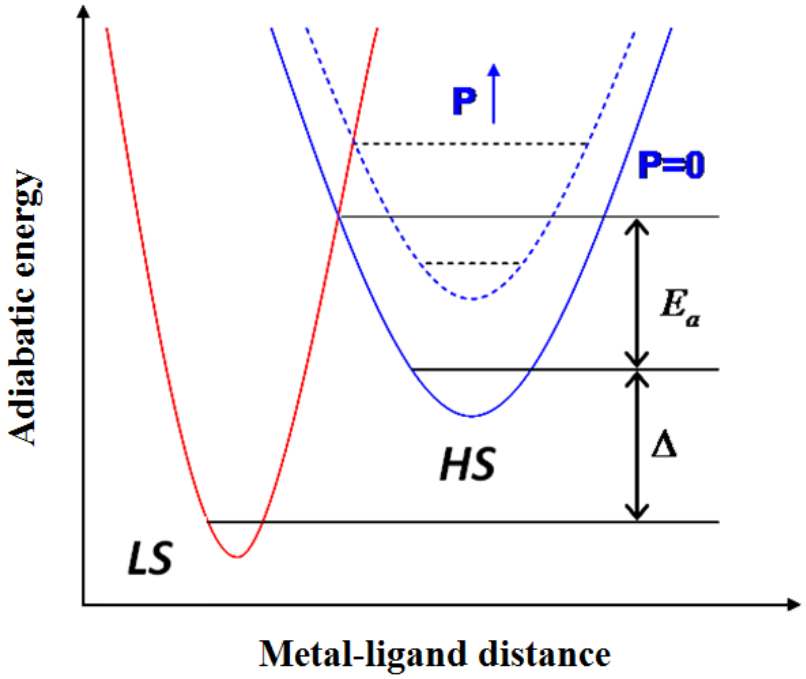

Figure 1.4 Schematic representation of the pressure influence.

Using hydrostatic pressure cells in conjunction with the SQUID, Mossbauer or optical systems for measuring optical reflectivity constitute the main types of characterization of the thermal and piezo behaviors of CTS [6,77-79].

1.4 Light induced spin state change

1.4.1 Light Induced Excited Spin State Trapping (LIESST)

By irradiating a Fe (II) based complexes in liquid phase, $Fe(biz)_3(ClO_4)_2$, $Fe(ppa)_2(ClO_4)_2$ and $Fe(pyimH)_3(BPh_4)_2$, (biz = 2,2'-bi-1,4,5,6-tetrahydropyrimid- ine; ppa = N^2-(2-pyridylmethy1)picolinamidine; pyimH = 2-(2-pyridylimidazole)), with a 530 nm wavelength light, McGarvey *et al.* [80] were able to disrupt the equilibrium between the two spin states. Two years later, in 1984, Decurtins *et al.* [81], by irradiating the $[Fe(ptz)_6](BF_4)_2$ (ptz = 1-propyltetrazole) compound in the solid state with green light (λ = 514 nm) at 20K, were able to induce a transition from the LS state to a HS state which was maintained for more than 10^6 s. This effect was called *Light Induced Excited Spin State Trapping* (LIESST). In 1986, Hauser [45] demonstrated that this process is reversible by irradiation with λ = 820 nm wavelength light. An explanation for this phenomenon is illustrated in Figure 1.5. As one can see, the first LS → HS transition is induced by irradiating the compound, in the absorption band LS, $^1A_1$, with λ = 514 nm wavelength light, populating one of the excited levels $^1T_1$ or $^1T_2$. This new state has a very short lifetime causing the system to relax to an intermediate state, $^3T_2$ and $^3T_1$ followed by a transition to a metastable HS state, $^5T_2$. Since the energy barrier ΔE_{HL} is high, the lifetime of this state is greater than 10^6 s [81]. The phenomenon of reverse-LIESST [45] involves irradiating the absorption band of the HS state with a λ = 820 nm wavelength thus populating state ^5E. From this state the system can relax in one of the $^3T_1$ and $^3T_2$ states and, ultimately, in LS $^1A_1$.

The discovery of the LIESST phenomenon opened several new research directions for scientists. Thus, Herber and Casson in 1986 [82], using IR spectroscopy, found out that there

are temperature limits beyond which this phenomenon is no longer noticeable. In 1991 a study by Hauser *et al*. [83] on the lifetime of the photo-induced HS state showed that the lifetime values are closely related to the transition temperature $T_{1/2}$. More specifically, Hauser noted that the lifetime of the photo-induced HS state is higher for the compounds with lower transition temperatures. Over the years several studies on the LIESST effect [56,84-87] have been reported and new methods of excitation have been proposed: hard X-ray induced excited spin state trapping (HAXITH) [88,89]nuclear decay-induced excited spin state trapping (NIESST) [90-92], electron-induced excited spin state trapping [93].

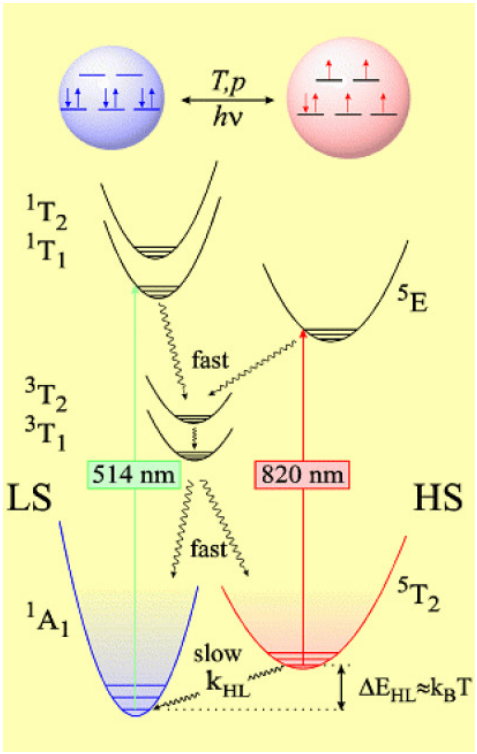

Figure 1.5 Jablonsky diagram for LIESST and reverse-LIESST effects [44]

1.4.2 Ligand-driven light-induced spin change (LD-LISC)

The first results reported on the effect of LD-LISC were performed on the $\left[Fe(stpy)_4(NCS)_2\right]$ compound (where stpy = 4-styrylpyrydine) by J. Zarembowitch's group [94]. This method involves irradiating the compound with a wavelength characteristic of the chemical reaction mechanism of the photochemical isomerization used in the cis-trans isomerization of the ligand. Thus, irradiating the compound with a chemical isomerization reaction characteristic wavelength allows for modifications in the behavior of the magnetic system. This phenomenon corresponds to the LD-LISC effect.

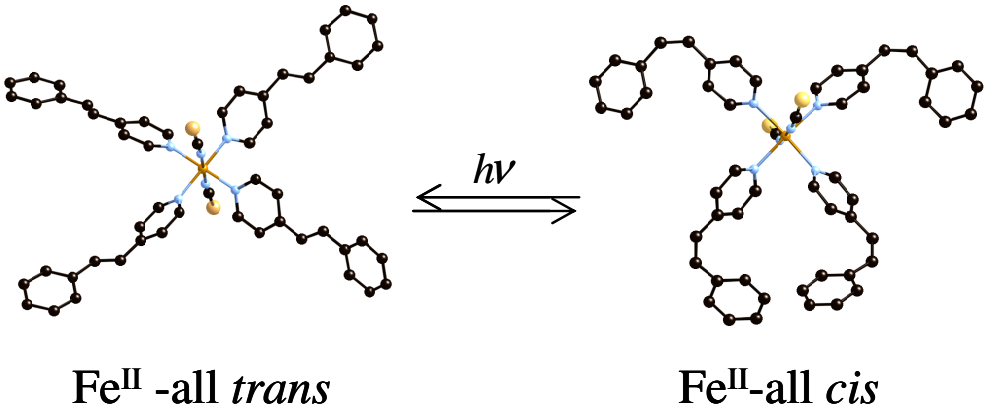

Figure 1.6 The crystallographic structure for compound $[Fe(trans\text{-}stpy)_4(NCSe)_2]$ and $[Fe(cis\text{-}stpy)_4(NCSe)_2]$ [95].

The LD-LISC effect leads to many potential applications such as information storage at ambient temperature.

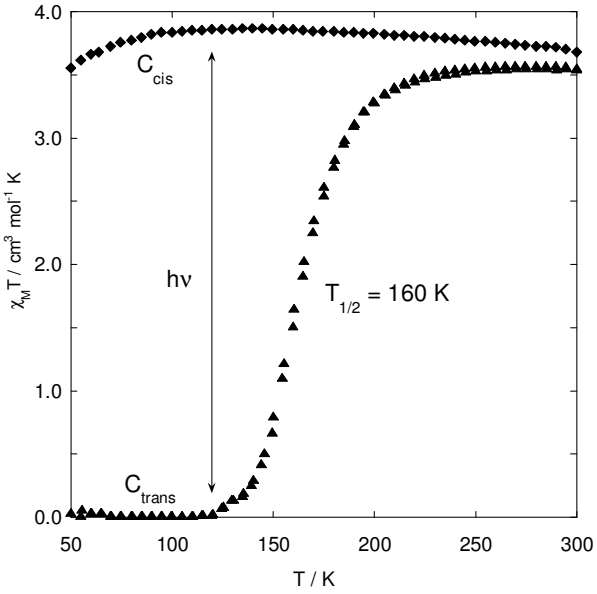

Figure 1.7 Temperature dependence of $\chi_M T$ for compound $Fe(stpy)_4(NCSe)_2$ ([96]).

1.5 Magnetic field induced spin transition

Spin transition may also be triggered by the application of a magnetic field, thus stabilizing the spin state characterized by a significant magnetic moment, i.e. the HS state. Historically, this effect was first reported in 1983 by Y. Qi *et al.* [97], who reported a 0.12K shift of the hysteresis loop towards lower temperatures in the case of the compound $\left[Fe(phen)_2(NCS)_2\right]$.

Studies on the effect of the magnetic field on the Co (II) and Fe (II) based compounds were also carried out by Bousseksou *et al.*, using a magnetic field of about 32T [98]. They have shown that by applying a magnetic field when the CTS is on the increasing branch of the

thermal hysteresis loop induces a quasi-complete and irreversible transition from the LS to the HS state.

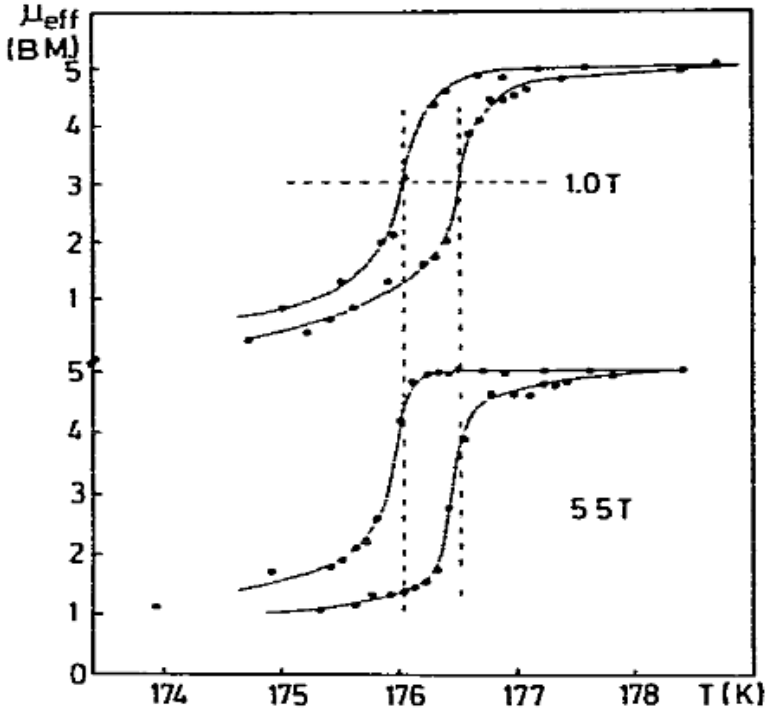

Figure 1.8 Temperature dependence of the effective magnetic moment of $[Fe(phen)_2(NCS)_2]$ [97]**.**

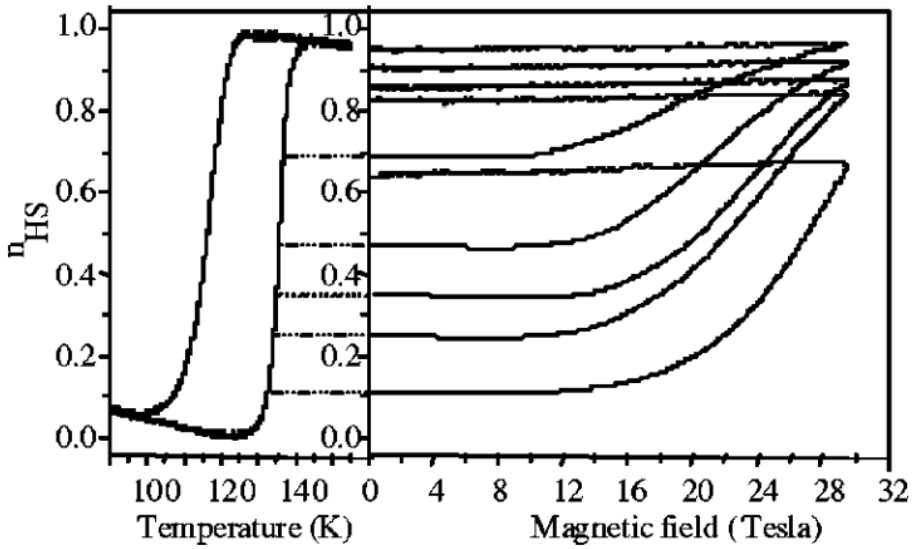

Figure 1.9 Different set of isotherms $n_{HS}(B)$ showing the irreversible triggering effect of $Co(H_2(fsa)_2en)(pz)_2$ in a pulsed magnetic field in the metastable LS state [99].

1.6 Electric field induced spin transition

The transition from one state to another can also induce changes in the electrical properties [2,37,100]. This was first shown by Rotaru *et al*. [2,37,101] in a study on the electrical conductivity of the $[Fe(Htrz)_2(trz)](BF_4)$ (Htrz = 1H-1,2,4-triazole, trz=1,2,4-triazole) spin crossover compound. They showed that the electrical conductivity decreases by two orders of magnitude when the transition from the LS state to the HS state occurs (Figure 1.10). This was shown to be a consequence of the fact that the thermal activation energy of the electrical conductivity is lower in the LS state than in the HS state.

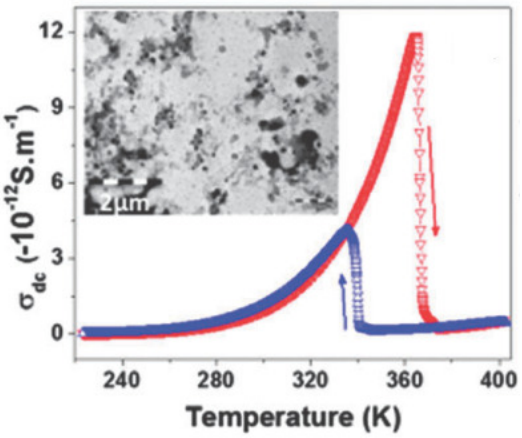

Figure 1.10 Temperature dependence of the electrical conductivity of $[Fe(Htrz)_2(trz)](BF_4)$ (Htrz=1H-1,2,4-triazole) [102]

Another important result reported on the charge transport behavior is that the Fe(II) centers participates at the charge transport mechanism [103]. Moreover, it was shown that by applying an electric field, the transition from the HS state to the LS state can be induced (Figure 1.11) [104].

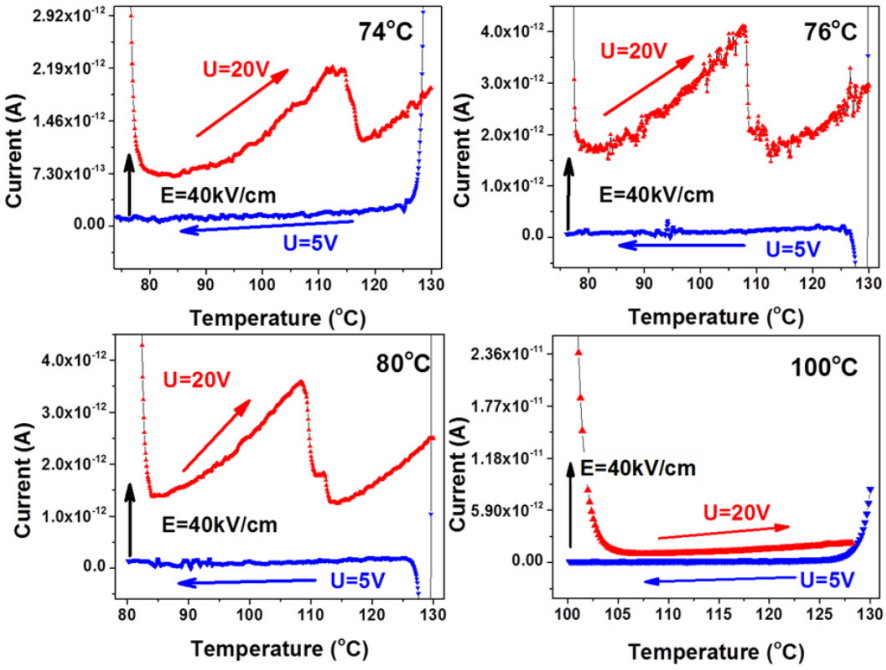

Figure 1.11 Temperature dependence of current under an applied electric field of step type for compound ([104]).

1.7 Theory. Models and methods

In parallel with the various and numerous investigations on CTS, the need for describing and understanding the phenomena and processes occurring under the action of various external stimuli has led to the development of theoretical models and simulation methods regarding CTS behavior [105]. Proposed in the early 70s [106,107], the Wajnflasz and Pick model is the first one to introduce the concept of molecular interaction. This model is able to qualitatively simulate the temperature induced spin transition. The model introduces a fictious spin with the eigen values σ = 1 (HS) and σ = -1 (LS). The interactions between the neighboring centers are described by an Ising type term, J. The total Hamiltonian is resolved by using mean field approximation and by taking into account the interactions with first order neighboring molecules only. Intermolecular interactions are not considered in this model.

In 1972, Bari and Sivardiere [108] continued the study by emphasizing some of the physical aspects that were ignored by the model of Wajnflasz *et al*., such as the temperature dependence of the intensity of the interactions. However, both models have a disadvantage concerning the entropy of the system associated with the two states (HS and LS) which does not show changes in the vicinity of the transition point which is a major issue [109].

The first model proposed to describe the influence of an applied external pressure on the spin transition behaviour is the Slichter and Drickamer model, developed in 1972 [72]. This model is the first to take into account the intermolecular interactions and, for years, has been the basis for other proposed models in order to point out the origin of interactions such as the atom-phonon coupling model or the mechano-elastic model. An important aspect is that this model entails a system of randomly distributed molecules, each molecule having its spin state independent of that of the neighboring molecule with which it interacts. Using this model and taking into account the intensity of interactions represented by the term Γ, both gradual transitions and step like transitions with and without hysteresis could be reproduced.

The model proposed by Sorai and Seki [110] in 1974 considered that the same spin state molecules are organized into independent domains. Their critical size can be calculated using calorimetric measurements. This model has the disadvantage that it cannot reproduce transitions with hysteresis.

1.7.1 Slichter and Drickamer model

When the molecules are in the solid state, intermolecular interactions play an important role in the characteristics of the spin transition. One of the most well-known thermodynamic approaches, taking into account the intermolecular interactions, is the thermodynamic model of Slichter and Drickamer [72], in which the enthalpy of the system, is described by the following equation:

$$G = n_{LS}G_{LS} + n_{HS}G_{HS} - TS_{mix} + \Gamma n_{HS}n_{LS} \tag{1.1}$$

where Γ is the intermolecular interaction parameter and S_{mix} is the mixt entropy which is defined as:

$$S_{mix} = -R\left[n_{LS}\ln\left(n_{LS}\right) + n_{HS}\ln\left(n_{HS}\right)\right] \tag{1.2}$$

Considering G_{LS} the reference of the energy, with $G_{LS} = 0$ and $\Delta G = G_{HS} = \Delta H - T\Delta S$ (where ΔH and ΔS represent the variations in enthalpy and entropy respectively during the spin transition), one obtains:

$$G = n_{HS}\Delta H + \Gamma n_{HS}\left(1-n_{HS}\right) - RT\left[\left(1-n_{HS}\right)\ln\left(1-n_{HS}\right) + n_{HS}\ln\left(n_{HS}\right) + n_{HS}\Delta S / R\right] \tag{1.3}$$

The equilibrium condition of the system, $\left(\frac{\partial G}{\partial n_{HS}}\right)_{T,P} = 0$, allows to obtain the temperature dependence as a function of the HS spin fraction:

$$T = \frac{\Delta H + \Gamma\left(1-2n_{HS}\right)}{R\ln\left(\frac{1-n_{HS}}{n_{HS}}\right)+\Delta S} \tag{1.4}$$

The equilibrium temperature of the system, defined for $n_{HS} = n_{LS} = 0.5$ (the number of molecules in the HS state is equal to the number of molecules in the LS state) is given by the expression:

$$T_{eq} = \frac{\Delta H}{\Delta S} \tag{1.5}$$

In the absence of intermolecular interactions, $\Gamma = 0$, the HS spin fraction can be expressed as:

$$n_{HS} = \frac{1}{1+\exp\left[\frac{\Delta H}{R}-\left(\frac{1}{T}-\frac{1}{T_{eq}}\right)\right]} \tag{1.6}$$

In this case the thermal population of spin states is in accordance with the Boltzmann law corresponding to a gradual transition.

In the case of $\Gamma \neq 0$, equation (1.3) allows for the computation of the HS fraction, n_{HS}, as a function of temperature. Depending on the value of the interaction parameter Γ, several transition types can be obtained:

- gradual, for values of $\Gamma < 2RT_{eq}$, characteristic of weak intermolecular interactions. The derivative $\frac{dT}{dn_{HS}}$ is positive for $0 < n_{HS} < 1$ and the transition is continuous and without hysteresis.
- abrupt, for values of $\Gamma \approx 2RT_{eq}$ characteristic of strong intermolecular interactions. The derivative $\frac{dT}{dn_{HS}}$ is positive except for $n_{HS} = 0.5$. The transition is discontinuous but without hysteresis.
- abrupt with hysteresis for values of $\Gamma > 2RT_{eq}$ characteristic of strong interactions. The curve $T = f\left(n_{HS}\right)$ has two extrema indicating the occurrence of thermal hysteresis (red curve in Figure 1.12).

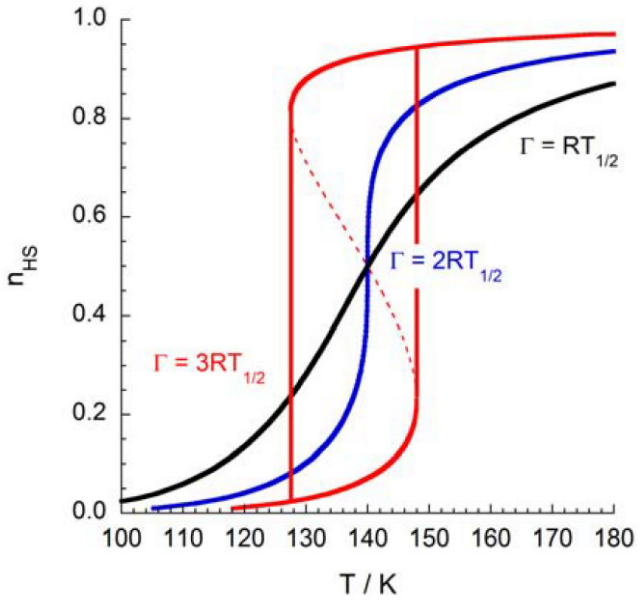

Figure 1.12 Thermal variation of HS fraction, n_{HS}, for different values of interaction parameter Γ (ΔH=7kJ.mol^{-1} and ΔS=50J.K^{-1}.mol^{-1}) [111].

1.7.2 Spiering model

In the model proposed by Spiering *et al.* [112] spin transition ions are considered as hard spheres inserted into an elastic, isotropic and homogeneous medium. The molecules are treated as point defects in a network causing differences in the volumes of the two LS and HS states. The interactions between the molecules in an elastic medium are due to the displacement field produced in the crystalline structure as a consequence of the molecular volume changes throughout the transition.

In this model, a sphere of volume v_α (α = HS, LS), placed in a crystal lattice of volume v_0 will have an elastic energy given by the expression:

$$e_\alpha = \frac{1}{2}K(\gamma_0 - 1)\frac{(v_\alpha - v_0)^2}{v_0} - \frac{1}{2}K\gamma_0(\gamma_0 - 1)\frac{(v_\alpha - v_0)^2}{V} \qquad (1.7)$$

where K is the compressibility module, γ_0 is Eshelby constant and V is the total volume of the crystal.

The energy due to differences in the two states of the crystal volume is represented by the first term while the surface effect is described by the second term.

1.7.3 Sorai & Seki model

In 1974, Sorai and Seki [110] proposed a different approach concerning the organization of the molecules in a SCO system. In their model the molecules are not randomly distributed but rather grouped in domains associated with their spin. For a system with N domains (each being composed of n molecules) and central transition temperatures T_c, the enthalpy of the system is given by the equation:

$$G = n_{HS}G_{HS} + (1 - n_{HS})G_{LS} + NkT\left[n_{HS}\ln(n_{HS}) + (1 - n_{HS})\ln(1 - n_{HS})\right] \qquad (1.8)$$

and the mixed entropy of the system is:

$$S_{mix} = -\frac{R}{n}\left[n_{HS}\ln\left(n_{HS}\right)+\left(1-n_{HS}\right)\ln\left(1-n_{HS}\right)\right] \tag{1.9}$$

For the case $\left(\frac{\partial G}{\partial n_{HS}}\right)_{T,P} = 0$, the HS spin fraction has the expression:

$$n_{HS} = \frac{1}{1+\exp\left[\frac{n\Delta H}{R}-\left(\frac{1}{T}-\frac{1}{T_c}\right)\right]} \tag{1.10}$$

Although it cannot reproduce the transition with hysteresis, this model can predict the fact that by decreasing the dimension of the domains, the transition will be more gradual (Figure 1.13). This model involves the assumption of an intermolecular interaction, which favors the HS state, even if in the expression for the free energy no term is introduced to represent such interactions.

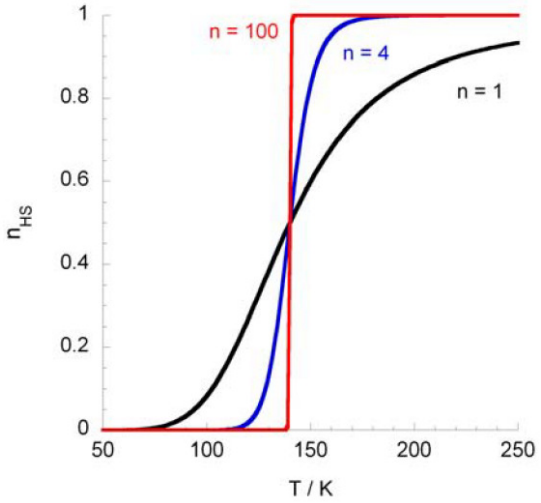

Figure 1.13 Thermal variation of HS fraction, n_{HS}, for different domain sizes (ΔH=7KJ.mol^{-1} and T_c=140K) [111].

1.7.4 Ising-like model

This model aims at providing a simple representation of the molecular states and intermolecular interactions. Starting with the model of Wajnflasz and Pick, the Ising–like model is adapted as a model with two different degenerate levels, each corresponding to a certain electronic configuration. If we consider that the molecules do not interact, the Ising type Hamiltonian of a system with two states, HS and LS, can be represented by the expression:

$$H = \frac{\Delta - k_B T \ln g}{2}\sum_{i=1}^{N}\sigma_i \tag{1.11}$$

where Δ is the energy difference between the two states, N is the number of molecules that compose the system, k_B is the Boltzmann's constant, T is the temperature of the system and σ_i is an operator associated to each molecule and that can take the value +1 when the molecule is in the HS state and the value -1 when the molecule is in the LS state. $g = g_{HS} / g_{LS}$ is the degeneracy ratio of the two states.

The spin fraction corresponding of the HS state is given by:

$$n_{HS} = \frac{1+\langle\sigma\rangle}{2} \tag{1.12}$$

The equilibrium temperature of the system for which $n_{HS} = n_{LS} = 1/2$ corresponding to a zero effective field is given by:

$$T_{1/2} = \frac{\Delta}{k_B \ln g} \tag{1.13}$$

Taking into account the expressions (1.10) and (1.13) we can say that the system is in the LS state for temperature values lower than the equilibrium temperature, $T < T_{1/2}$, and in the HS state for temperature values higher than the temperature of equilibrium, $T > T_{1/2}$.
For a system of *N* interacting molecules, where the intensity of the interactions is being represented by the parameter value *J*, the system Hamiltonian has the following expression:

$$H = \frac{\Delta - k_B T \ln g}{2} \sum_{i=1}^{N} \sigma_i - J \sum_{\langle i,j \rangle} \sigma_i \sigma_j \tag{1.14}$$

In order to solve this system one usually uses the mean field approximation technique. This technique involves the representation of the sum of interactions experienced by a single solid molecule by a single field also known as a molecular field.

Statistical thermodynamics allows for calculating the partition function of the system taking into account the filling of energy levels and the magnetization change as a funtion of temperature. One can then find equations identical to those obtained in the model Slichter & Drickamer, including the emergence of a hysteresis loop for constant interaction $J / k_B > T_{1/2}$.

Using this model, Bousseksou *et al*. [113] reproduced a two step transition considering two anti-ferromagnetically coupled molecular networks and, a few years later, the effect of intramolecular vibrations have been also taken into account [114]. In 1999 Linares *et al*. [115] reproduced, for the first time, the hysteretic transition of a 1D system considering the long-range interactions. Taking into account the long-range interactions, the Hamiltonian of the system can be written as:

$$H = \frac{\Delta - k_B T \ln g}{2} \sum_{i=1}^{N} \sigma_i - J \sum_{<i,j>} \sigma_i \sigma_j - G\langle\sigma\rangle \sum_{i=1}^{N} \sigma_i \tag{1.15}$$

For a 1D system, the Ising-like model type can be easily applied. However, for 2D and 3D systems, where the number of molecules is high, no exact solution has been found. Thus, many numerical techniques have been instead applied such as Monte Carlo including Metropolis [116,117]. Monte Carlo Arrhenius [58,65,118], Monte Carlo entropic sampling [58,119-121] or Molecular Dynamics [122,123]. Using these techniques, the Ising-like model was used to study the 1D systems [62,124] 2D [117,125] and the 3D systems as well [59,63].

1.7.5 Atom-phonon coupling model

Introduced in 2001 by Nasser [126] this model aims at providing an insight into the physical origin of intermolecular interactions in 1D systems. In this model molecules are modeled as atoms interconnected to each other through springs with a spring constant that depends on the electronic state of the molecules. The force between two neighboring interacting atoms *i* and *j* has an associated elastic constant k_{ij} given by:

- ✓ $C_{LL} = \lambda$, if the atoms are in the LS state;
- ✓ $C_{HH} = \nu$, if the atoms are in the HS state;
- ✓ $C_{HL} = \mu$, if an atom is in the LS state and other in HS state,

where $\lambda > \mu > \nu$.

For a system with N atoms, each atom being associated with a spin operator, which can take the value +1 or -1, depending of the electronic level in which it is found, the HS or the LS, the total Hamiltonian can be written as:

$$H = H_{spin} + H_{phonon} \tag{1.16}$$

where:

$$H_{spin} = \sum_{i=1}^{N} \frac{\Delta}{2} \sigma_i \tag{1.17}$$

$$H_{phonon} = E_c + E_p \tag{1.18}$$

E_c and E_p are the potential and kinetic energies and can be written as:

$$E_c = \sum_{i=1}^{N} \frac{p_i^2}{2m} \tag{1.19}$$

$$E_p = \sum_{i=1}^{N} \frac{1}{2} e_{i,i+1} \left(u_{i+1} - u_i\right)^2 \tag{1.20}$$

where p_i is the momentum of the i^{th} atom, m is the atomic mass, u_i represents the displacement of the atom from its equilibrium position and $e_{i,i+1}$ is the spring constant between the i molecule and molecule $i+1$ which can take one of the values λ, μ and ν, and can be expressed as:

$$e_{i,i+1} = \frac{\lambda + 2\mu + \nu}{4} + \frac{\nu - \lambda}{4}\left(\sigma_i + \sigma_{i+1}\right) + \frac{\lambda - 2\mu + \nu}{4} \sigma_i \sigma_{i+1} \tag{1.21}$$

In this case, if a periodic system is considered, the potential energy, E_p can be written as:

$$E_p = \sum_{i=1}^{N} \frac{\lambda + 2\mu + \nu}{8} \left(u_{i+1} - u_i\right)^2 + \sum_{i=1}^{N} \frac{\nu - \lambda}{8} \left[\left(u_i - u_{i-1}\right)^2 + \left(u_{i+1} - u_i\right)^2\right] \sigma_i + \sum_{i=1}^{N} \frac{\lambda - 2\mu + \nu}{8} \left(u_{i+1} - u_i\right)^2 \sigma_i \sigma_{i+1} \tag{1.22}$$

The Hamiltonian of the system becomes:

$$H = -\sum_{i=1}^{N} h_i \sigma_i - \sum_{i=1}^{N} J_{i,i+1} \sigma_i \sigma_{i+1} + \sum_{i=1}^{N} \left[\frac{p_i^2}{2m} + \frac{\lambda + 2\mu + \nu}{8} \left(u_{i+1} - u_i\right)^2\right] \tag{1.23}$$

where:

$$h_i = -\frac{\Delta}{2} - \frac{\nu - \lambda}{8} \left[\left(u_i - u_{i-1}\right)^2 + \left(u_{i+1} - u_i\right)^2\right] \tag{1.24}$$

is the effective field acting on a spin in a Zeeman type interaction and the second term may be associated with a type of exchange interaction energy between two neighboring spins:

$$J_{i,i+1} = \frac{\lambda - 2\mu + \nu}{8} \left(u_{i+1} - u_i\right)^2 \tag{1.25}$$

From equation (1.22) it is observed that the Hamiltonian of the system consists of a classical Ising Hamiltonian and the Hamiltonian of the phonon.

In 2004, a two steps transition was obtained from this model and in 2005 it was used to characterize the SCO in diluted systems of molecules [127].

1.7.6 Elastic models

Recently, a new class of cooperative SCO models has been developed to characterize the behavior of spin transition compounds namely the elastic model [128,129]. This model assumes that the molecules are connected together by a spring and as the transition from one state to another occurs, the molecule's volume varies producing a force acting on the spring interconnecting neighboring molecules. This force will cause neighboring molecules to change their position.

The elastic Hamiltonian is given by the expression:

$$H_{system} = \sum_i \frac{P_i^2}{2M} + \sum_i \frac{p_i^2}{2m} + \sum_i V_i^{intra}(r_i) + \sum_{\langle i,j \rangle} V_{ij}^{inter}(X_i, X_j, r_i, r_j) \tag{1.26}$$

where $V_i^{intra}(r_i)$ is the intramolecular energy and is expressed as a function of the i^{th} molecule's radius, p_i is the momentum and m is the reduced mass. The intermolecular interaction between two molecules i and j is given by the term: $V_{ij}^{inter}(X_i, X_j, r_i, r_j)$ where $X_i = (X_i, Y_i)$ are the coordinates of the center of the i^{th} molecule. $P_i = (P_X, P_Y)$ is the corresponding momentum and M is the mass of the molecule.

1.7.6.1 Mechano-elastic model

In this model the molecules are considered as being connected by elastic springs that are unstressed in the two spin states, HS and LS. When the state of a molecule transits from HS to LS, through a decrease in temperature, a force is generated that changes the position of its neighbors and then, progressively, the effect propagates to all the other molecules in the system [130]. Therefore, in the classical Hamiltonian (equation (1.14)) of a cooperative Ising-like system the short-range interaction term is replaced by the elastic interaction potential between molecules [131]:

$$V = \frac{k}{2} \sum_{i,j} \delta x_{ij}^2 \tag{1.27}$$

The transition probability for the HS-LS transition is given by the expression [129]:

$$P_{HS \to LS}^i = \frac{1}{\tau} \exp\left(-\frac{E_A - \kappa p_i}{k_B T} \right) \tag{1.28}$$

where E_A is the activation energy of the molecule for the HS-LS relaxation, and τ a constant for the time scale; the term κp_i expresses the energy difference under the pressure p_i between HS and LS states, where κ is a parameter representing the size difference among the molecules. The expression of the local pressure p_i can be written as:

$$p_i = \sum_{neighbour\ springs} k \delta x_{ij} \tag{1.29}$$

where the elongations δx_{ij} are taken positive for compressed springs and negative for elongated ones.

For the LS-HS transition the probability is written as:

$$P^{i}_{LS\to HS} = \frac{1}{\tau}\exp\left(-\frac{\Delta - k_B T \ln g}{k_B T}\right)\exp\left(-\frac{E_A + \kappa p_i}{k_B T}\right) \tag{1.30}$$

At mechanical equilibrium the following condition must hold:

$$\sum_{neighbour\ springs} k\delta\vec{x_i} = 0 \tag{1.31}$$

1.7.6.2 Electro-elastic model

In the framework of this model the spin transition is accompanied by changes in volume as well as deformations of the crystal lattice related to the properties of elastic interactions between molecules [132,133]. Thus, the electro-elastic model is constructed to include two contributions:

(a) an electronic contribution taking into account the energy of the ligand field and the degeneration of the system (first term equation (1.32));

(b) a structural contribution, related to the elastic interaction between molecules (the last two terms of equation (1.32)).

$$H = \sum_i \frac{1}{2}\left(\Delta - k_B T \ln g\right)\sigma_i + \sum_{\langle i,j\rangle} A\left[r_{ij} - R_0\left(\sigma_i, \sigma_j\right)\right]^2 + \sum_{\langle i,k\rangle} B\left[r_{ik} - R'_0\left(\sigma_i, \sigma_k\right)\right]^2 \tag{1.32}$$

where A and B represent the elastic constants between the first peer nearest neighbors and second nearest neighbors relative to the (i, j) site. The distance between two first nearest molecules is denote by R_0^{HH}, R_0^{HL} and R_0^{LL} in regards to the molecules state, HS-HS, HS-LS, LS-LS. In addition, considering that $R_0^{HL} = \left(R_0^{HH} + R_0^{LL}\right)/2$ the general expression of the equilibrium distance can be written as:

$$R_0\left(\sigma_i, \sigma_j\right) = R_0^{HL} + \frac{\delta R}{4}\left(\sigma_i + \sigma_j\right) \tag{1.33}$$

where:

$$\delta R = \left(R_0^{HH} - R_0^{LL}\right) \tag{1.34}$$

1.8 Monte Carlo methods

Simulation of physical processes is a challenge for scientists trying to understand the physical phenomena that occur inside the materials. Thus, besides some analytical methods which can solve exactly finite or infinite systems, several other methods, mainly numerical have been develloped. Monte Carlo methods are the most used methods by researchers in order to model probabilistic or stochastic systems whose analytical solutions are too complicated or impossible to be determined. Concerning SCO materials, the Monte Carlo methods are used in combination with certain models such as: Ising-like model, atom-phonon coupling (APC) model or mechano-elastic model. All these models are used by researchers to simulate the behavior of SCO materials when they are disturbed by an external perturbation such as: thermal or/and pressure variation, light irradiation, applied magnetic or electrical fields.

Recent investigations using Monte Carlo methods applied to an Ising-like model [107,113,134] have shown that the behavior of SCO materials is influenced by the lattice architecture of the system, the system's size (or size of particles) [65,135]. Also, the role of

edge effect in 1D, 2D and 3D SCO systems have been analyzed, considering that the edge molecules are trapped in the HS states [62,63]. Considering the edge molecule as active molecules some important results have been reported in the recent years for 1D and 2D SCO network systems [64,136,137].

1.8.1 Monte Carlo Metropolis

This method introduced by Metropolis [138] was initially proposed for the specific case of a canonical ensemble but it has been adopted in other fields. The Metropolis algorithm consists in the following description: a system with a configuration C_i of spin operators and with energy E_i is shifted in the configuration C_{i+1} with energy E_{i+1} by changing a spin operator, k, from its initial value σ_k to $-\sigma_k$ only if the following conditions are met: (i) the energy of the new configuration is lower than the previous one or (ii) in the oposite case, then a random number, R is generated, in the interval [0,1]; if the probability to move from the configuration C_i to configuration C_{i+1}, $P = e^{-(E_{i+1}-E_i)/k_B T}$, is less that the value of R, the new configuration is accepted. Otherwise, the new configuration is refused and restarting from the same configuration C_i, the same steps are applied. This new configuration will be accepted or not depending on the fulfillment of the conditions specified above.
This method has been used over the years in combination with main models that are used to describe the spin transition behavior [116,139,140].

1.8.2 Monte Carlo entropic sampling

The Monte Carlo Entropic Sampling (MCES) can be used when the Hamiltonian of the system cannot be solved exactly via the transfer matrix method or when the mean-field approximation method is not appropriate enough for researchers' investigations. The MCES in combination with the Ising-like model is used to obtain the table that contains the macroscopic variables, m and s, and their density, $d(m,s)$, m and s are defined as:

$$m = \sum_{i=1}^{N} \sigma_i \quad and \quad s = \sum_{\langle i,j \rangle} \sigma_i \sigma_j \tag{1.35}$$

The principle of MCES, described by the Shteto *et al*. [119,120] is the follow: in order to obtain a desired distribution P, it is necessary to introduce an appropriate distribution as a bias in the detailed balance equation expressed as:

$$P_i W(i \to j) = P_j W(j \to i) \tag{1.36}$$

The biasing probability was chosen as the inverse of the desired restricted density of states.

$$P_i \propto \frac{1}{d(m_i, s_i)} \tag{1.37}$$

In this way, configurations with weakly degenerate macrostates are favored and those with highly degenerate states are damped. In this case, the balance equation (1.36) can be written as:

$$\frac{W(i \to j)}{W(\mathrm{j} \to i)} = \frac{P_j}{P_i} = \frac{d(m_i, s_i)}{d(m_j, s_j)} \tag{1.38}$$

Because in the first Monte Carlo step the density of the state $d(m,s)$ is unknown we put all $d(m,s)$ equal to 1. So, after iteration k the density will be $d_k(m,s)$. Then, using $d_k(m,s)$ as a bias, a MC sampling is run; it is termed a 'Monte Carlo stage' and yields a histogram of the frequency of the macrostates: $H_k(m,s)$:

$$H_k(m,s) \propto d(m,s)\frac{1}{d_k(m,s)} \tag{1.39}$$

The resulting restricted density of states is obtained after applying a correction for the bias:

$$d_{k+1}(m,s) \propto d_k(m,s)\ H_k(m,s) \tag{1.40}$$

From the table of the *d(m,s)* thus built from the (*m*, *s*) states, the partition function can be calculated using the following expression:

$$Z = \sum_{(m,s)} d(m,s)\exp(-\beta(-hm - Js)) \tag{1.41}$$

from which all the thermodynamic properties of the system can be analytically derived.
So, in the evolution of the HS fraction given by equation (1.12) the average magnetization can be written as:

$$<\sigma>=\frac{\sum_{i=1,NL}\frac{m_i}{N}d(m_i s_i)\exp\left(-\frac{1}{k_B T}(-h_f m_i - Js_i)\right)}{\sum_{i=1,NL} d(m_i s_i)\exp\left(-\frac{1}{k_B T}(-h_f m_i - Js_i)\right)} \tag{1.42}$$

where *NL* is the number of distinct configuration of states <*m,s*> and *d(m,s)* is the number of configuration for a given set of values.

1.9 Conclusions

Through of this chapter we wanted to explain the spin transition phenomenon and are presented the main models used to model the behaviors of these compounds. Although ST phenomenon is purely electronic nature, the behavior of an ensemble of molecules in the solid phase depends largely on the nature of intermolecular interactions. The recently studies show that the spin interactions are of two types: short-range interactions and long-range interactions. The short-range interactions are of electronic nature and/or elastic between two neighboring molecules. These interactions depend of the distance between molecules, and their network orientation. The long-range interactions are due to internal pressure created by changing the volume of molecules in crystal. Despite numerous theoretical studies on this topic, the spin interaction issue in spin transition is not understood completely. Until now, various models have been proposed, but the most used are those proposed by Wajnflasz, Slichter and Drickamer sister Seki. The cooperativity origin is, in turn, usually attributed to elastic interactions. Various stimuli can be used to induce the spin transition. The most used stimuli to induce the transition are the variation of temperature and application of external pressure. In the next chapter are presented some behaviors of SCO compounds under action of temperature or pressure variation and their applications as sensors.

1.10 References

[1] Xu, Xiao, X. Yang, L. Zang, Tao, Journal of the American Chemical Society 127 (2005) 2386.

[2] A. Rotaru, J. Dugay, R.P. Tan, I.A. Gural'skiy, L. Salmon, P. Demont, J. Carrey, G. Molnar, M. Respaud, A. Bousseksou, Advanced Materials 25 (2013) 1745.

[3] S.V. Aradhya, L. Venkataraman, Nat Nano 8 (2013) 399.

[4] B. Capozzi, J. Xia, O. Adak, E.J. Dell, Z.-F. Liu, J.C. Taylor, J.B. Neaton, L.M. Campos, L. Venkataraman, Nat Nano 10 (2015) 522.

[5] J. Linares, E. Codjovi, Y. Garcia, Sensors 12 (2012) 4479.

[6] C.-M. Jureschi, I. Rusu, E. Codjovi, J. Linares, Y. Garcia, A. Rotaru, Physica B: Condensed Matter 449 (2014) 47.

[7] C.M. Jureschi, J. Linares, A. Rotaru, M.H. Ritti, M. Parlier, M.M. Dîrtu, M. Wolff, Y. Garcia, Sensors (Basel, Switzerland) 15 (2015) 2388.

[8] G. Molnar, L. Salmon, W. Nicolazzi, F. Terki, A. Bousseksou, Journal of Materials Chemistry C 2 (2014) 1360.

[9] O. Kahn, E. Codjovi, Y. Garcia, P.J. vanKoningsbruggen, R. Lapouyade, L. Sommier, in: M.M. Turnbull, T. Sugimoto, L.K. Thompson (Eds.), Molecule-Based Magnetic Materials - Theory, Techniques, and Applications, 1996, p. 298.

[10] L. Cambi, L. Szegö, Berichte der deutschen chemischen Gesellschaft (A and B Series) 64 (1931) 2591.

[11] E. Konig, Chemical Communications 3 (1966) 61.

[12] E. König, K. Madeja, JACS 88 (1966) 4528.

[13] E. Konig, Structure and Bonding 76 (1991) 51.

[14] R.C. Stoufer, D.H. Busch, W.B. Hadley, Journal of the American Chemical Society 83 (1961) 3732.

[15] J. Zarembowitch, O. Kahn, Inorganic Chemistry 23 (1984) 589.

[16] J. Faus, M. Julve, F. Lloret, J.A. Real, J. Sletten, Inorganic Chemistry 33 (1994) 5535.

[17] K. Heinze, G. Huttner, L. Zsolnai, P. Schober, Inorganic Chemistry 36 (1997) 5457.

[18] W. Eberspach, N. Elmurr, W. Klaui, Angewandte Chemie-International Edition in English 21 (1982) 915.

[19] W. Klaui, W. Eberspach, P. Gutlich, Inorganic Chemistry 26 (1987) 3977.

[20] A. Hauser, Spin Crossover in Transition Metal Compounds I, 2004, p. 49.

[21] R. Boca, L. Dlhan, W. Linert, H. Ehrenberg, H. Fuess, W. Haase, Chemical Physics Letters 307 (1999) 359.

[22] K. Nakatani, J. Sletten, S. Halutdesporte, S. Jeannin, Y. Jeannin, O. Kahn, Inorganic Chemistry 30 (1991) 164.

[23] P.G. Sim, E. Sinn, Journal of the American Chemical Society 103 (1981) 241.

[24] L. Kaustov, M.E. Tal, A.I. Shames, Z. Gross, Inorg Chem 36 (1997) 3503.

[25] H.J. Krokoszinski, C. Santandrea, E. Gmelin, K. Barner, Physica Status Solidi B-Basic Research 113 (1982) 185.

[26] Y. Garcia, O. Kahn, J.P. Ader, A. Buzdin, Y. Meurdesoif, M. Guillot, Physics Letters A 271 (2000) 145.

[27] D.M. Halepoto, D.G.L. Holt, L.F. Larkworthy, G.J. Leigh, D.C. Povey, G.W. Smith, Journal of the Chemical Society-Chemical Communications (1989) 1322.

[28] D.M. Halepoto, D.G.L. Holt, L.F. Larkworthy, D.C. Povey, G.W. Smith, G.J. Leigh, Polyhedron 8 (1989) 1821.

[29] M. Sorai, Y. Yumoto, D.M. Halepoto, L.F. Larkworthy, Journal of Physics and Chemistry of Solids 54 (1993) 421.

[30] C.-M. Jureschi, J. Linares, A. Boulmaali, P. Dahoo, A. Rotaru, Y. Garcia, Sensors 16 (2016) 187.

[31] A. Rotaru, J. Dugay, R. Tan, I. Guralskiy, L. Salmon, P. Demont, J. Carrey, G. Molnar, M. Respaud, A. Bousseksou, Adv Mater 25 (2013) 1745
[32] C. Lefter, V. Davesne, L. Salmon, G. Molnár, P. Demont, A. Rotaru, A. Bousseksou, Magnetochemistry 2 (2016) 18.
[33] C.J. Humphreys, Nature 401 (1999) 21.
[34] P. Gütlich, A.B. Gaspar, Y. Garcia, Beilstein Journal of Organic Chemistry 9 (2013) 342.
[35] T. Mahfoud, G. Molnar, S. Cobo, L. Salmon, C. Thibault, C. Vieu, P. Demont, A. Bousseksou, *Applied Physics Letters* **99** (2011) 053307.
[36] T. Mahfoud, G. Molnar, S. Bonhommeau, S. Cobo, L. Salmon, P. Demont, H. Tokoro, S.I. Ohkoshi, K. Boukheddaden, A. Bousseksou, *Journal of the American Chemical Society* **131** (2009) 15049.
[37] C. Lefter, I.y.A. Gural'skiy, H. Peng, G. Molnár, L. Salmon, A. Rotaru, A. Bousseksou, P. Demont, physica status solidi (RRL) – Rapid Research Letters 8 (2014) 191.
[38] V. Legrand, S. Pillet, C. Carbonera, M. Souhassou, J.F. Letard, P. Guionneau, C. Lecomte, European Journal of Inorganic Chemistry (2007) 5693.
[39] S. Pillet, J. Hubsch, C. Lecomte, European Physical Journal B 38 (2004) 541.
[40] N.N. Greenwood, T.C. Gibb, (1971).
[41] P. Guionneau, F. Le Gac, S. Lakhoufi, A. Kaiba, D. Chasseau, J.F. Letard, P. Negrier, D. Mondieig, J.A.K. Howard, J.M. Leger, Journal of Physics-Condensed Matter 19 (2007).
[42] W. Irler, G. Ritter, E. König, H.A. Goodwin, S.M. Nelson, Solid State Communications 29 (1979) 39.
[43] T. Granier, B. Gallois, J. Gaultier, J.A. Real, J. Zarembowitch, Inorganic Chemistry 32 (1993) 5305.
[44] S. Decurtins, P. Gutlich, K.M. Hasselbach, A. Hauser, H. Spiering, Inorganic Chemistry 24 (1985) 2174.
[45] A. Hauser, Chemical Physics Letters 124 (1986) 543.
[46] W. Linert, M.C. Grunert, A.B. Koudriavtsev, Spin Crossover in Transition Metal Compounds Iii, 2004, p. 105.
[47] J.P. Martin, J. Zarembowitch, A. Bousseksou, A. Dworkin, J.G. Haasnoot, F. Varret, Inorganic Chemistry 33 (1994) 6325.
[48] N. Moliner, L. Salmon, L. Capes, M.C. Munoz, J.F. Letard, A. Bousseksou, J.P. Tuchagues, J.J. McGarvey, A.C. Dennis, M. Castro, R. Burriel, J.A. Real, Journal of Physical Chemistry B 106 (2002) 4276.
[49] J.A. Rodriguez-Velamazan, M. Castro, E. Palacios, R. Burriel, J.S. Costa, J.F. Letard, Chemical Physics Letters 435 (2007) 358.
[50] W. Morscheidt, J. Jeftic, E. Codjovi, J. Linares, A. Bousseksou, H. Constant-Machado, F. Varret, Measurement Science & Technology 9 (1998) 1311.
[51] E. Codjovi, W. Morscheidt, J. Jeftic, J. Linares, M. Nogues, A. Goujon, O. Roubeau, H. Constant-Machado, A. Desaix, A. Bousseksou, M. Verdaguer, F. Varret, Molecular Crystals and Liquid Crystals Science and Technology Section a-Molecular Crystals and Liquid Crystals 334 (1999) 1295.
[52] A. Rotaru, J. Linares, F. Varret, E. Codjovi, A. Slimani, R. Tanasa, C. Enachescu, A. Stancu, J. Haasnoot, Physical Review B 83 (2011) 224107.
[53] E.D. Loutete-Dangui, E. Codjovi, H. Tokoro, P.R. Dahoo, S. Ohkoshi, K. Boukheddaden, Physical Review B 78 (2008).
[54] K. Boukheddaden, E.D. Loutete-Dangui, E. Codjovi, M. Castro, J.A. Rodriguez-Velamazan, S. Ohkoshi, H. Tokoro, M. Koubaa, Y. Abid, F. Varret, *Journal of Applied Physics* **109** (2011) 013520.

[55] A. Goujon, F. Varret, K. Boukheddaden, C. Chong, J. Jeftic, Y. Garcia, A.D. Naik, J.C. Ameline, E. Collet, Inorganica Chimica Acta 361 (2008) 4055.
[56] L. Zhang, G.-C. Xu, H.-B. Xu, T. Zhang, Z.-M. Wang, M. Yuan, S. Gao, Chemical Communications 46 (2010) 2554.
[57] J.A. Real, H. Bolvin, A. Bousseksou, A. Dworkin, O. Kahn, F. Varret, J. Zarembowitch, Journal of the American Chemical Society 114 (1992) 4650.
[58] D. Chiruta, J. Linares, P.R. Dahoo, M. Dimian, Journal of Applied Physics 112 (2012).
[59] D. Chiruta, J. Linares, Y. Garcia, P.R. Dahoo, M. Dimian, European Journal of Inorganic Chemistry 2013 (2013) 3601.
[60] D. Boinnard, A. Bousseksou, A. Dworkin, J.M. Savariault, F. Varret, J.P. Tuchagues, Inorganic Chemistry 33 (1994) 271.
[61] Y. Garcia, O. Kahn, L. Rabardel, B. Chansou, L. Salmon, J.P. Tuchagues, Inorganic Chemistry 38 (1999) 4663.
[62] D. Chiruta, J. Linares, Y. Garcia, M. Dimian, P.R. Dahoo, Physica B: Condensed Matter 434 (2014) 134.
[63] D. Chiruta, J. Linares, M. Dimian, Y. Alayli, Y. Garcia, European Journal of Inorganic Chemistry 2013 (2013) 5086.
[64] D. Chiruta, C.-M. Jureschi, J. Linares, P.R. Dahoo, Y. Garcia, A. Rotaru, The European Physical Journal B 88 (2015) 1.
[65] A. Atitoaie, R. Tanasa, C. Enachescu, Journal of Magnetism and Magnetic Materials 324 (2012) 1596.
[66] S.M. Neville, B.A. Leita, G.J. Halder, C.J. Kepert, B. Moubaraki, J.F. Letard, K.S. Murray, Chemistry-a European Journal 14 (2008) 10123.
[67] J.K. Tang, J.S. Costa, S. Smulders, G. Molnar, A. Bousseksou, S.J. Teat, Y.G. Li, G.A. van Albada, P. Gamez, J. Reedijk, Inorganic Chemistry 48 (2009) 2128.
[68] P. Gütlich, Y. Garcia, H. Spiering, **Magnetism: Molecules to Materials IV**, Wiley-VCH Verlag GmbH & Co. KGaA, 2002.
[69] A. Stancu, C. Enachescu, R. Tanasa, J. Linares, E. Codjovi, F. Varret, Frontiers in condensed matter physics research, Nova Science Publishers (2006).
[70] A.H. Ewald, E. Sinn, Inorganic Chemistry 8 (1969) 537.
[71] B. C.B., A. M., H.G. Drickamer, Inorg Chem 10 (1971) 1338.
[72] C.P. Slichter, H.G. Drickamer, J. Chem. Phys. 56 (1972) 2142.
[73] E. Codjovi, N. Menendez, J. Jeftic, F. Varret, Comptes Rendus De L Academie Des Sciences Serie Ii Fascicule C-Chimie 4 (2001) 181.
[74] A. Bousseksou, G. Molnar, J.P. Tuchagues, N. Menendez, E. Codjovi, F. Varret, Comptes Rendus Chimie 6 (2003) 329.
[75] V. Ksenofontov, G. Levchenko, H. Spiering, P. Gutlich, J.F. Letard, Y. Bouhedja, O. Kahn, Chemical Physics Letters 294 (1998) 545.
[76] J. Jeftic, High Pressure Research 29 (2009) 369.
[77] V. Ksenofontov, A.B. Gaspar, P. Gutlich, Spin Crossover in Transition Metal Compounds Iii, 2004, p. 23.
[78] P. Gutlich, V. Ksenofontov, A.B. Gaspar, Coordination Chemistry Reviews 249 (2005) 1811.
[79] A.B. Gaspar, V. Ksenofontov, V. Martinez, M.C. Munoz, J.A. Real, P. Gütlich, European Journal of Inorganic Chemistry (2004) 4770.
[80] J.J. McGarvey, I. Lawthers, Journal of the Chemical Society, Chemical Communications 16 (1982) 906.
[81] S. Decurtins, P. Gutlich, C.P. Kohler, H. Spiering, A. Hauser, *Chemical Physics Letters* **105** (1984) 1.
[82] R. Herber, L.M. Casson, Inorganic Chemistry 25 (1986) 847.
[83] A. Hauser, A. Vef, P. Adler, Journal of Chemical Physics 95 (1991) 8710.

[84] B. Ordejon, C. de Graaf, C. Sousa, Journal of the American Chemical Society 130 (2008) 13961.
[85] N. Suaud, M.L. Bonnet, C. Boilleau, P. Labeguerie, N. Guihery, Journal of the American Chemical Society 131 (2009) 715.
[86] C. Chong, M. Itoi, K. Boukheddaden, E. Codjovi, A. Rotaru, F. Varret, F.A. Frye, D.R. Talham, I. Maurin, D. Chernyshov, M. Castro, Physical Review B 84 (2011) 144102.
[87] A. Rotaru, J. Linares, Journal of Optoelectronics and Advanced Materials 9 (2007) 2724.
[88] G. Vanko, F. Renz, G. Molnar, T. Neisius, S. Karpati, Angewandte Chemie-International Edition 46 (2007) 5306.
[89] F. Renz, G. Vanko, P. Homenya, R. Saadat, Z. Nemeth, S. Huotari, European Journal of Inorganic Chemistry (2012) 2653.
[90] P. Gütlich, J. Ensling, F. Tuczek, Hyperfine Interactions 84 (1994) 447.
[91] P. Gutlich, Molecular Crystals and Liquid Crystals Science and Technology Section a-Molecular Crystals and Liquid Crystals 305 (1997) 17.
[92] P. Gütlich, Spin Crossover in Transition Metal Compounds Ii, 2004, p. 231.
[93] T.G. Gopakumar, F. Matino, H. Naggert, A. Bannwarth, F. Tuczek, R. Berndt, Angewandte Chemie-International Edition 51 (2012) 6262.
[94] J. Zarembowitch, New Journal of Chemistry 16 (1992) 255.
[95] M.L. Boillot, J. Zarembowitch, A. Sour, Spin Crossover in Transition Metal Compounds Ii, 2004, p. 261.
[96] V. Ksenofontov, G. Levchenko, H. Spiering, P. Gutlich, J.-F. Letard, Y. Bouhedja, O. Kahn, Chem Phys Lett 294 (1998) 545
[97] Y. Qi, E.W. Müller, H. Spiering, P. Gütlich, Chemical Physics Letters 101 (1983) 503.
[98] A. Bousseksou, N. Negre, M. Goiran, L. Salmon, J.P. Tuchagues, M.L. Boillot, K. Boukheddaden, F. Varret, European Physical Journal B 13 (2000) 451.
[99] A. Bousseksou, K. Boukheddaden, M. Goiran, C. Consejo, M.L. Boillot, J.P. Tuchagues, *Physical Review B* **65** (2002) 172412.
[100] C. Lefter, R. Tan, J. Dugay, S. Tricard, G. Molnar, L. Salmon, J. Carrey, A. Rotaru, A. Bousseksou, Physical Chemistry Chemical Physics 17 (2015) 5151.
[101] A. Rotaru, I.y.A. Gural'skiy, G. Molnar, L. Salmon, P. Demont, A. Bousseksou, Chemical Communications 48 (2013) 4163.
[102] A. Rotaru, I.y.A. Gural'skiy, G. Molnar, L. Salmon, P. Demont, A. Bousseksou, Chemical Communications 48 (2012) 4163.
[103] C. Lefter, S. Tricard, H. Peng, G. Molnar, L. Salmon, P. Demont, A. Rotaru, A. Bousseksou, Journal of Physical Chemistry C 119 (2015) 8522.
[104] C. Lefter, FIESC, Vol. Ph. D, Stefan cel Mare University, Suceava (2015).
[105] J. Pavlik, R. Boca, European Journal of Inorganic Chemistry (2013) 697.
[106] J. Wajnflasz, J. Phys. Stat. Solidi 40 (1970) 537.
[107] J. Wajnflasz, R. Pick, J. Phys. Colloques 32 (1971) C1.
[108] R.A. Bari, J. Sivardiere, Phys. Rev. B 5 (1972) 4466.
[109] M. Sorai, S. Seki, Journal of the Physical Society of Japan 33 (1972) 575.
[110] M. Sorai, S. Seki, J. Phys. Chem. Solids 35 (1974) 555.
[111] A. Tissot, ICMM, Vol. Ph. D, Universite de Paris-Sud 11, Orsay (2011).
[112] H. Spiering, E. Meissner, H. Koppen, E.W. Muller, P. Gutlich, Chemical Physics 68 (1982) 65.
[113] A. Bousseksou, J. Nasser, J. Linares, K. Boukheddaden, F. Varret, Journal De Physique I 2 (1992) 1381.
[114] A. Bousseksou, H. Constantmachado, F. Varret, Journal De Physique I 5 (1995) 747.
[115] J. Linares, H. Spiering, F. Varret, European Physical Journal B 10 (1999) 271.

[116] J. Linares, J. Nasser, K. Boukheddaden, A. Bousseksou, F. Varret, Journal of Magnetism and Magnetic Materials 140 (1995) 1507.
[117] D. Chiruta, C.-M. Jureschi, J. Linares, Y. Garcia, A. Rotaru, Journal of Applied Physics 115 (2014).
[118] M. Nishino, K. Boukheddaden, S. Miyashita, F. Varret, Physical Review B 68 (2003).
[119] I. Shteto, J. Linares, F. Varret, Physical Review E 56 (1997) 5128.
[120] J. Linares, C. Enachescu, K. Boukheddaden, F. Varret, Polyhedron 22 (2003) 2453.
[121] R. Tanasa, J. Linares, C. Enachescu, F. Varret, A. Stancu, Physica B-Condensed Matter 372 (2006) 215.
[122] A. Slimani, F. Varret, K. Boukheddaden, D. Garrot, H. Oubouchou, S. Kaizaki, Physical Review Letters 110 (2013).
[123] A. Slimani, K. Boukheddaden, F. Varret, H. Oubouchou, M. Nishino, S. Miyashita, Physical Review B 87 (2013).
[124] D. Chiruta, J. Linares, M. Dimian, Y. Garcia, European Journal of Inorganic Chemistry 2013 (2013) 951.
[125] D. Chiruta, J. Linares, P. Richard Dahoo, M. Dimian, Physica B: Condensed Matter 435 (2014) 76.
[126] J.A. Nasser, European Physical Journal B 21 (2001) 3.
[127] J.A. Nasser, European Physical Journal B 48 (2005) 19.
[128] M. Nishino, K. Boukheddaden, Y. Konishi, S. Miyashita, Physical Review Letters 98 (2007).
[129] C. Enachescu, L. Stoleriu, A. Stancu, A. Hauser, Physical Review Letters 102 (2009).
[130] C. Enachescu, M. Nishino, S. Miyashita, A. Hauser, A. Stancu, L. Stoleriu, Epl 91 (2010).
[131] S. Miyashita, Y. Konishi, M. Nishino, H. Tokoro, P.A. Rikvold, Physical Review B 77 (2008).
[132] K. Boukheddaden, R. Traiche, H. Oubouchou, J. Linares, Magnetochemistry 2 (2016) 17.
[133] A. Slimani, K. Boukheddaden, F. Varret, M. Nishino, S. Miyashita, The Journal of Chemical Physics 139 (2013).
[134] K. Boukheddaden, J. Linares, E. Codjovi, F. Varret, V. Niel, J.A. Real, *Journal of Applied Physics* **93** (2003) 7103.
[135] A. Muraoka, K. Boukheddaden, J. Linares, F. Varret, Physical Review B 84 (2011).
[136] C.-M. Jureschi, B.-L. Pottier, J. Linares, P. Richard Dahoo, Y. Alayli, A. Rotaru, Physica B: Condensed Matter 486 (2016) 160.
[137] J. Linares, C.-M. Jureschi, A. Boulmaali, K. Boukheddaden, Physica B: Condensed Matter 486 (2016) 164.
[138] N. Metropolis, A.W. Rosenbluth, M.N. Rosenbluth, A.H. Teller, E. Teller, The Journal of Chemical Physics 21 (1953) 1087.
[139] A.M. Apetrei, C. Enachescu, R. Tanasa, L. Stoleriu, A. Stancu, Physica B: Condensed Matter 405 (2010) 3673.
[140] C. Enachescu, M. Nishino, S. Miyashita, L. Stoleriu, A. Stancu, Physical Review B 86 (2012) 054114.

Chapter 2

Sensing applications of SCO materials

Contents

2 Sensing applications of SCO materials

2.1 Introduction

Variation of temperature and/or pressure is most often used to induce the spin transition phenomenon. In this chapter the behaviors of a few compounds and their colors in both LS and HS spin states, respectively are presented. The potential applications as sensors of these materials are also presented in this chapter.

The temperature and pressure effects have been extensively studied in terms of both experimental and theoretical standpoint. In order to experimentally investigate simultaneous the temperature and pressure effect of SCO compounds, a pressure cell, connected to a high pressure system, was been used. The cell body is constructed using a bronze-beryllium alloy, and, as a pressure transmitting medium, either transparent and inert gases, such as He, Ne, Ar and N_2, or a liquid (4:1 Methanol/Ethanol, Silicone Oil, Fluorinert, Daphne 7474 Cyclohexane) are being used. However, the use of fluids has the disadvantage of the loss of hydrostatic properties [1] at low temperatures or high pressures [2-7]. The first study on the effect of pressure was performed by Ewald *et al*. [8] on a SCO compound that has Co(II) ion as its central ion. Due to the color change of these materials in response to a temperature and/or pressure change, SCO materials are considered to be good candidates for practical implementation as temperature or pressure sensors.

2.2 Temperature sensors

Over the years have been reports of SCO materials exhibiting a strong color contrast between the two transitional states (Figure 2.1). Thus, as a result of temperature and/or pressure variations, different behaviors of spin transition compounds have been reported.

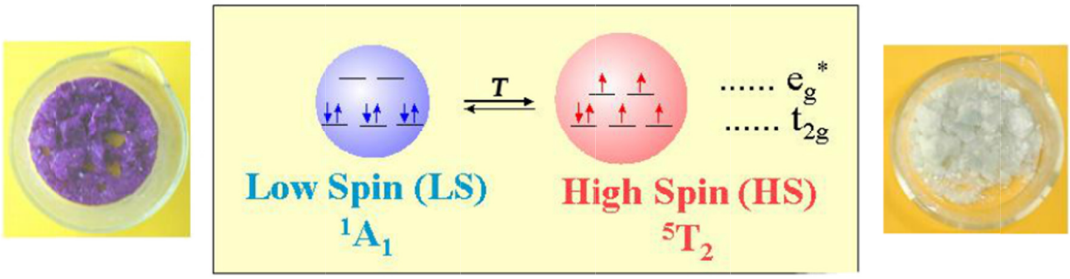

Figure 2.1 The color changes and electron distribution of Fe(II) in the LS and HS states. [9]

The fascinating behavior of these materials has sparked the interest of many research groups. Thus, in 2006, Seredyuk *et al*. [10] reported on a liquid crystals compound which exhibited a strong color contrast between the two states (Figure 2.2). They also showed that, with dehydration of the compound, the transition is more gradual and linear (Figure 2.3).

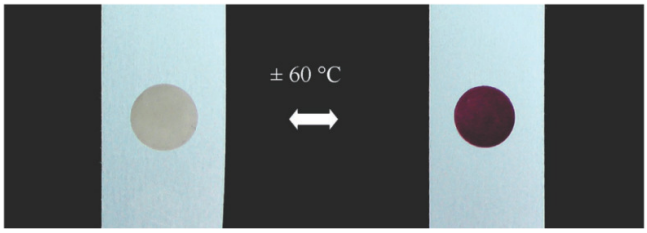

Figure 2.2 Change of color in the SCO liquid crystalline films around 60 °C of $[Fe(C_n\text{-trz})_3](4\text{-}MeC_6H_4SO_3)_2{*}H_2O$ [10].

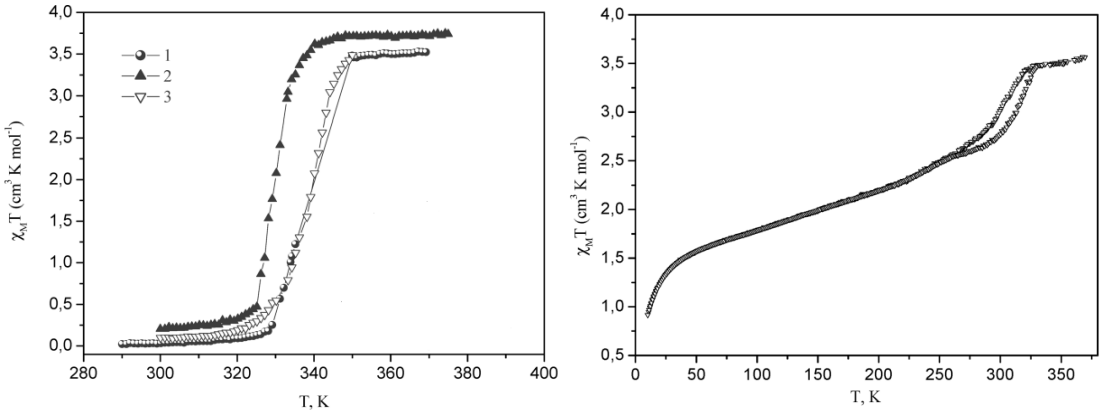

(a) **(b)**

Figure 2.3 The thermal variation of magnetic proprieties of the complexes (a) $[Fe(C_n\text{-trz})_3](4\text{-}MeC_6H_4SO_3)_2{*}H_2O$ (for the cases 1 - n=8, 2 - n=10 and 3 - n=12) and (b) $[Fe(C_n\text{-trz})_3](4\text{-}MeC_6H_4SO_3)_2$ - n=12 [10].

Another interesting compound, exhibiting a great color contrast during the spin state switching, was synthesized by Zhao *et al*. [11]. This compound has the great advantage of an increased stability over time (Figure 2.4a). The transition cycles in Figure 2.4a were measured on $[Fe(Htrz)_2(trz)](BF_4)$ (Htrz=1,2,4-triazole) (SCO-2) particles obtained by the use of the "reverse micelle method".

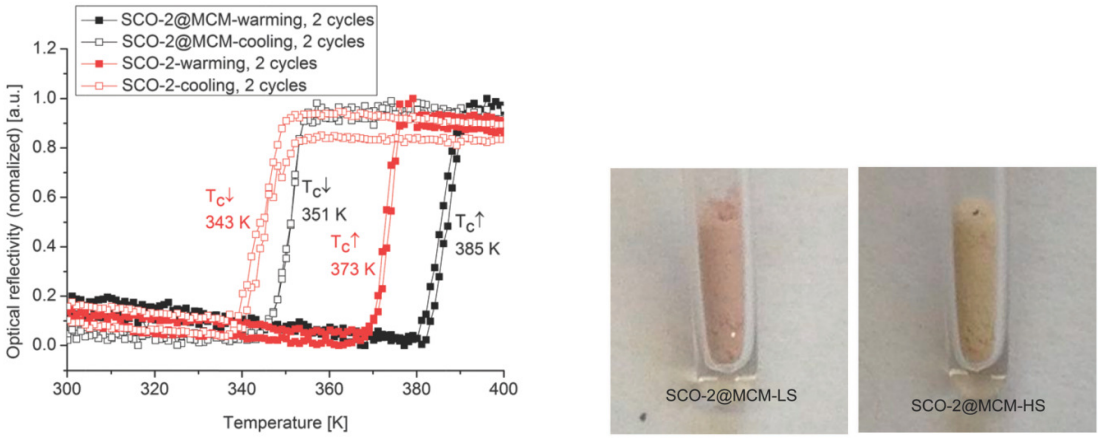

(a) **(b)**

Figure 2.4 (a) Optical reflectivity recorded in function of temperature variation for the SCO compound $[Fe(Htrz)_2(trz)](BF_4)$; (b) The colors in the low spin state (left) and the high spin state (right) for the SCO compound $[Fe(Htrz)_2(trz)](BF_4)$ embedded in the pores of mesostructured silica MCM-41.

The behavior of compounds showing a gradual transition without hysteresis was attributed to weak cooperativity [12] or by diluting the compounds [13]. Figure 2.5 shows examples of SCO compounds exhibiting transitions of this kind.

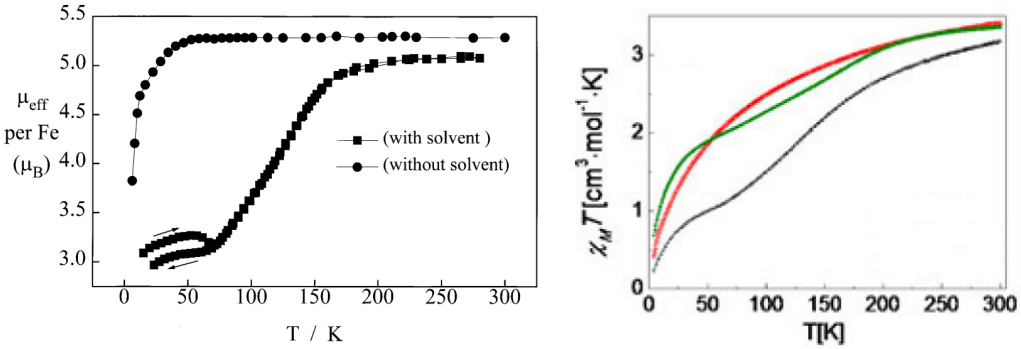

Figure 2.5 (a) Magnetic moment μ_{eff}, per Fe, versus temperature for {[Fe(pypz)$_2$(NCSe)$_2$]$_2$(μ-OH$_2$)(H$_2$O)$_2$}.H$_2$O.MeOH (filled squares), and for its desolvated product (filled circles) [14]; (b) $\chi_M T$ *vs.* T for [Fe(phtptrz)$_3$]I$_2$ - black, [Fe(phtptrz)$_3$](ReO$_4$)$_2$•CH$_3$OH - green and [Fe(phtptrz)$_3$]TaF$_7$•6H$_2$O - red [12].

In Figure 2.6a) is presented a proof-of-concept experiment where a gold microwire (L = 80μm, l = 1μm, h = 5 nm) covered by a thin layer of SCO compound [Fe^{II} (hptrz)$_3$](Ots)$_2$ doped with Rhodamine 110 is heated by Joule effect [15]. The temperature distribution along the wire is presented in Figure 2.6b). The scheme of the device is shown in Figure 2.6 c). The temperature variation is a consequence of the luminescence intensity change. By increasing the temperature the spin state of the compound that cover the gold microwire will change locally from LS to HS state and the luminescence intensity will increase.

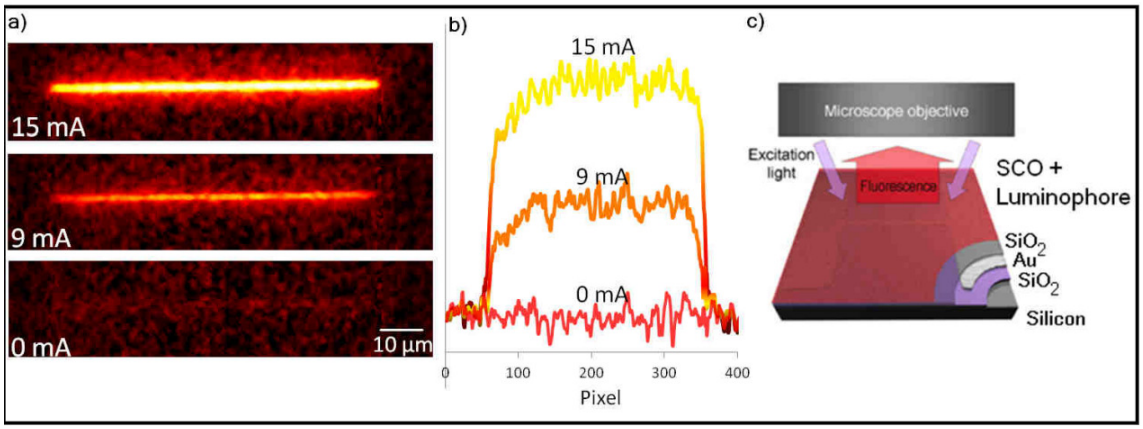

Figure 2.6 Example of sensor using SCO compounds [15]

2.3 Pressure sensors

The pressure effect on a spin transition compound is illustrated in Figure 2.7. It is well known that the molecule's volume in its LS state is smaller than in the HS state. Therefore the application of external pressure promotes the LS state. By applying an external pressure the energy gap increases by $p\Delta V$ as the metal-ligand distances decrease thus lowering the value of the activation energy E_a. ΔV is the molecular volume variation during the spin transition and p is the external applied pressure.

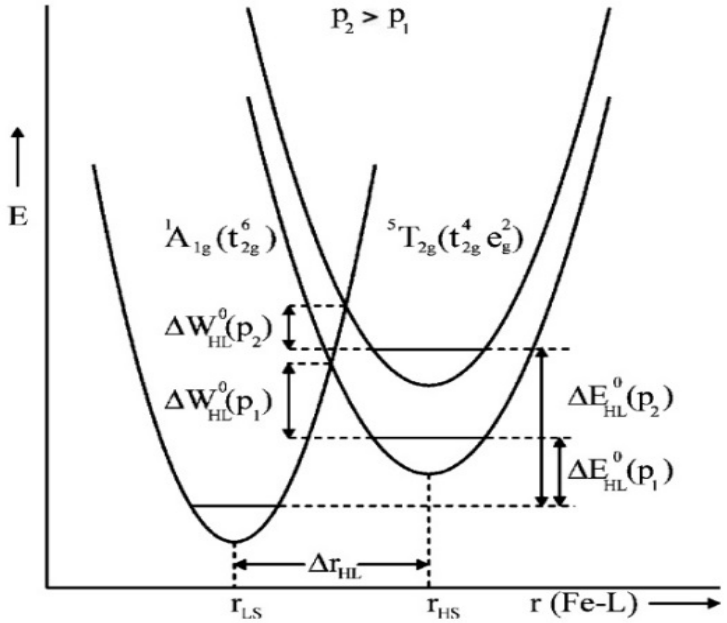

Figure 2.7 Schematic representation of the pressure influence on the LS and HS potential wells of an Fe(II) SCO compound [8].

As previous mentioned, the pressure dependence of the energy gap is given by:

$$\Delta(T, p) = \Delta(T, p = 0) + p\Delta V \tag{2.1}$$

Investigating the [Fe(hyptrz)$_3$](4-chlorobenzenesulfonate)$_2$•H_2O compound, Garcia *et al*. [16] observed that, by increasing the applied pressure, the transition temperatures increases and the width of the hysteresis loop decreases and disappears around 4.1 kbars of pressure. At pressures above 5 kbar the hysteresis loop reappears with a constant width value of 6K (figure 2.8).

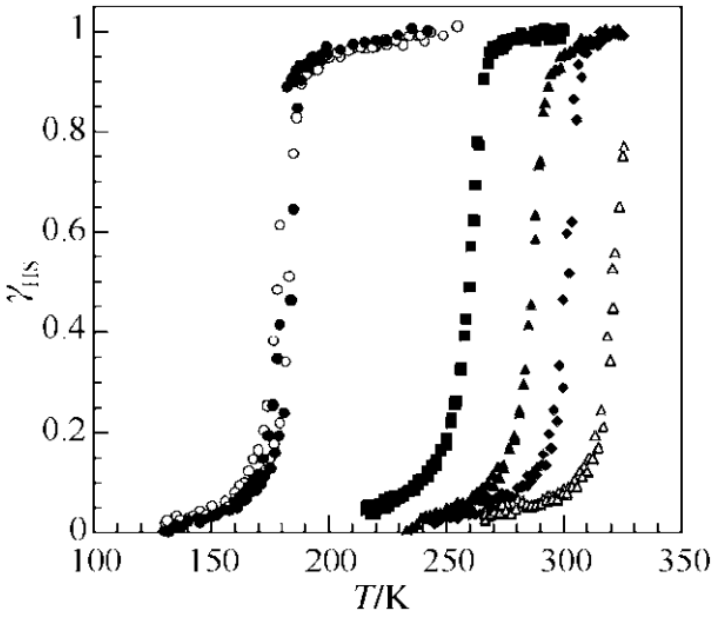

Figure 2.8 The high spin fraction as a function of temperature for [Fe(hyptrz)$_3$](4-chlorobenzenesulfonate)$_2$•H_2O at different pressures (● P=1 bar, ■ P=4.1 kbar, ▲ P=5 kbar, ♦ P=5.3 kbar, ∆ P=5.9 kbar,○ P=1 bar after releasing the pressure) [16]

This behavior was associated to short range interactions due to the presence of triazole molecules which connect the Fe (II) ions. Another similar behavior was reported by Bruns-Yilmaz [17]. In this case the transition occurs in two steps. Much the same as in the previous case, the transition temperatures are shifted towards higher values and the width of the hysteresis loop decreases and even disappears (the second stage hysteresis loop) up to a pressure of 0.4 GPa. It can be seen that, at a pressure of 0.73 GPa, the transition occurs in two steps with hysteresis (Figure 2.9), reappearing on the second stage of the transition hysteresis loop.

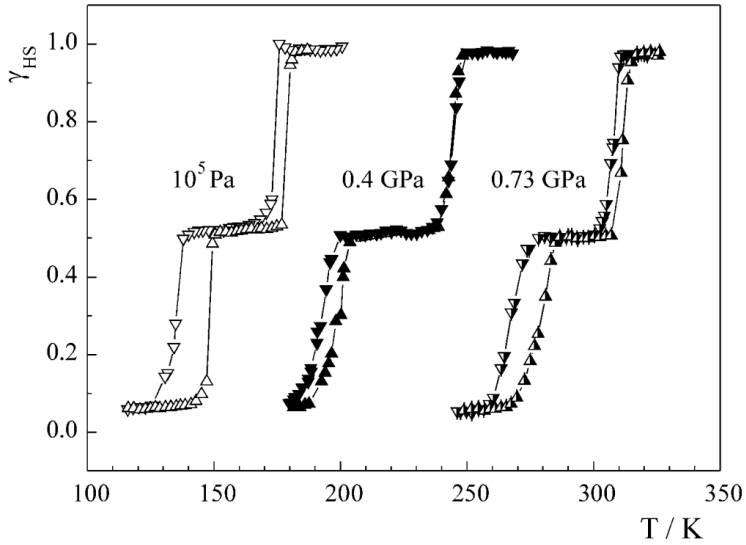

Figure 2.9 The high spin fraction as a function of temperature for [Fe(5-NO_2-sal-N(1,4,7,10))] at different pressures.

In 2003 Bousseksou *et al*. [18] showed that a pressure pulse applied on SCO compound $Fe(phen)_2(NCS)_2$ reveal properties symmetrical of a magnetic pulse applied (figure 2.10).

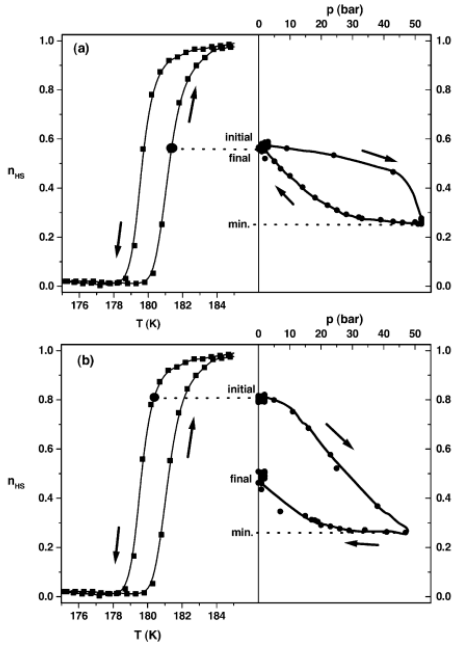

Figure 2.10 The pressure pulse effect on the high spin fraction in $Fe(phen)_2(NCS)_2$ [18]

Studies at constant temperatures and varying the pressure applied has been also recorded [19] (figure 2.11).

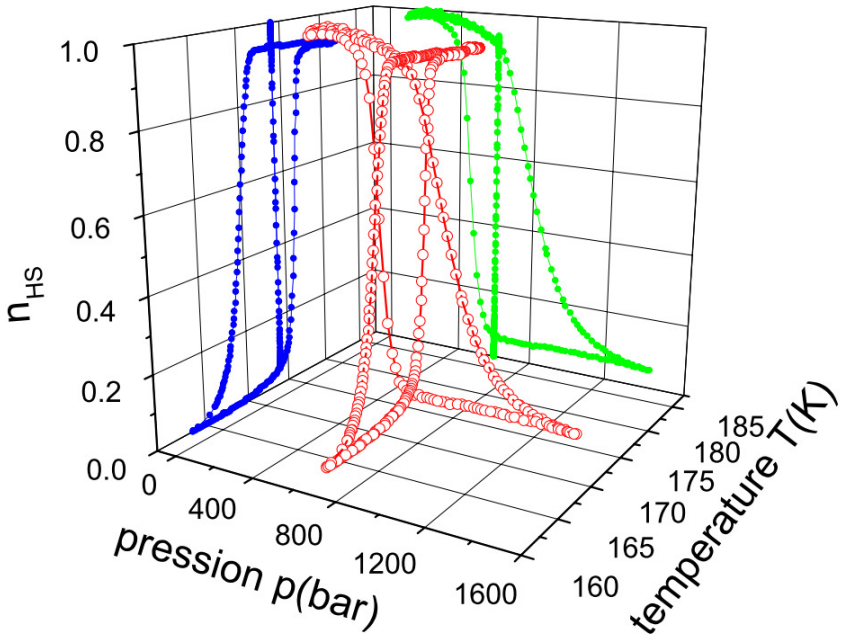

Figure 2.11 Several hysteresis loops recorded at different pressures and temperatures, respectively for $[Fe(PM\text{-}BiA)_2(NCS)_2]$ [19]

Up until a few years ago the SCO compounds exhibiting a thermal hysteretic behavior were intensely studied due to potential application as memory. In the recent years the SCO compounds with gradual and linear transition drew attention of several research groups. This type of behavior accompanied by color changes of the compound opened a new area of implementation, namely the sensors. In 2012 Linares *et al*. [20] proposed a concept of sensor based on SCO compound. The operating principle is shown in Figure 2.12.

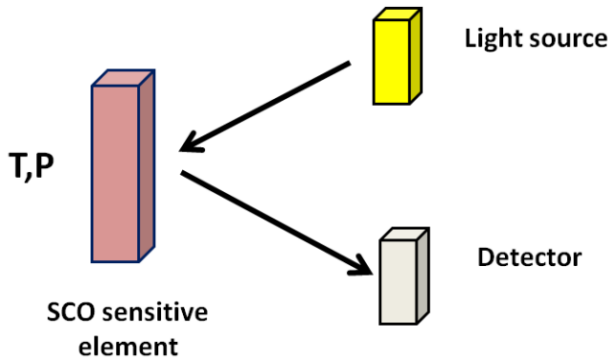

Figure 2.12 The operating principle of a SCO sensor with optical reflectivity detection [20]**.**

This type of sensor can be used for temperature measurement at a well-known pressure or for pressure measurement at constant temperature. It is important to mention that the measurement error is estimated to c.a 20K/kbar rate variation of T vs P [21]. Thus, when the sensor is used for temperature measurement the 1bar variation of pressure induce an error of 20 mK. On the other hand, the pressure measuring can be done with an error of 50 bars at variation of temperature with 1 K. The contrast of the color change of the material plays also an important role in the sensitivity and resolution of measurement process. Using the advantages of these materials such as change in color, repeatability, time responding and the

possibility to be controlled at molecular level, such kind of materials are being commercialized for various applications where a wide selection of colors (Figure 2.13) [22] is necessary.

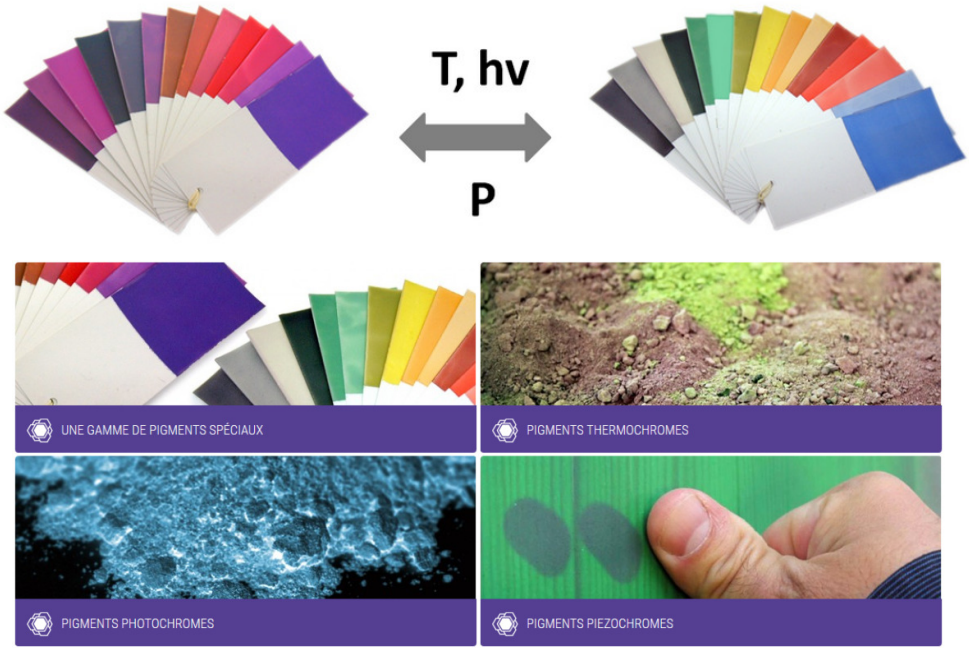

Figure 2.13 Types of pigments and their applications [22].

2.4 Gas sensors

Because the transition can also be chemically induced, certain compounds can be used as chemical sensors (figure 2.14). Compounds such as Fe(pyrazine)[$Ni^{II}(CN)_4$], Fe(pyrazine)[$Pd^{II}(CN)_4$] or Fe(pyrazine)[$Pt^{II}(CN)_4$], in the HS state display a yellow color which may be stabilized in a hydrosillic solvent. In the LS state, these compounds exhibit a reddish-brown color and may be stabilized in a CS_2 solvent.

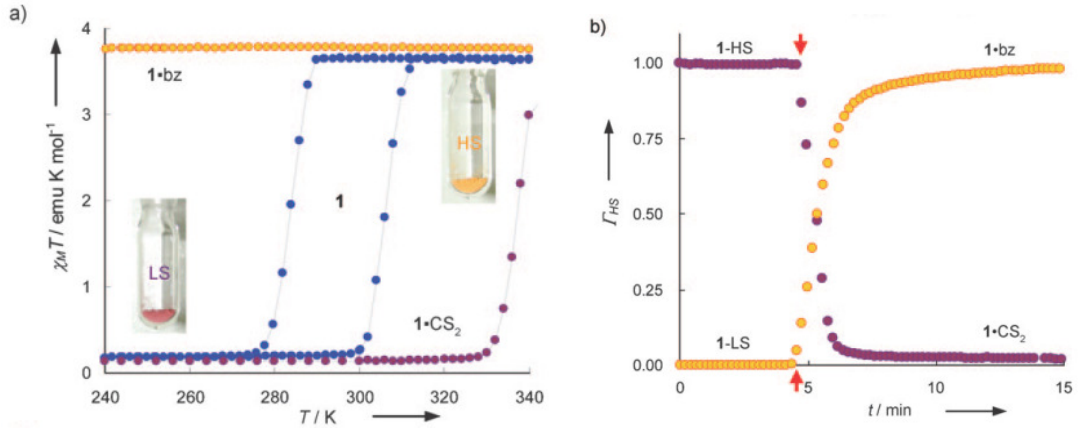

Figure 2.14 a) The temperature dependence of SCO compound Fe(pz)[$Pt(CN)_4$]; b) the time dependence of HS fraction under the action of benzene (yellow) CS_2 (purple) at 293K [23]

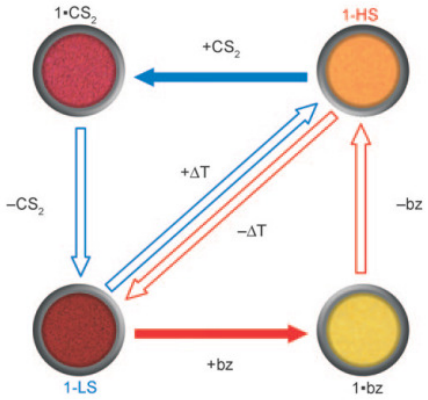

Figure 2.15 The thermal and chemical behavior of $Fe(pz)[Pt(CN)_4]$ [23]

As shown in Figure 2.15 the transition from the LS state to the HS state can be achieved both thermally and chemically. From an initial LS state, the isothermal absorption of benzene by the compound triggers the transition to the HS state. By adsorption of benzene the volume increase by a very low step P/P_0 value of ca. 0.05 and the complete transition from the LS state to the HS state was observed for $P/P_0=0.19$. The HS state is then maintained even after the benzene is eliminated under vacuum. By cooling, the system can return to the initial LS state. If the compound is in the HS state and absorbs CS_2 the transition from the HS state to the LS state occurs due of framework contraction (hardened). After CS_2 is removed in vacuum the compound retains its LS state and, by heating, it can switch back to the HS state [23].

In this context, for use the SCO materials as sensors, for to help to choose the SCO compound for the desired application, the next chapter is dedicated to theoretical studies regarding to the role of cooperativity, edge and architecture effect, in thermal and pressure behaviors of these interesting materials.

2.5 References

[1] N. Tateiwa, Y. Haga, Review of Scientific Instruments 80 (2009) 123901.
[2] R.A. Forman, G.J. Piermarini, J.D. Barnett, S. Block, Science 176 (1972) 284.
[3] M. Baran, V. Dyakonov, L. Gladczuk, G. Levchenko, S. Piechota, H. Szymczak, Physica C 241 (1995) 383.
[4] C. Roux, J. Zarembowitch, J.P. Itie, A. Polian, M. Verdaguer, Inorganic Chemistry 35 (1996) 574.
[5] J. Jeftic, A. Hauser, Chemical Physics Letters 248 (1996) 458.
[6] J. Jeftic, U. Kindler, H. Spiering, A. Hauser, Measurement Science & Technology 8 (1997) 479.
[7] P. Gutlich, A.B. Gaspar, Y. Garcia, V. Ksenofontov, Comptes Rendus Chimie 10 (2007) 21.
[8] A.H. Ewald, E. Sinn, Inorganic Chemistry 8 (1969) 537.
[9] P. Gütlich, Zeitschrift für anorganische und allgemeine Chemie 638 (2012) 15.
[10] M. Seredyuk, A.B. Gaspar, V. Ksenofontov, S. Reiman, Y. Galyametdinov, W. Haase, E. Rentschler, P. Gutlich, Chemistry of Materials 18 (2006) 2513.
[11] T. Zhao, L. Cuignet, M.M. Dirtu, M. Wolff, V. Spasojevic, I. Boldog, A. Rotaru, Y. Garcia, C. Janiak, Journal of Materials Chemistry C 3 (2015) 7802.
[12] M.M. Dîrtu, D. Gillard, A. Naik, A. Rotaru, Y. Garcia, Hyperfine Interactions 205 (2012) 75.
[13] P. Ganguli, P. Gutlich, E.W. Muller, Inorganic Chemistry 21 (1982) 3429.

[14] K.S. Murray, C.J. Kepert, Spin Crossover in Transition Metal Compounds I, 2004, p. 195.
[15] G. Molnar, I.y.A. Gural'skiy, L. Salmon, W. Nicolazzi, C. Quintero, A. Akou, K. Abdul-kader, G. Felix, T. Mahfoud, C. Bergaud, C. Bartual-Murgui, C. Thibault, C. Vieu, A. Bousseksou, in: H.R.R.S.G.A.L.C.S.C. Miuez (Ed.), Photonic Crystal Materials and Devices X, 2012.
[16] Y. Garcia, V. Ksenofontov, G. Levchenko, P. Gutlich, *Journal of Materials Chemistry* **10** (2000) 2274.
[17] C. Bruns-Yilmaz, PhD Thesis, University of Mainz, Germany (1999).
[18] A. Bousseksou, G. Molnar, J.P. Tuchagues, N. Menendez, E. Codjovi, F. Varret, Comptes Rendus Chimie 6 (2003) 329.
[19] R.A. TANASA, Universite de Versailles et Saint Quentin en Yvelines, Versailles, 2006.
[20] J. Linares, E. Codjovi, Y. Garcia, Sensors 12 (2012) 4479.
[21] E. Codjovi, N. Menendez, J. Jeftic, F. Varret, Comptes Rendus De L Academie Des Sciences Serie Ii Fascicule C-Chimie 4 (2001) 181.
[22] O. Company, http://olikrom.com/.
[23] M. Ohba, K. Yoneda, G. Agusti, M.C. Munoz, A.B. Gaspar, J.A. Real, M. Yamasaki, H. Ando, Y. Nakao, S. Sakaki, S. Kitagawa, Angewandte Chemie-International Edition 48 (2009) 4767.

Chapter 3

Cooperativity tuning in spin crossover nanostructures via matrix and architecture effect

Contents

3. Cooperativity tuning in spin crossover nanostructures via matrix and architecture effect

3.1. Introduction

In the past years SCO compounds was intensely studied in order to understand the influence of physical and chemical parameters on the cooperativity in molecular SCO compounds. Thus, it has been shown that both short and long range interactions [1] are present in these molecular materials and play a major role on the behavior of SCO compounds subjected to various external stimuli such as temperature and pressure [2-5], light irradiation [6-8] or magnetic field. More recently, it has been shown that the cooperativity is also strongly affected by the system's size [9,10], the architecture [11,12] or the size of the molecules [13-15]. Up to now, several types of spin transitions, have been reported in the literature, one step transition [16,17] or the stepwise transition with two [18] or three steps [19-21], with equilibrium temperature centered below, above or at room temperature. These transitions can occur with or without hysteresis. At the origin of multi-steps transition is the presence of both the antiferromagnetic-like short range (J) and ferromagnetic-like long range (G) interactions [1,22].

The theoretical studies have given a great importance to the simulation of the thermal behavior of nano-patterned molecular SCO systems. Several approaches have been used by various research groups such as mechano-elastic [23-25], atom-phonon coupling [26-30], Ising like model [31-33] or first order reversal curves (FORC) [13,34]. However, only few experimental studies have been made at nanoscopic scale due to the low signal that could be detected by classical techniques, such as in magnetic or optical measurements. Nevertheless, in the last years it has been shown that a stylish way to investigate the thermal behavior of SCO systems at nanoscopic scale is by using electrical measurements [7,35-37] or surface plasmons detection [38].

The role of cooperativity in SCO materials has attracted great interest from unusual observations revealed experimentally [1-3,19,20,31,39-50]. **The origin of cooperativity** is assigned to elastic interactions between neighboring switching molecules and as a function of the interaction strength among molecules and/or of the lattice architecture, the spin transition (ST) curve can display a variety of shapes which can be gradual, abrupt, or stepwise [51]. Increasing the strength of these interactions, the cooperative phenomena between the spin state changing molecules can lead to a hysteretic behavior. In the last years a special attention has been paid to the two-step behavior which was attributed to a synergistic effect between intra-molecular interactions favoring the mixed-spin state and intermolecular interactions favoring like-spin species domains. In the last five years, several coordination complexes have been shown to present a ST occurring in three steps [19,20,41]. Although the origin of the two-step behavior is rather clear, the origin of the three-step behavior is far from being fully understood. However, there is clear evidence that this stepwise behavior should be governed by both matrix (i.e. surface effect) and long-range interaction effects [52,53].

In the first part of this chapter, a theoretical study concerning the influence of an elastic environment on a SCO system is presented. By reducing the particle's size, the surface contribution became more important comparing with the bulk behaviour. Moreover, the fabrication of a temperature and pressure sensor with optical detection demands the integration of the SCO complexes in a matrix. This make very important to know how SCO behavior is influenced by the interaction of SCO molecules with their environment. Thus, the edge effect might play an important role on the spin crossover behavior. Indeed, it has been shown that the edge effect could led through a multi-step behavior. This kind of behavior has

been experimentally observed in 2D and 3D SCO systems [19,20,41] but not yet for 1D systems. We used Ising-like model [31,49,50] in order to simulate the edge effect in SCO systems. These studies are very important for engineers in the fabrication process of temperature and pressure sensors.

In the second part of the chapter is analyzed the architecture effect of a SCO system.

The Ising-like model with short-range (J) and long-range interactions (G) [31], presented in the first chapter, has been used in several studies to reproduce different experimental behaviors such as a one-step transition [1,31,42] or a two-step [43] transition, with or without hysteresis. The two steps SCO curve was attributed to the interplay between an antiferromagnetic (AF) short-range interaction and a ferromagnetic (F) long-range interaction. Example of two-steps transition has been also reported as a consequence of binuclear molecules [48] or two-sub-lattices [49,54].

3.2. Matrix effect on spin crossover nanoparticles on the origin of multi-step spin transition behavior in 1D nanoparticles

3.2.1. The Ising-like model with edge effect

It is known that the SCO compounds that exhibit hysteresis can be used as memories and those whose transition is gradual can be used as sensors. Thus, compounds with gradual transition can be obtained by synthesis or may be diluted compounds that exhibit transition with hysteresis. By dilution the system cooperativity is reduced and can appear new interactions if the compounds are mixed for example with paints. In order to take into account these new interactions (the matrix effect), we have added an additional interaction parameter to the Ising-like Hamiltonian [31] which accounts for the SCO molecules behavior within the environment (matrix effect), that is termed, the matrix interaction L. This interaction is assumed to act on the molecules localized at both ends of the 1D SCO system. In this case, the system's Hamiltonian can be written as follows:

$$H = \frac{\Delta - k_B T \ln g}{2} \sum_{i=1}^{N} \sigma_i - G \sum_{i=1}^{N} \sigma_i < \sigma > - J \sum_{\langle i,j \rangle} \sigma_i \sigma_j - L \sum_{\{i=1; i=N\}} \sigma_i \,, \tag{3.1}$$

where the first term represents the temperature dependent field, the second and third terms are describing the long- and short-range interactions, respectively. The last term describes the interaction of the SCO system with the matrix. Δ is the energy gap between the high-spin (HS) and low-spin (LS) states, and g is the degeneracy ratio of the two states.
Since the ratio of HS state n_{HS} as a function of the pseudo-spin variable can be expressed by:

$$n_{HS} = \left(1 + \langle \sigma \rangle\right) / 2 \tag{3.2}$$

and appears self-dependent of $<\sigma>$, we propose an analytical treatment using a new expression of n_{HS} based on the bisection technique.
Thus, the system's Hamiltonian could be expressed as a function of the dimensionless macroscopic variables:

$$m = \sum_{j=1,N} \sigma_j \tag{3.3}$$

$$s = \sum\nolimits_{<i,j>} \sigma_i \sigma_j \quad \text{and} \tag{3.4}$$

$$c = < \sigma_1 + \sigma_N > \tag{3.5}$$

(herein σ_1 and σ_N represent the spin operator associated to the first and the last molecule in the molecular chain):

$$H = \left(\frac{\Delta - k_B T \ln g}{2} - G\langle \sigma \rangle \right) m - Js - Lc \tag{3.6}$$

The canonical expression of <σ> can be constructed in terms of the above dimensionless quantities:

$$< \sigma >= \frac{\sum_{j=1,NL} \frac{m_j}{N} d(m_j s_j c_j) \exp\left(-\frac{1}{k_B T} (-h_f m_j - J s_j - L c_j) \right)}{\sum_{j=1,NL} d(m_j s_j c_j) \exp\left(-\frac{1}{k_B T} (-h_f m_j - J s_j - L c_j) \right)} \tag{3.7}$$

where *d(m,s,c)* is the number of configurations for a given set of values, *NL* is the number of distinct configurations of states <*m,s,c*> and where:

$$h_f = -\left(\frac{\Delta - k_B T \ln g}{2} - G\langle \sigma \rangle \right) \tag{3.8}$$

Since *d(m,s,c)* is the degeneracy of each state <*m,s,c*>, we are able to generate all the system configurations building by this way, the states distributions of the molecular system.

Upon considering open boundary conditions and following the numerical calculation of equation (3.7) from the bisection technique, the curves from Figures 3.1 and 3.2 were obtained where n_{HS} is given by equation (3.2). Moreover we discuss in the rest of the study some simulations regarding the behavior of a 1D system using the values of parameters *Δ*, *ln(g)* in the range of those of SCO compounds.

In the numerical studies [42,55] it was shown that a stepwise behavior could be obtained in 3D SCO systems by taking into account negative short-range interactions (anti-ferromagnetic-like interactions) and positive long-range interactions (ferromagnetic-like interactions). Following similar conditions, it is further considered in this work, that the coupling between the matrix and the edge molecules is ferromagnetic-like (positive).

3.2.2. Results and discussions

The results on the influence of the SCO-matrix interaction strength are reported in figure 3.1. By increasing the value of *L*, the 1D SCO system goes from a complete two-steps behavior (L/k_B = 90 K, with k_B the Boltzmann constant) to a complete three-steps behavior for an interaction strength between the matrix and the boundary molecules given by L/k_B = 147 K. Moreover, an incomplete two-steps transition is obtained for higher values of L/k_B = 180 K. These results are to be compared to the incomplete behavior induced by the SCO-matrix interaction strength that were recently reported by Stoleriu *et al*. [10] in the framework of the mechano-elastic model. In their paper, it was concluded that the nanoparticle system behavior is affected drastically by the matrix environment upon decreasing the nanoparticles system's size. Atitoaie *et al*. [56] and Muraoka *et al*. [57] have also studied the effect of the environment on the SCO behavior.

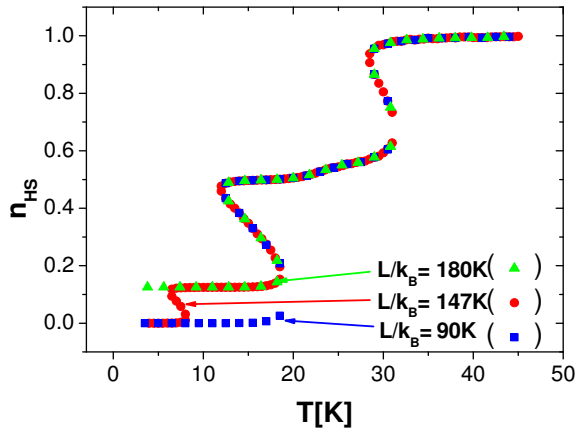

Figure 3.1 Thermal evolution of the HS molar fraction, n_{HS}, in a 1D SCO system embedded into a matrix for different matrix interaction strength: Square (L/k_B = 90 K), Circle (L/k_B = 147 K) and Triangle (L/k_B = 180 K). The parameter values are: N = 16 molecules, Δ/k_B = 240 K, ln(g) = 9.5, G/k_B = 120 K, and J/k_B = -43 K.

In the past years, particular attention was paid to the influence of size effect in the frame of the nano-structuration of SCO complexes [58]. Since the hysteretic behavior of the SCO systems is strongly affected by the decrease in the number of molecules, many studies were reported on the critical size, under which the SCO system losses its hysteretic properties. Rotaru *et al*. [13] studied a series of nanoparticles of the surfacted $[Fe(NH_2trz)_3]Br_2 \bullet 3H_2O$ (NH_2trz = 4-amino-1,2,4-triazole) SCO complex, with various mean sizes (30-110nm) using first-order reversal curves (FORC). They have shown that the critical size is around 45-50nm. On the other hand, SCO systems with a critical size below 10 nm have been also reported [59]. The size effect in SCO systems exhibiting a three-step behavior has however not been studied so far. For this reason, we present in the following, a study on the size influence on 1D SCO system exhibiting a stepwise thermal behavior.

In figure 3.2, the simulated thermal behavior of the HS fraction is shown for various numbers of molecules. We show that, when the SCO system size consists of a high number of interacting molecules, the thermal behavior of the 1D SCO system, depending on the matrix interaction strength, can exhibit both two-step and three-step ST and both complete or incomplete transition. However, when the system's size is decreasing, the coupling between the edge molecules with the matrix becomes more important and the synergistic effect between intra-molecular interactions favors the mixed-spin state configuration. Thus, with the decrease of the system's size, the SCO particles embedded into a matrix can exhibit even a four-step behavior. As it was expected, the decrease of the system's size also affects the increase of the residual HS fraction, for high values of the matrix interaction parameter. Another feature that was observed with the decrease of the number of molecules, is a shift of the equilibrium temperature $T_{1/2}$ to low temperatures, in good agreement with the experimental data reported in [9].

Because in our model the edge atoms are not blocked in the HS state, it is difficult to give an evolution of $T_{1/2}$ as a function of all the system's parameters (i.e. Δ, $ln(g)$, J, G and L). A particular aspect which should be noted here is the fact that different cooperative effects at small nanoparticles sizes were obtained, in good agreement with the results reported by Tokarev *et al*. [15] for of $[Fe(NH_2trz)_3](tosylate)_2$ nanoparticles of 3-4nm in size.

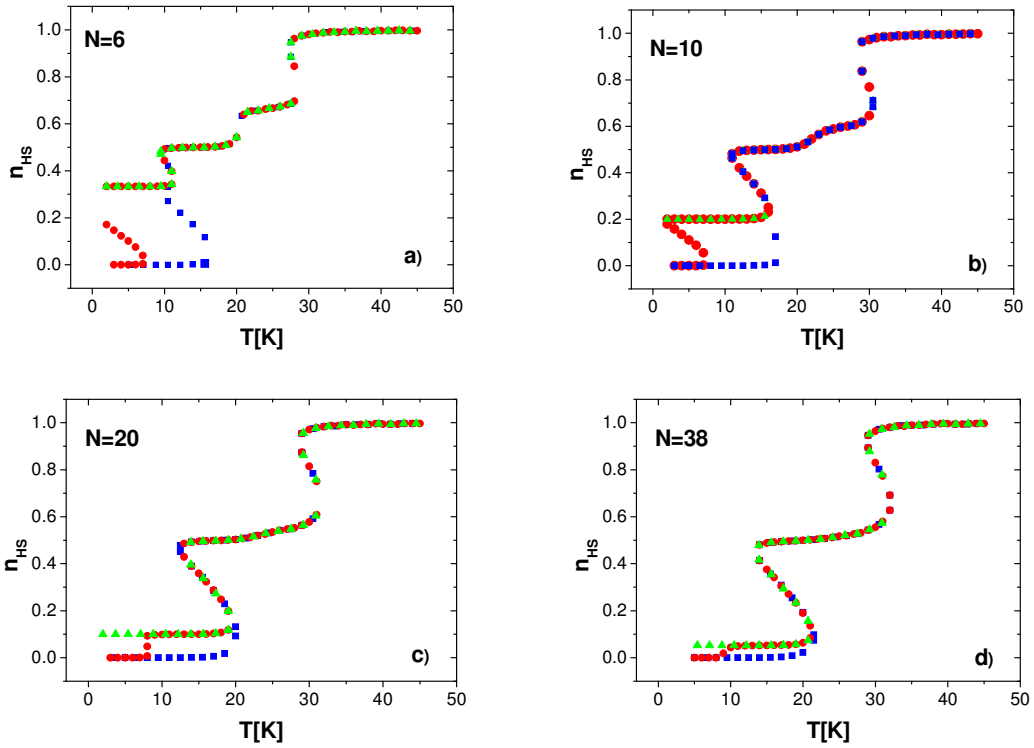

Figure 3.2 Evolution of the HS molar fraction, n_{HS}, as a function of temperature, for various numbers of molecules: (a) N=6 molecules, (b) N=10 molecules, (c) N=20 molecules, (d) N=38 molecules for different polymeric-interactions strength: Square (L/k_B = 90 K), Circle (L/k_B = 147 K) and Triangle (L/k_B = 180 K). The computational parameters are: Δ/k_B = 240 K, ln(g) = 9.5, G/k_B = 120 K, and J/k_B = -43 K.

In figure 3.3 we show the case where *L* as well as *J*, the short range interaction are 0, together with the case with L/k_B = 147 K and J/k_B = -43 K. It is clear from this figure that the multi-steps hysteresis transition originates from the interaction of the border SCO molecules with the local environment together with an antiferromagnetic-type short range interaction.

The value of the parameter *L*, which is a "long-range interaction" between the matrix and the SCO at the surface, is of the same order with the long-range interaction parameter *G*.

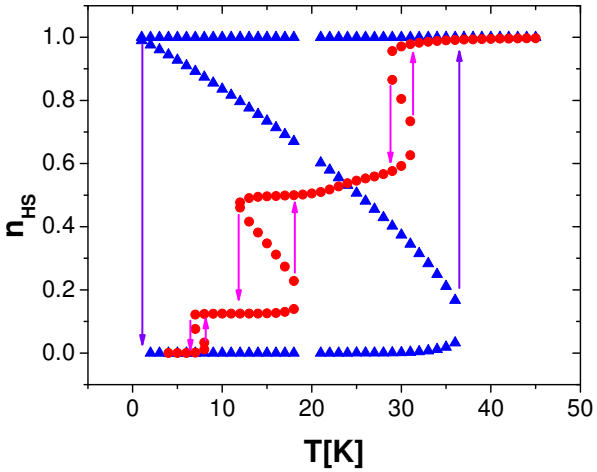

Figure 3.3 Evolution of the HS molar fraction n_{HS} as a function of temperature, for the case: (Circle) (L/k_B = 147 K, J/k_B = -43 K) and (Triangle) (L/k_B = 0 K, J/k_B = 0 K). The computational parameters are: N=16, Δ/k_B = 240 K, ln(g) = 9.5 and G/k_B = 120 K.

The role of the long-range (G), as well as the short-range interaction, on the thermal behavior are presented in figure 3.4 and figure 3.5 respectively. For a high value of the long-range interaction, three-step hysteretic behavior can be reproduced, however the hysteresis disappears, as we expected, for small values of the long-range interaction.

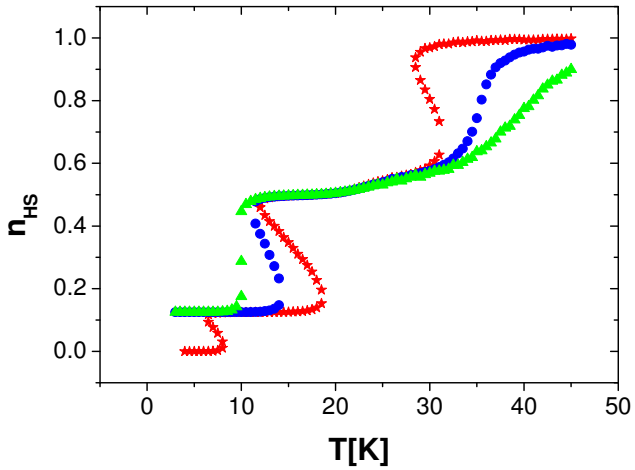

Figure 3.4 Evolution of molecules in the HS state, n_{HS}, as a function of temperature, for a 1D system N= 16 molecules, for different long range-interactions strength: G/k_B = 40 K (triangle), G/k_B = 80 K (circles), G/k_B = 120 K (star) The parameter values are Δ/k_B = 240 K, ln(g) = 9.5, J/k_B = -43 K, and L/k_B = 147 K.

The short-range interaction strength plays an important role on the stepwise behavior. Thus, when the short-range interaction strength dominates the other two interactions parameters, i.e. long-range and the matrix interaction parameters, the stepwise behavior is more pronounced. For a small value of short-range interaction, the stepwise behavior can be masked by a macroscopic one-step behavior.

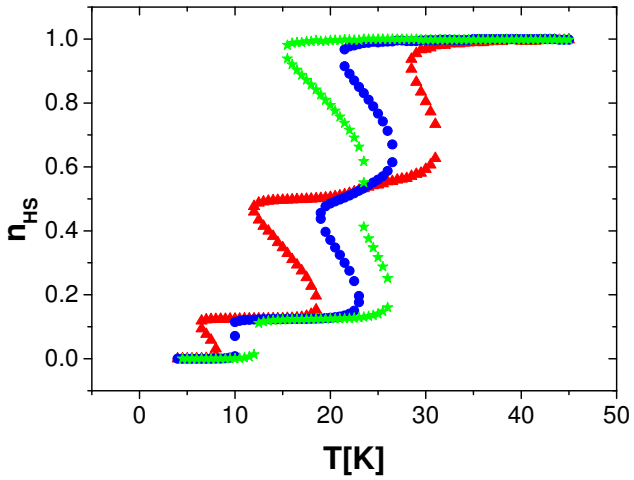

Figure 3.5 Evolution of molecules in the HS state, n_{HS}, as a function of temperature, for a 1D system N= 16 molecules, for different long short-interactions strength: J/k_B = -43 K (triangle), J/k_B = -30 K (circle) and J/k_B = -20 K (star). The parameter values are Δ/k_B = 240 K, ln(g) = 9.5, G/k_B = 120 K, and L/k_B = 147 K.

3.3. Matrix and size effects on the appearance of the thermal hysteresis in 2D spin crossover nanoparticles.

This study aims at addressing the investigations on SC nanoparticles on which an extensive work has been devoted this last decade, both from the chemical point of view by synthesizing new core-shell systems [60-62] and from the theoretical side, in which some attempts to explain the interplay between the matrix and the SCO properties [42,57] have been developed.

Here, we consider this problem in the frame of the Ising-like model in which we include the effect of the environment on the SC nanoparticles and we study its impact on the macroscopic thermal properties of the system.

3.3.1. Results and discussions

Adapting the Hamiltonian expressed in equation (3.1) to a 2D system type the new Hamiltonian can be expressed as:

$$H = \frac{\Delta - k_B T \ln g}{2} \sum_{i=1}^{N} \sigma_i - G \sum_{i=1}^{N} \sigma_i < \sigma > -J \sum_{\langle i,j \rangle} \sigma_i \sigma_j - L \sum_{\{i=edge \quad molecules\}} \sigma_i \qquad (3.9)$$

The molecules situated at the surface of the nanoparticle can be considered to be at the interface between the nanoparticle and its immediate environment (matrix, air, …) and therefore, it is legitimate to consider that they have specific properties. figure 3.6 illustrates the thermal-dependence of the HS fraction for an isolated SC nanoparticle having a homogeneous and constant ligand field on all sites including those located at the surface. Obviously, this situation corresponds to the case where L=0 in Hamiltonian given by equation (3.9).

The Hamiltonian (equation (3.9)) was exactly solved in the canonical approach, using parameter values chosen from typical data in spin-crossover literature, such as, Δ/k_B=840K, J/k_B=10K, G/k_B=115K, ln(g)=6.9 (leading to a molar entropy change $\Delta S \approx 56$ J.K-1.mol-1), except for L which is a variable parameter.

This study is carried out for several lattice sizes, containing a number $N = N_x \times N_y$ of molecules. The results of figure 3.6. show that, in all cases, a first-order transition is observed whose thermal hysteresis loop increases in width with the lattice size. As it was expected, the equilibrium temperature $T_{1/2} = \frac{\Delta}{k_B \ln g} = 121.7K$ remains size-independent.

Figures 3.7 displays the associated phase diagram Δ/k_B as a function of T for two values of the size, N=30 (5x6) and N=16 (4x4). Let's consider the case N=30. For a compound with Δ/k_B higher than the critical ligand field value, Δ_C/k_B=997K, the spin transition from the LS state to the HS state occurs gradually, i.e. without thermal hysteresis. It is worth to notice that if for some reason (like, the interaction of the SC nanoparticle with some surrounding shell) the average value of Δ/k_B decreases to the extent that Δ/k_B becomes smaller than the critical value Δ_C/k_B, then the thermal hysteresis may not appear.

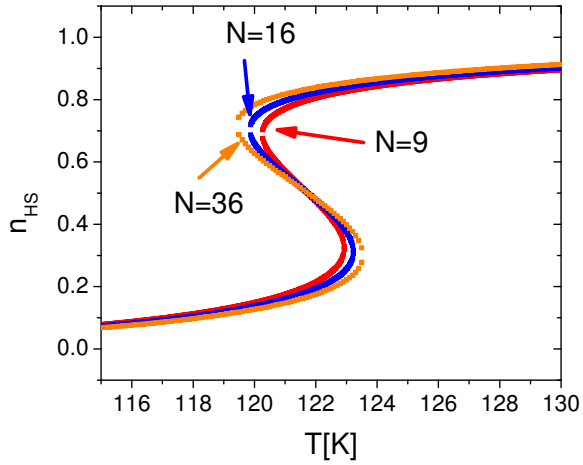

Figure 3.6 Simulated thermal dependence of the HS fraction for 2D SCO system for three numbers of molecules, showing the dependence of the thermal hysteresis on size. Parameters values, used in calculations, are: Δ/k_B=840K, J/k_B=10K, G/k_B=115K, L/k_B=0K, ln(g)=6.9.

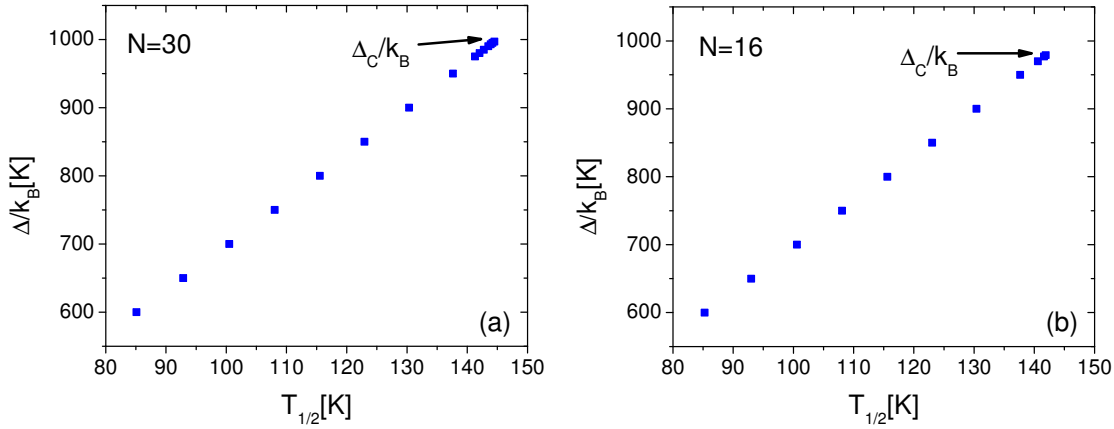

Figure 3.7 Phase diagram in $T_{1/2}$-Δ coordinates for an isolated SC nanoparticle of size (a) N=30 and (b) N=16, leading to the respective critical ligand field values Δ_C/k_B=997K and 979K. The parameter values are the same as those of figure 3.6.

We have made extensive simulations of thermal dependences of the HS fraction for different ligand field values and various nanoparticle sizes. For each size, we determined the critical ligand field above which the first-order spin transition vanishes. The results are summarized in figure 3.8, where we represent the size dependence of these critical Δ/k_B-values. It is important to notice that the critical value of the energy gap increases with N till saturation, which occurs for Δ_C/k_B ~1000K, corresponding more or less to a Δ_C/k_B value at the thermodynamic limit.

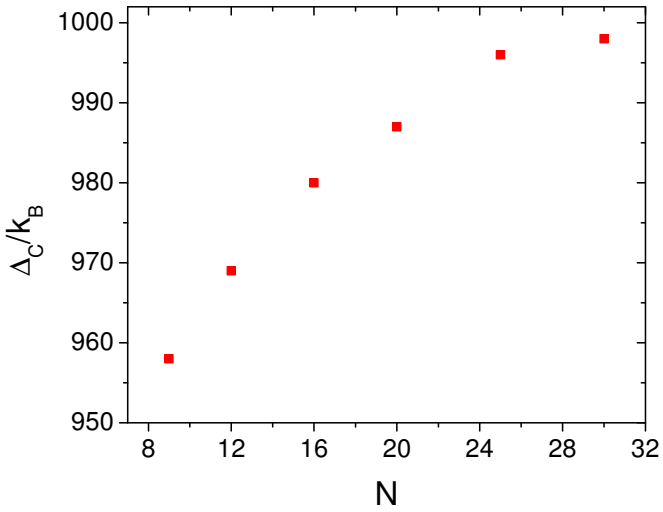

Figure 3.8 Size-dependence of the critical ligand field showing a monotonous increase and a saturation indicating the proximity of the thermodynamic limit. The parameter values are the same as those of figure 3.6.

In the second part of this section, the problem of a 2D SC nanoparticle under the influence of a matrix or a shell was explored. In this case, the parameter *L* in equation (3.9), accounting for the existence of a specific ligand field of the edge atoms, becomes significant. The thermal behavior of a 2D SC system including surface effects is reported in figure 3.9, for various value of the system's size. We observe that, contrary to the case of an isolated nanoparticle (see figure 3.6), now the transition temperature $T_{1/2}$ shifts to higher temperatures with the nanoparticle size, while concomitantly the width of the thermal hysteresis shows a very unusual trend, since it increases when the nanoparticle size decreases. One of the important conclusions arising from these results is, as a result of surface effects, the emergence of the first-order transition at small sizes, which was absent at bigger sizes. This surface-driven first-order transition, is a result which is very original, and to the best of our knowledge it was never reported in the theoretical literature. The phase diagram giving the size-dependence of the critical ligand-field, $\Delta_C/k_B(N)$, is presented in figure 3.10. Now, $\Delta_C/k_B(N)$ is an increasing function of the size, a behavior which clearly contrasts with the case of the isolated nanoparticle, as given in figure 3.8.

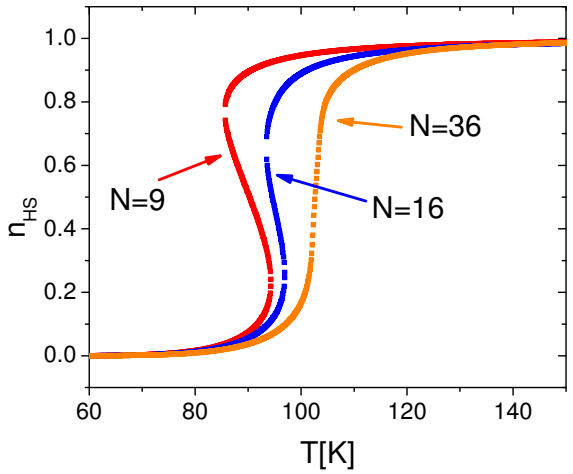

Figure 3.9 Simulated thermal dependence of the HS fraction for 2D SCO nanoparticle including surface effects, for three increasing numbers of molecules. Remark the behavior of the thermal hysteresis width and equilibrium temperature with size. The parameter values are the same as those of figure 3.6, except for L/k_B=120K.

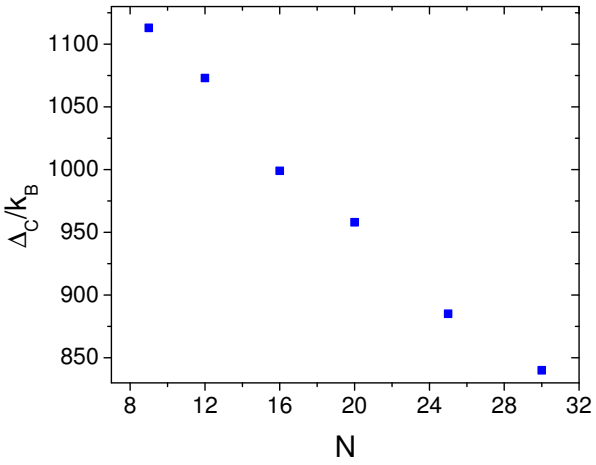

Figure 3.10 Size-dependence of the critical value of the energy gap as function of the number of molecules for a 2D SC system embedded into a matrix. The computation parameters are the same as those of figure 3.9.

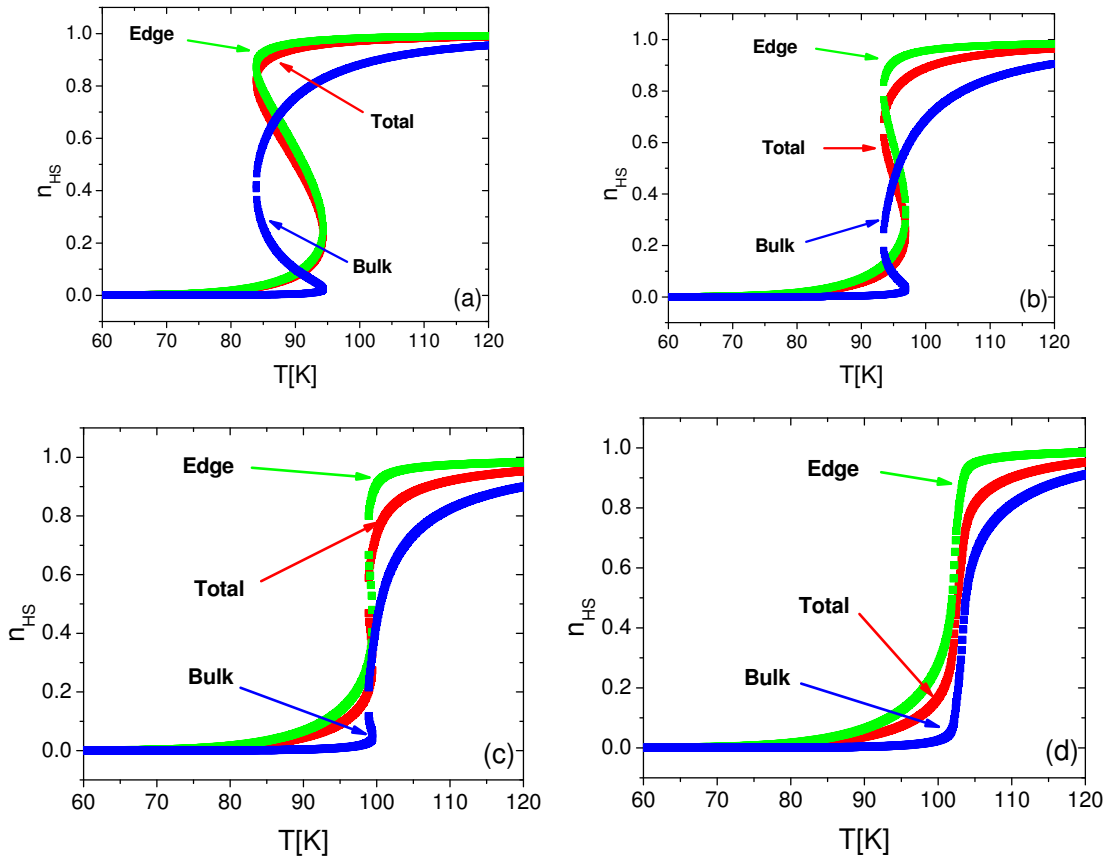

Figure 3.11 Thermal evolution of the high spin molar fraction, n_{HS}, for a 2D system embedded into a matrix for the sizes: (a) N=9 (3x3), (b) N=16 (4x4), (c) N=25 (5x5) and (d) N=36 (6x6). The parameter values are: Δ/k_B=840K, J/k_B=10K, G/k_B=115K, L/k_B=120K and ln(g)=6.9.

To disentangle the surface and the bulk contributions in the thermal dependence of the total HS fraction of figure 3.9, we have calculated the thermal evolution of the HS fraction corresponding to each of them, for various sizes, that we illustrate in figure 3.11. It is clearly shown in this figure that the thermal dependence of the surface (green curve) and bulk (blue

curve) contributions are dramatically influenced by the ratio of the numbers of edge/bulk (surface/volume in 3D) molecules. Thus, for the first case (figure 3.11a) for which the ratio is 8:1, meaning that that the surface is dominant, the thermal behavior of the system is mainly governed by that of the edge molecule. The expected transition temperature $T_{1/2}(surface) = \frac{\Delta - 2L}{k_B \ln g} \approx 87K$ is significantly different from that of the bulk system, given by $T_{1/2}(bulk) = \frac{\Delta}{k_B \ln g} \approx 121.7K$ and is in excellent agreement with the simulation. The influence of edge molecules on the global behavior of the system (red curve), weakens as the system size increases, which is confirmed by the shift of the transition temperature towards that of the bulk material. However, despite these simple considerations, the thermal behavior dependence on the bulk and the edge HS fractions is quite complex (see the shapes of the blue curves), due to their interplay and a complete description will be developed elsewhere.

3.4. Simulation of multi-steps thermal transition in 2D SCO nanoparticles

The surface interaction parameter is assumed to act on the edge molecules of the system, which are represented in blue color in figure 3.12 where a 2D such system is illustrated.

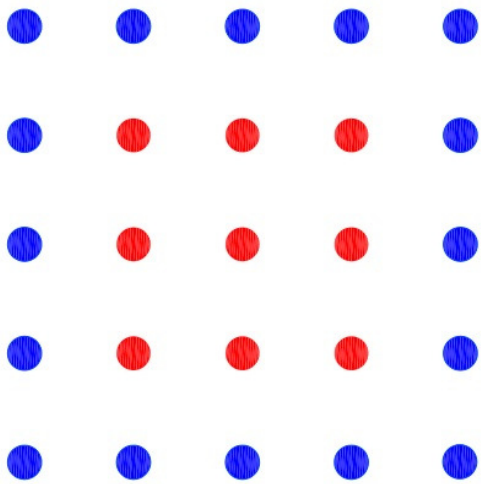

Figure 3.12 Schematic representation of a 2D SCO system with 25 molecules (5x5). Blue full circles represent the edge molecules and red full circles represent the inner molecules.

3.4.1. Results and discussions

Keeping the same signs for the short and long range interactions as it was reported in [22,35] and applying in the numerical calculation of equation (3.7), the bisection technique to a system of 25 molecules (5x5) with 16 edge molecules, the stepwise thermal behavior was plotted as shown in the figure 3.13. The high spin fraction, n_{HS}, was obtained from equation (3.2)) We have considered an open boundary condition for the matrix system.

From figure 3.13 we can see that a four steps hysteresis transition was obtained. To understand the role of a negative short range interaction that is responsible for a multi-steps transition [22,55] and the role of the interaction parameter between the edge molecules and the environment we have also performed calculations that gave results reported in figure 3.14. The behavior of the system when both parameters are 0 is plotted in figure 3.14 (a). In figure

3.14 (b) and 3.14 (c) are presented the evolution of the HS fraction when the short range interaction parameters (in figure 3.14 (b)) and the interaction parameter with environment (in figure 3.14 (c)) are 0, respectively.

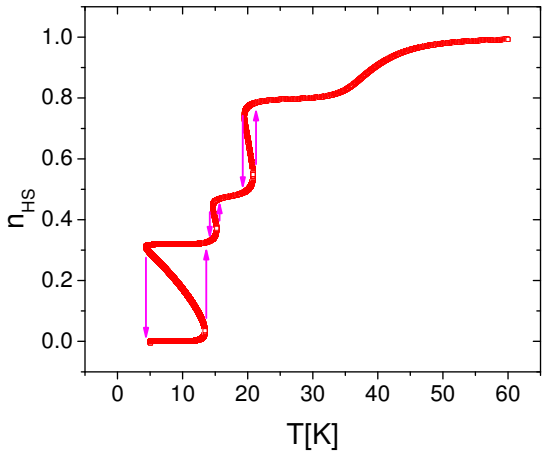

Figure 3.13 The evolution of the high spin fraction, n_{HS}, of all system molecules. The computational parameters are: N=25, Δ/k_B=320 K, J/k_B=-29 K, G/k_B=120 K, L/k_B=107 K, ln(g)=9.1.

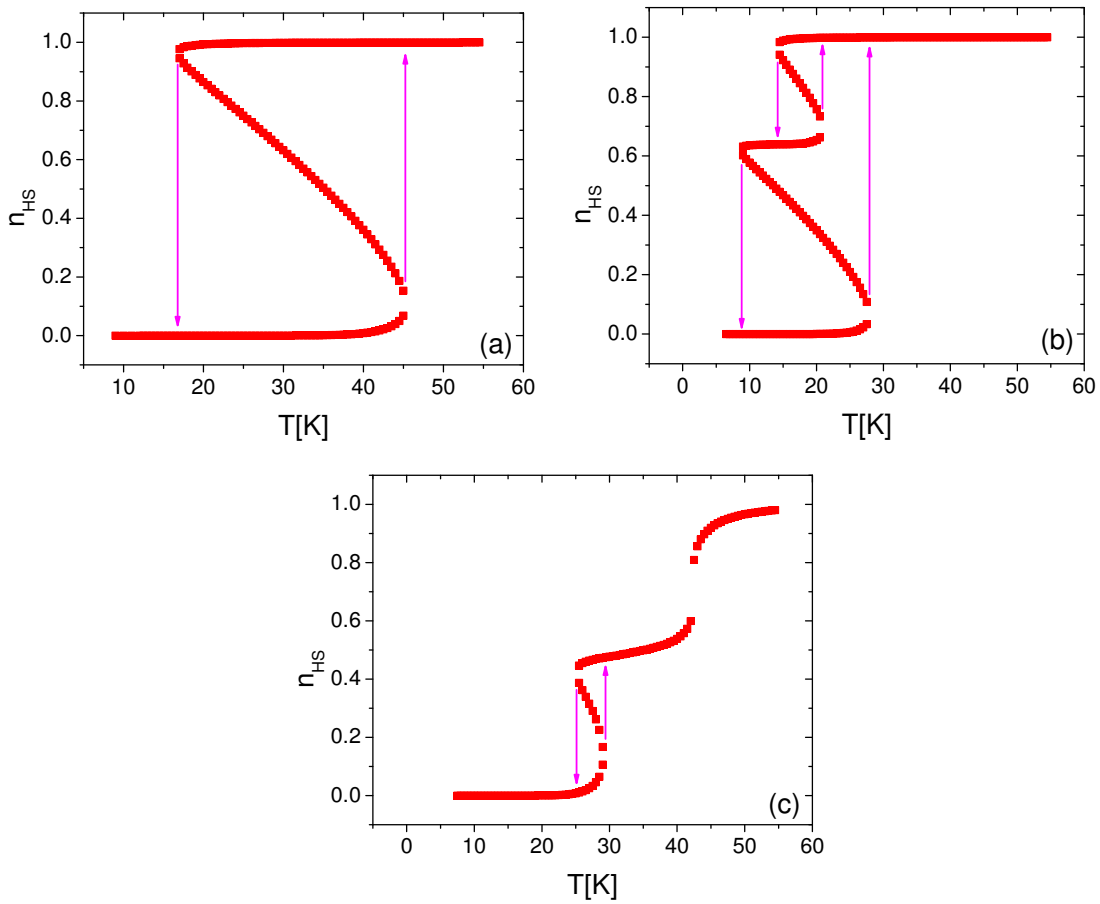

Figure 3.14 Thermal evolution of the HS molar fraction, n_{HS}, in a 2D SCO system embedded into a matrix for the case: a) J/k_B=0 and L/k_B=0, b) J/k_B=0 and L=/k_B=107 K, c) J/k_B=-29 K and L/k_B=0 K. The computational parameters are: N=25 (5x5), Δ/k_B=320 K, G/k_B=120 K, ln(g)=9.1.

It is clear from these two figures that both short-range interactions and the interaction between edge SCO molecules and its local environment can trigger the multi-step hysteresis transition.

The size effect on the thermal behavior of a 2D SCO system embedded into a matrix has also been studied. As can be seen from figure 3.15, by decreasing the system's size, the ratio between edge and inner molecules is higher and the influence of interaction between the edge SCO molecules with environment becomes more important than the influence of the inner SCO molecules on the thermal behavior of the system. For N=9, for example, no multi-steps occurs for the inner molecules whereas for N=36, a stepwise transition from LS to HS occurs.

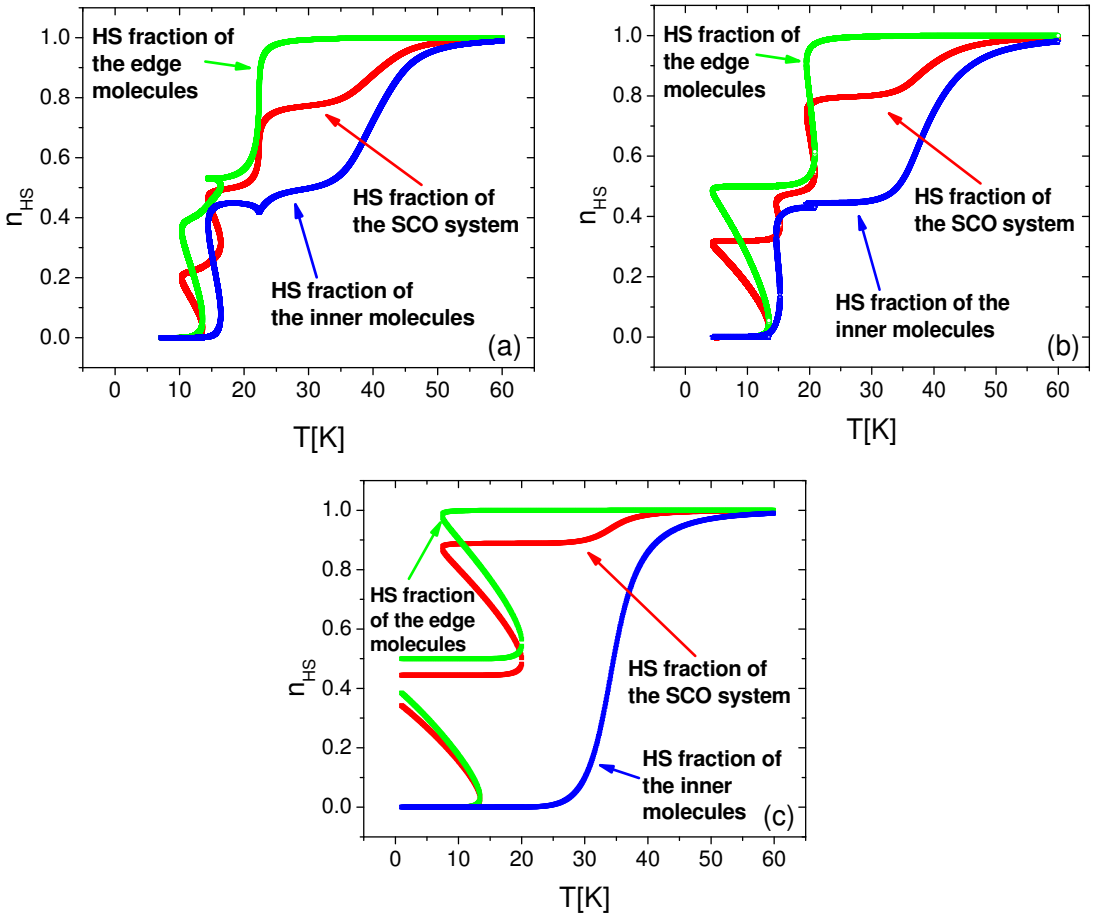

Figure 3.15 Thermal evolution of the HS fraction for different system's size: (a) N=36 (6x6), (b) N=25 (5x5), (d) N=9 (3x3). The computational parameters are: Δ/k_B=320 K, J/k_B= -29 K, G/k_B=120 K, L/k_B=107 K, ln(g)=9.1.

3.5. Analysis of edge effect in 3D systems

3.5.1. Results and discussions

In this study, we first consider a 3D SCO system whose edge metallic centers interact with its environment and apply the bisection technique to equation (3.7). The HS fraction, n_{HS}, is derived from equation (3.2). The SCO selected system contains 125 metallic centers (5x5x5) of which 98 are surface metallic centers and only 27 are inner metallic centers. A typical distance between metal centers of about 9 Å [63] is taken into account corresponding to a cubic sampling of 3.6 nm x 3.6 nm x 3.6 nm. As a result, a hysteretic multi-steps transition is predicted (figure 3.16).

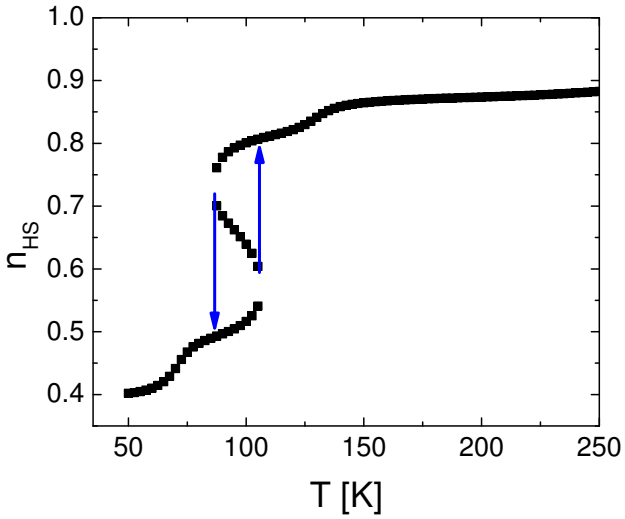

Figure 3.16 Simulated HS fraction, n_{HS}, as a function of temperature for a 3D SCO system. The computational parameters are N = 125 (5x5x5), Δ/k_B = 1450 K, G/k_B = 470 K, J/k_B = -100 K, L/k_B = 750 K and ln(g) = 4.7.

For comparison purposes, we plotted the computed thermal behavior without edge effect on figure 3.17. The following conclusions can be drawn: (i) the hysteresis related to the middle-step disappears, (ii) the HS fraction increases from 0 (when L/k_B = 0 K) to 0.4 (when L/k_B = 750 K), (iii) the transition is shifted to lower temperatures, which means that the edge interaction seems to have an action opposite to a typical applied pressure because the edge interaction favors the HS state while an applied pressure is known to favor the LS state, due to its lower ionic volume.

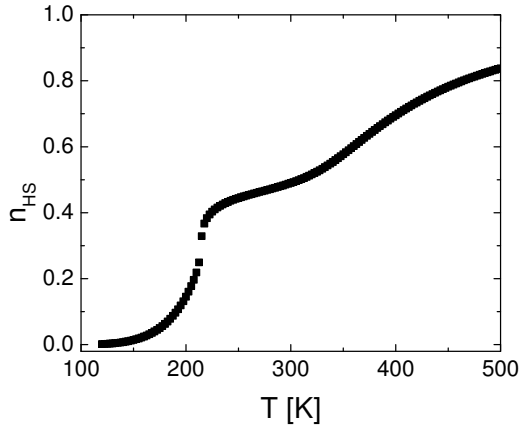

Figure 3.17 Simulated HS fraction, n_{HS}, as a function of temperature for a 3D SCO system when L/k_B = 0 K. The other parameters are the same as those of figure 3.16.

The computed thermal behavior of a 2D SCO system (where the interactions within molecules between planes are less than 10% of that between the molecules in the same plane) with 121 of metallic centers is shown in figure 3.18. Even if the number of metallic centers is almost equal to the number of metallic centers of the 3D system used above (125), the role of edge effect is reduced, because the number of edge metallic centers is only 40 compared to 98 metallic centers in the case of the 3D system. The spin transition is still incomplete, and proceeds in three steps but is no longer hysteretic.

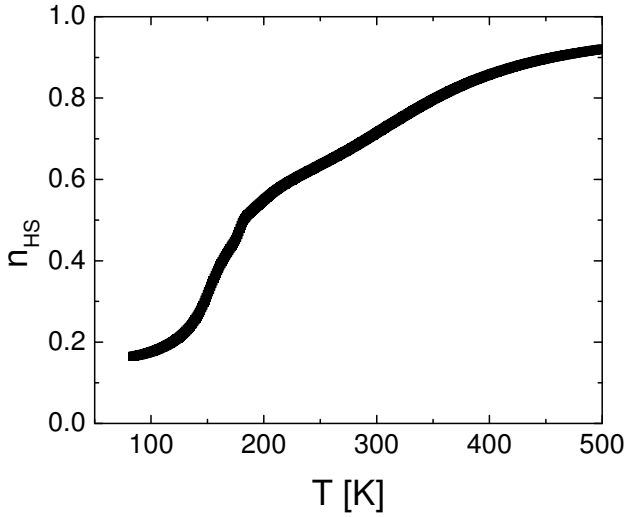

Figure 3.18 Simulated HS fraction, n_{HS}, as a function of temperature for a 2D SCO system with N = 121 (11x11). Other parameters are the same as those of figure 3.16.

Finally, we have investigated the increase of the system's size (figure 3.19). By increasing the system's size, i.e. by decreasing the ratio between edge and inner metallic centers (from 7 for a cube system with 64 metallic centers to 3.629 for a system with 125 metallic centers and to 2.375 for a system with 216 metallic centers), the edge effect decreases and the role of inner metallic centers increases. As a result, when we increase the size of the system, the equilibrium temperature, $T_{1/2}$, is shifted to higher temperatures and the transition proceeds continuously from the LS state to the HS state.

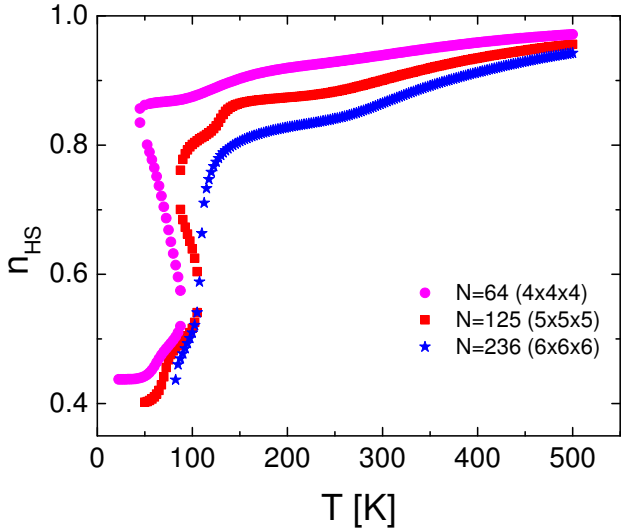

Figure 3.19 Simulated HS fraction, n_{HS}, as a function of temperature for 3D SCO systems of different sizes. Other parameters are the same as those of figure 3.16.

3.6. Size dependence of the equilibrium temperature in 2D SCO system

Figure 3.20 illustrates the thermal behavior of the HS fraction, $n_{HS}(T)$, calculated for various particle sizes. Upon decreasing the particle size ($N_x \times N_x$), the transition temperature is shifted downward and the width of the thermal hysteresis loop progressively increases as a result of surface effects. The detailed discussion of the results of the model follows. This behavior contrasts with the classical behavior of the thermal hysteresis with particle size, for which it monotonously vanishes at small sizes.

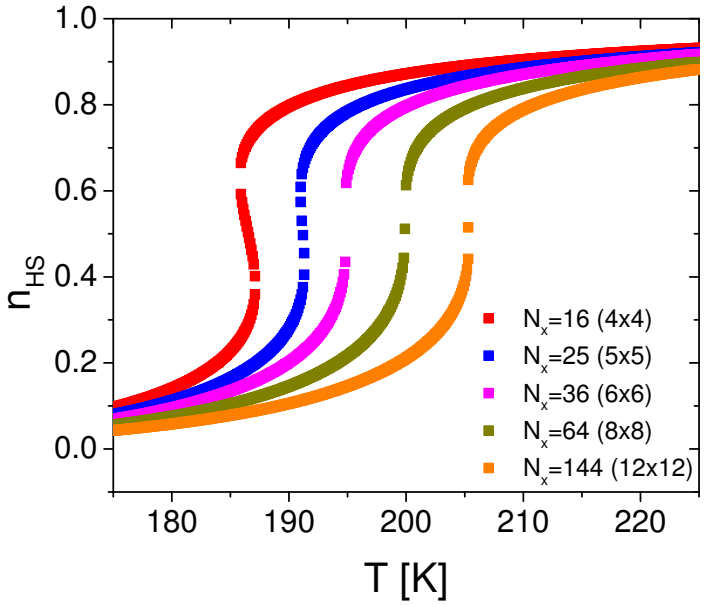

Figure 3.20 The simulated thermal behavior of the total HS fraction, $n_{HS}(T)$, for different system's sizes, showing an increase of the thermal hysteresis width for smaller nanoparticle sizes. The computational parameters are: Δ/k_B = 1300 K, G/k_B = 172.7 K, J/k_B = 15 K, L/k_B = 120 K, ln(g) = 6.01.

We could separate the contributions of surface atoms and core atoms in the thermal behavior of the total HS fraction of figure 3.20. Figure 3.21 displays two chosen cases of nanoparticles with sizes (4x4) and (12x12) depicting all contributions. One can clearly see, that in both cases, the surface (blue curves) starts to transform much earlier than the core (green curves), which clearly indicates that the surface is driving the thermal LS to HS transitions. It is however obvious that for very bigger sizes (unreachable with MCES method), the contribution of the surface will be marginal and the core will dominate. This tendency is already visible in the case of 12x12 particle, in which we remark that the curve of the total response (red) is much closer to that of the bulky atoms.

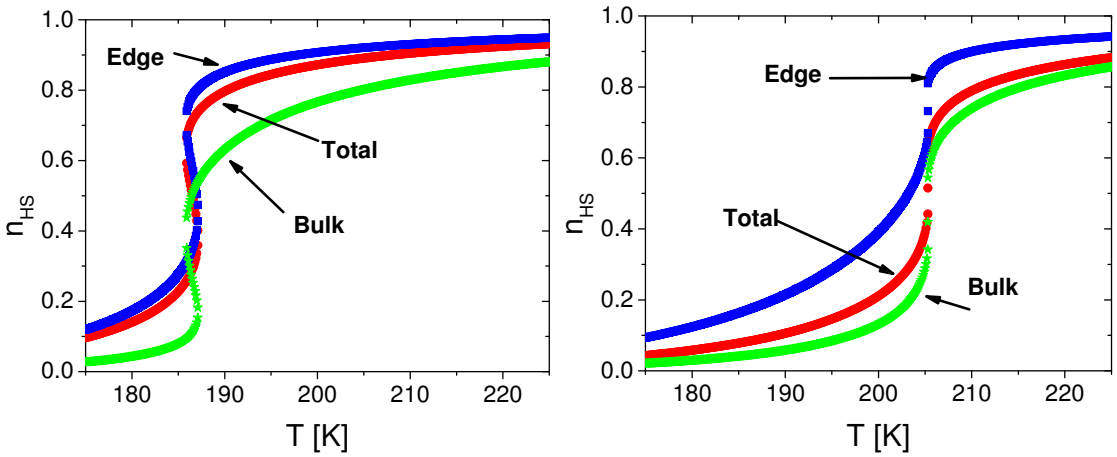

Figure 3.21 The thermal behavior for the edge, inner and total molecules of the system for the cases: left - N_t = 16 (4x4) and right - N_t = 144 (12x12). The model parameters are the same as those of Figure 2.20.

We found that the size dependence of the transition temperature could be described by analytical laws (easily extended to 3D models). Here, it worth mentioning that even for small sizes, exact analytical solutions of Hamiltonian (1) in 2D are out of reach [64], contrary to our previous studied case where the surface atoms were fixed in the HS state [57].

We introduce here a simple idea that the transition temperature of the system is still the result of a null total effective ligand-field. From the expressions of the ligand field for the edges and core atoms, as listed in Table 3.1, the transition temperature, T_{eq}, for a square lattice N_x x N_x is the solution of the following equation:

$$\frac{\Delta - k_B T_{eq} \ln g}{2} \times (N_x - 2)^2 + \frac{\Delta - 2L - k_B T_{eq} \ln g}{2} \times 4(N_x - 1) = 0 \qquad (3.10)$$

which expresses that the total ligand-field is equal to zero at $T=T_{eq}$.

	Total	Edges	Core
Number of atoms	N_x^2	$4(N_x\text{-}1)$	$(N_x\text{-}2)^2$
Ligand-field		$\frac{\Delta - 2L - k_B T \ln g}{2}$	$\frac{\Delta - k_B T \ln g}{2}$

Table 3.1. The ligand-field correlated to the molecules number.

Solving equation (3.10) gives the analytical expression of the lattice size-dependence of the transition temperature, as:

$$T_{eq} = \frac{N_c}{N_t} T_{eq}^{bulk} + \frac{N_s}{N_t} T_{eq}^{surf}, \qquad (3.11)$$

which for a 2D square system can be written as:

$$N_x^2 T_{eq} = (N_x - 2)^2 T_{eq}^{bulk} + 4(N_x - 1) T_{eq}^{surf}, \qquad (3.12)$$

leading to a parabolic and linear contribution of the bulk and surface contribution to $N_x^2 T_{eq}$ respectively. These tendencies have been checked numerically in the simulations, and as shown in figure 3.22, they are followed from a phenomenological point of view.

In equation 2.12, T_{eq}^{bulk} and T_{eq}^{surf} are the transition temperatures of the bulk and the surface, whose expressions are:

$$T_{eq}^{bulk} = \frac{\Delta}{k_B \ln g} \approx 216.3K \quad \text{and} \quad T_{eq}^{surf} = \frac{\Delta - 2L}{k_B \ln g} \approx 176.3K \tag{3.13}$$

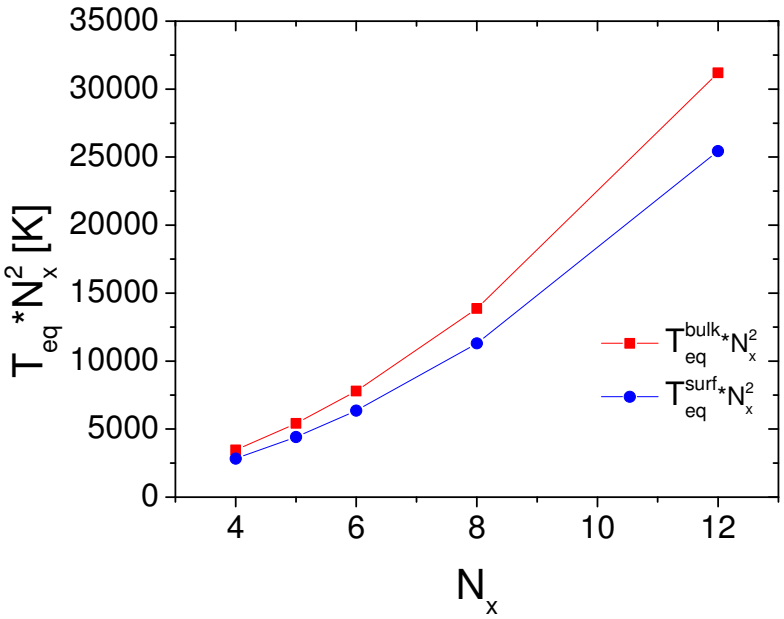

Figure 3.22 The size-dependence of $\boldsymbol{N_x^2 T_{eq}}$ showing a parabolic behavior for the bulk contribution and a quasi-linear trend for that of the surface, in qualitative good agreement with analytical predictions of equation (3.12).

Equation (3.11) predicts that the transition temperature has two limiting values, namely $T_{eq} = T_{eq}^{surf} = 176.3$ K for $N_x = 2$ for the smallest nanoparticle size, and $T_{eq} = \frac{\Delta}{k_B \ln g} \approx 216K$ corresponding to the bulk transition temperature, reached for an infinite lattice ($N_x \to \infty$).

The relevance of equation (3.11) is supported by the comparison to the exact results derived from the entropic sampling method. As shown in figure 3.23, where the global T_{eq} is plotted vs $1/N_x$, the analytical prediction (blue dots) given by equation (3.11) is in excellent agreement with the data obtained from the simulation (red squares).

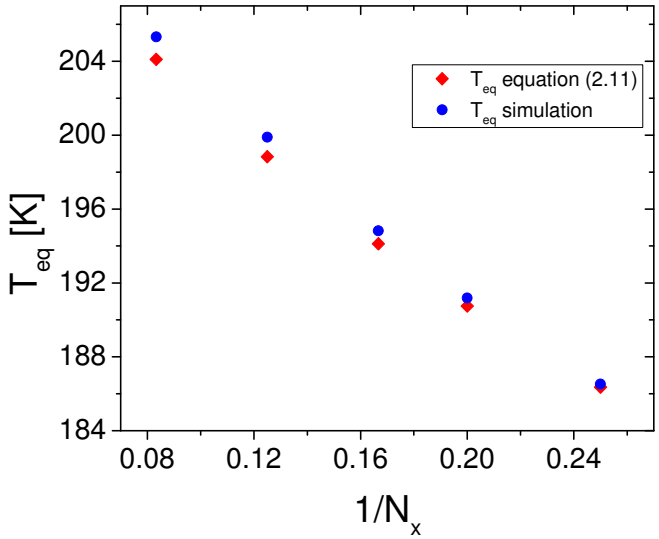

Figure 3.23 Size dependence of the global transition temperature showing an excellent agreement between MC simulations (blue circles) and analytical predictions (red squares) of equation (2.11). The computational parameters were: Δ/k_B = 1300 K, G/k_B = 172.7 K, J/k_B = 15 K, L/k_B = 120 K, ln(g) = 6.01

We should mention that the present model assumes that the effective degeneracy g is constant. Thus, g is considered to be independent on the strain at the surface and on the particle size.

For a thorough understanding of the size effects on the thermal behavior of the HS fraction, we performed MC simulations using the set of parameters given in figure 3.20, for which the studied system presents a gradual transition for the biggest studied size (i.e. $N_x = 12$). For that, the short-range interaction parameter was set to J/k_B = 15 K. It is worth mentioning that in the usual Ising-like model, the first-order phase transition takes place only when the condition $T_{O.D.} > T_{eq}$ is satisfied. Here, $T_{O.D.}$, is the order-disorder (or Curie) temperature of the corresponding pure Ising model, obtained from Hamiltonian (1) by putting Δ/k_B=0, L/k_B=0 and g=1 (ln(g)=0). For J=0 values, the interactions between SC sites are of pure long-range nature and so $T_{O.D} = G/k_B$ ~ 172.7 K (minimum value). For a large lattice size, the equilibrium temperature is dominated by the contribution of the bulk material and leads here to $T_{eq} \sim T_{eq}^{bulk} \sim 216$ K, which is larger than $T_{OD.}$ Under such conditions, for infinite lattice, the thermal behaviour of the HS fraction is that of a gradual conversion. When $J \neq 0$, the analytical expression of T_{OD} is out of reach. So, to determine T_{OD} for different lattice sizes, we performed MC simulations for Δ/k_B = 0 K, G/k_B = 172.7 K, J/k_B = 15 K, L/k_B = 0 K, ln(g) = 0. The results are summarized in figure 3.24, which shows a net increase of T_{OD} with the system's size, following a simple power law, $T_{OD} \sim \sqrt{N_x - 4}$, as demonstrated in figure 3.24(c).

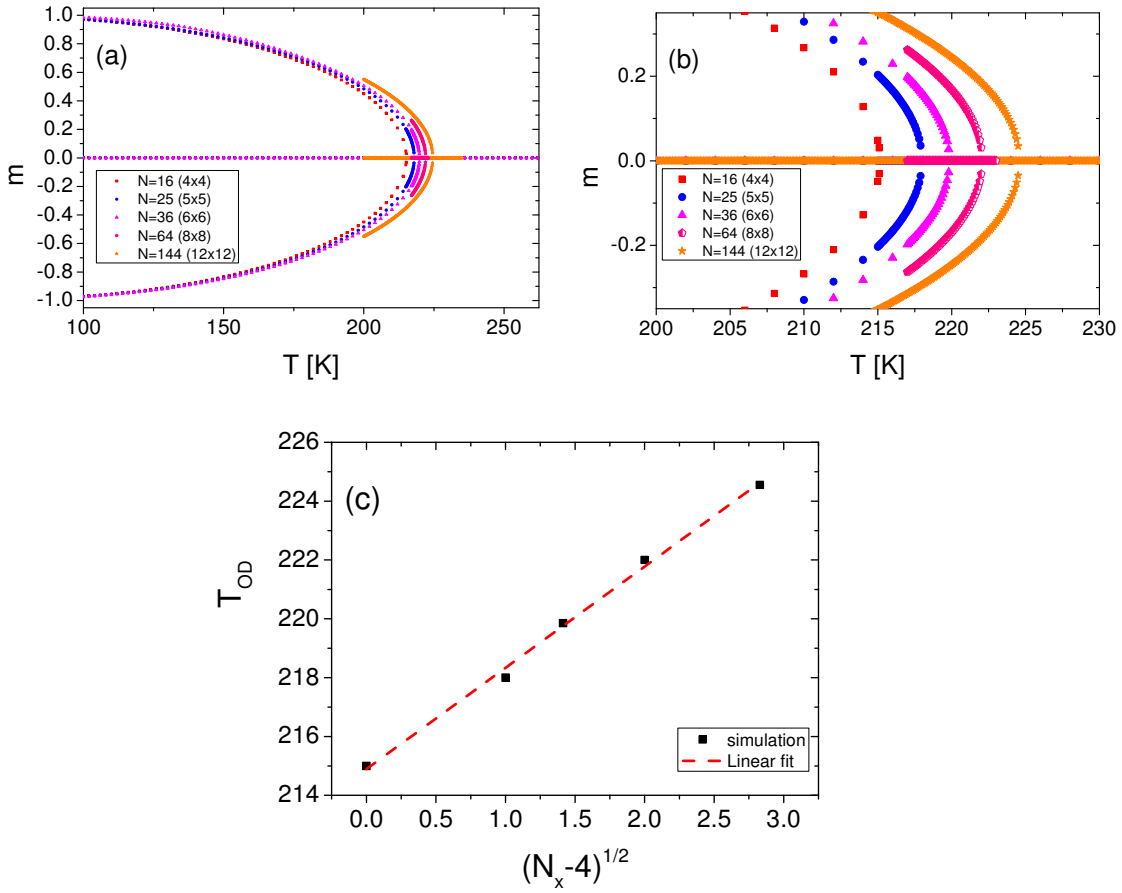

Figure 3.24 (a) The order-disorder temperature, $T_{O.D.}$, calculated for different system's sizes. (b) Zoom around the critical temperatures, showing the increase of $T_{O.D.}$ with size. (c) T_{OD} versus $\sqrt{N_x - 4}$ showing a linear behavior. The red dashed line is the best linear fit. The computational parameters are: Δ/k_B = 0 K, G/k_B = 172.7 K, J/k_B = 15 K, L/k_B = 0 K, ln(g) = 0.

The values of T_{OD} vary here from ~215 K for a 4x4 lattice to ~224 K for a 12x12 lattice. On the other hand, we found from figure 3.20, that T_{eq} ~204 K ($<T_{O.D}$=224K) for the lattice 12x12. Consequently, for the simple Ising-like model, the system is expected to show a first-order transition, while a gradual conversion is obtained in the simulations. However, for the lattice 4x4, we obtained a first-order transition with a hysteresis at T_{eq}~186K, which satisfies the usual criteria of occurrence of first-order transitions in Ising-like model. Figure 3.25 showing the behavior of the thermal hysteresis width versus the system sizes summarizes the results. The system undergoes a gradual SC transition for sizes bigger than $N_x = 6$, and shows first order transitions below this critical value. Interestingly, $N_x = 6$ corresponds to the value at which we observe only a slight difference between the number of particles in the bulk $(N_x - 2)^2$ and that at the surface, $4(N_x - 1)$. This fact demonstrates that the surface is playing the major role in driving the spin transition in this problem, as observed in experiments. The competition between the core and surface molecules are driven by the long-range, G, and the surface, L, interactions and then the critical size to obtain the first order transition is function of the rate of these interaction parameters.

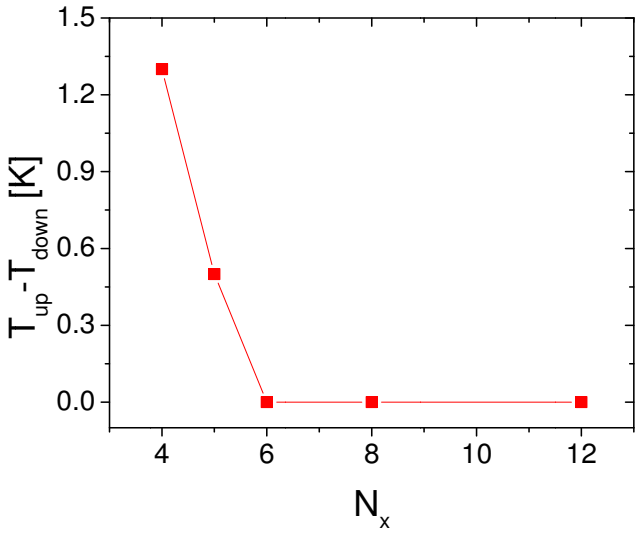

Figure 3.25 Size dependence of the thermal hysteresis width showing a drop of the bistability for nanoparticle bigger that 6x6. The model parameters are the same as those of figure 2.20.

3.7. Analysis of architecture effect

In the beginning of this subsection, the hysteretic properties of thermal induced LS ↔ HS phase transition of a 3D SCO nanostructure is analyzed when the cluster architecture is progressively changed from a cubic to a thin film. For this study the edge molecules was considered blocked in the HS state. The second part is dedicated to the study of architecture effect in a 2D SCO system when the edge molecules are considered as active molecules that interact with their local environment.

3.7.1. Results and discussions

The study of architecture effect for 1D and 2D SCO systems reported in [11] shows that the 1D system exhibits a gradual transition for a weak cooperativity system or a thermal transition for a strong value of short range interaction. For 1D ladder type systems the transition occurs with hysteresis and the hysteresis width increases more for a 2D square system (figure 3.26).

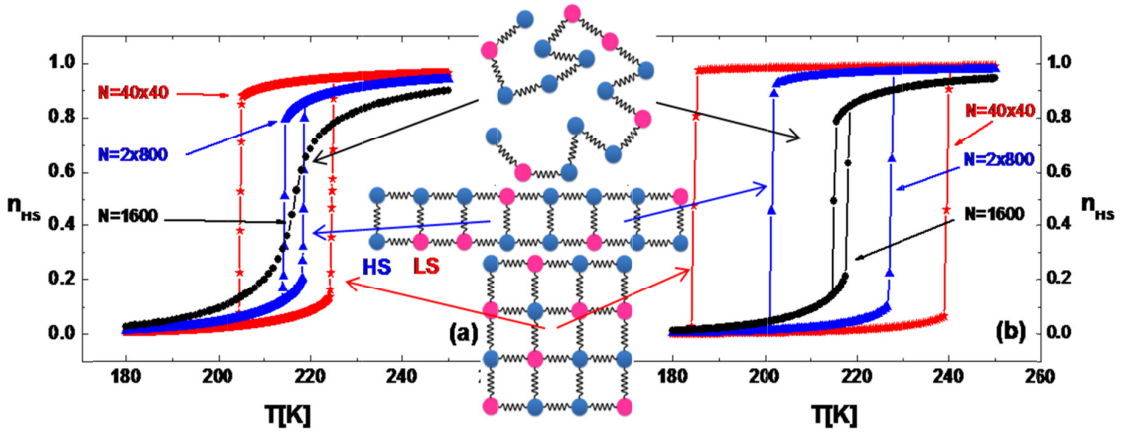

Figure 3.26 Evolution of HS fraction for different architectures of systems for the cases (a) J/k_B=64K and (b) J/k_B=105K. The computational parameters are: Δ/k_B = 1300K, $\ln(g)=6$, G/k_B = 105K [11].

For a 3D SCO system we observed an unexpected change of hysteretic behaviour, by a narrowing of the hysteresis loop upon decreasing size with a lowering of the equilibrium temperature and an increase of the residual high spin fraction that is undoubtedly a surface effect [65]. Indeed, when the system size is decreased, the edge/inner molecules ratio becomes more important which results in a strong influence of the coordination defects at the system surface, i. e. of the missing bonds at the surface [11]. The missing bonds on the edge molecules [66,67] could weaken the strength of the crystal field around the ionic centers that favors the HS state leading to a residual HS fraction. As it was presented by Volatron *et al.* [9], the first incomplete spin transition was obtained on a non-cubic architecture. In order to gain insight into the switching LS-HS mechanism of SCO systems when the system size is decreasing, we aim at analyzing the key parameters that can influence the behavior of these systems under thermal and pressure stimulation.

Up to now, there are few numerical studies of surface and architecture effects on the hysteretic behavior of nanostructured SCO system, since experimental work is also rather recent.

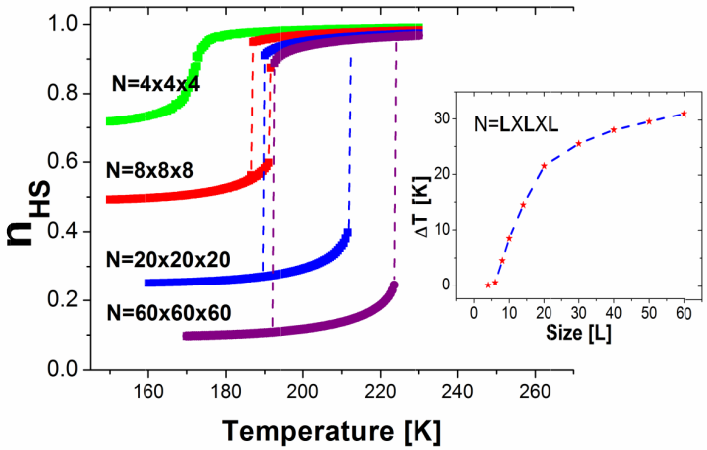

Figure 3.27 Simulated thermal transition for different sizes of a cubic system. The inset shows the size dependence of the thermal hysteresis loop width. The parameters' values used in the simulations are J/k_B = 45K, G/k_B = 105K, Δ/k_B = 1300K, ln(g) = 6.

Figure 3.27 shows a series of simulated thermal hysteresis loops obtained on a cubic system when its size is decreased from N=60x60x60 molecules to N=4x4x4 molecules. N represents the number of bulk SCO molecules (active molecules) and the edge molecules, on each face of the cubic system trapped in the HS state. Then the total number of molecules in the system is: M = (60+2)x(60+2)x(60+2) molecules.

As illustrated in the inset of figure 3.27, the hysteresis loop width (ΔT) decreases as the system's size is reduced, until a critical value (N_c) at which the hysteresis loop vanishes. This kind of behaviour has been also obtained by Boukheddaden *et al.* in a 2D system [57,66]. Another good agreement with 2D systems is represented by the evolution of residual high spin fraction. As can be observed in our simulations, by decreasing the system's size, the residual high spin fraction increases and an incomplete thermal spin transition can be observed. Furthermore, a shift of the equilibrium temperature: $T_{1/2}=(T_{down}-T_{up})/2$ to a lower temperature is observed when the system's size is decreased.

From figure 3.28 it can be observed that the hysteresis width of various SCO systems having the same number of molecules is strongly dependent on the cluster architecture. Thus, going from a cubic architecture to a thin film like architecture (discoid-shaped particles) the spin transition properties could be discussed as follows: i) an unexpected change in the

evolution of the high spin fraction and of the equilibrium temperature $T_{1/2}$; ii) a strong decrease of the hysteresis loop width from ΔT=31 K (for a cubic architecture: N=60x60x60 molecules) to ΔT=10 K (for a thin film like architecture: N=240x450x2 molecules). Thus, we can see that the change from a cubic architecture to a thin film architecture, results in a thermal spin transition behavior rather similar to that observed when the size effect was studied. In both cases the system's residual HS fraction increases and the equilibrium temperature is shifted to lower temperatures. This is a consequence of the enhancement of the surface effects, once the system's architecture or the system's size is changed. These results stress once again the important role played by the cluster architecture on the SCO system's cooperativity.

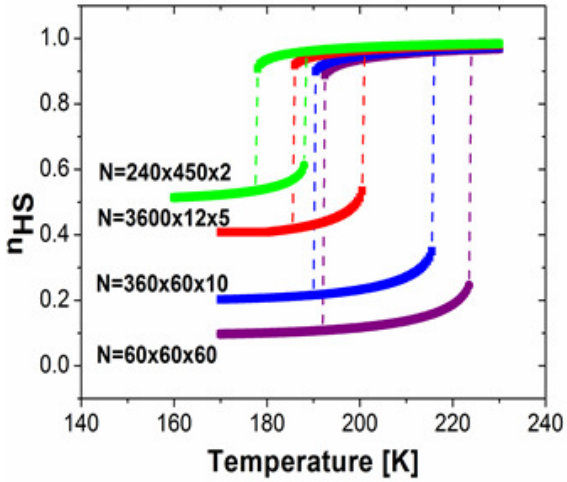

Figure 3.28 Simulated thermal hysteresis loops for different architectures of a 3D system, at ambient pressure. The parameters' values used in simulations are J/k_B = 45 K, G/k_B = 105 K, Δ/k_B = 1300K, ln(g) = 6.

In Table 3.2 a short summary of the main hysteretic characteristics obtained by varying the shape of the compounds (from cubic to thin film architecture) is presented.

Length (molecules)	Width (molecules)	Height (molecules)	ΔT (K)	n_{HS}	$T_{1/2}$ (K)
60	60	60	31	0.10	208
120	60	30	30	0.10	207.5
90	80	30	30	0.10	207.5
240	30	30	29	0.13	206.5
540	20	20	26	0.18	204
360	60	10	25	0.20	203
120	180	10	25.50	0.19	203
2160	10	10	18.50	0.32	197.75
360	120	5	19.50	0.31	197.75
240	180	5	19.50	0.31	197.75
540	80	5	19.50	0.32	197.25
1080	40	5	18.50	0.33	196.75
3600	12	5	14.50	0.40	193.25
240	450	2	10	0.51	183
5400	20	2	7.50	0.55	180.75

Table 3.2. Evolution of the hysteresis loop width, high spin fraction, and $T_{1/2}$ respectively as a function of the system's architecture of a 3D SCO system containing 216000 switchable molecules.

As previously mentioned, both short- and long-range interactions play an important role on the hysteretic properties of a SCO system. In figure 3.29, we depict some results on the short-range and long-range interaction parameters dependence of the hysteresis loop width for both cubic and thin film architectures.

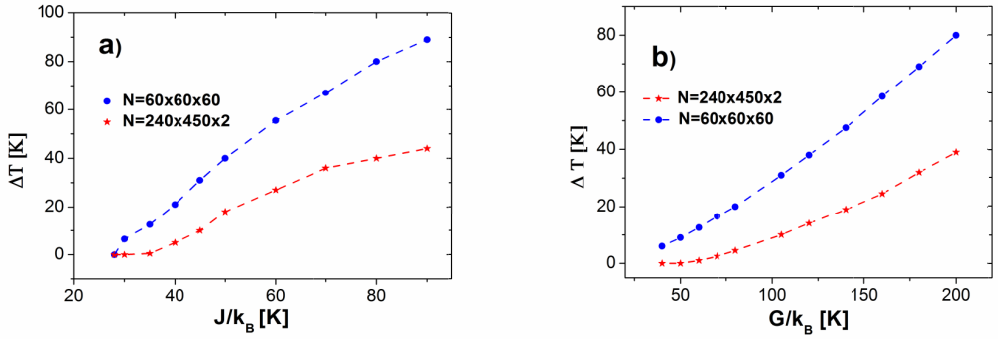

Figure 3.29 Variation of the hysteresis loop width (ΔT) vs. a) Short-range (J) interaction parameter, b) Long-range (G) interaction parameter for two system architectures: N=60x60x60 molecules (circles) and N=240x450x2 molecules (stars) respectively. The parameters' values used in simulations are Δ/k_B = 1300 K, ln(g) = 6 and ambient pressure.

The behavior of both systems (cubic and thin films) present an increase of the hysteresis loop width when the short-range interaction parameter is increased, but in the cubic case, this increase is more abrupt; the slope for the N=60x60x60 molecules system is higher than the slope of the N=240x450x2 molecules system. For small values of the short-range interaction parameter (J/k_B<35 K), the hysteresis loop width of the thin film architecture becomes zero, and the SCO system exhibits a gradual spin transition curve. It is worth noting that the critical value of the short-range interaction parameter J depends on the long-range interactions term, G: $J_c = \frac{T_{eq}}{6}\ln(T_{eq}k_B / G)$, where $T_{eq}=\Delta H/\Delta S$. These aspects were also highlighted in [11] when we studied the lattice effects in 2D systems.

It is important to mention that, even if the interaction parameters strength (J and G) are drastically modified, the hysteresis loop width for cubic and thin film systems can never have the same value ($\Delta T_{240x450x2} \neq \Delta T_{60x60x60}$).

Taking into account the above remarks, we can conclude that the organization of the molecules in SCO system plays an important role, being strongly affected by the system's architecture.

In figure 3.30 is reported the shape effect for a 2D system considering the edge molecules as active molecules that interact with their local environment. As we can see in figure 3.30 the behavior is strongly influenced by the edge effect. By decreasing the system's cooperativity the transition is shifted to lower temperatures and occurs with hysteresis contrary to the cases when the edge molecules are fixed in HS state.

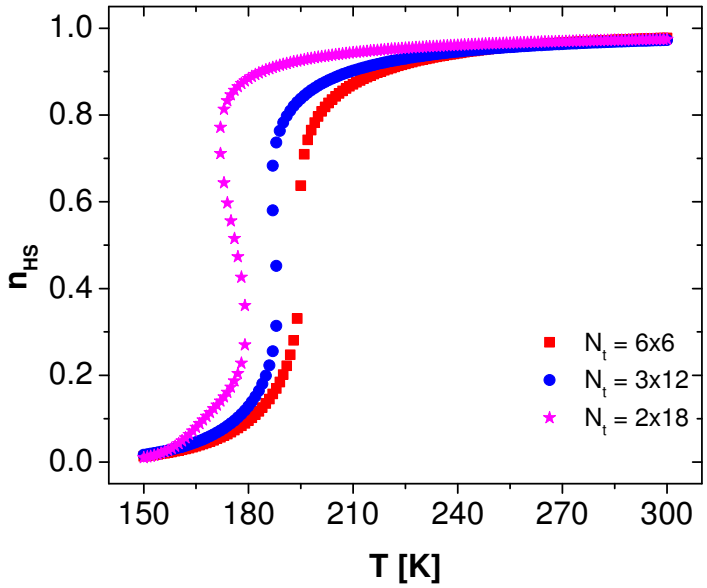

Figure 3.30 The thermal behaviour for different shapes of a 2D system containing 36 molecules. The computational parameters are: Δ/k_B = 1300 K, J/k_B = 15 K, G/k_B = 172.7 K, L/k_B = 120K, ln(g) = 6.01, N = 36.

3.7.2. Conclusions

This study demonstrates that the LS-HS transition triggered within an Ising-like model frame refined with a border SCO-matrix interactions, provides a qualitative insight on the physical origin of the cooperative phenomenon in 1D, 2D and 3D SCO systems embedded into a matrix. The main characteristic of this work is in the consideration of three types of interactions (short-range, long-range and SCO-matrix) which are responsible for the multi-step transitions. These strong cooperative effects which is shown to occur even in small-sized nanoparticles systems, confirm the results reported recently [9,11,15,57,59,68-70], that, depending on the compounds characteristics, hysteretic behavior is observed in such systems.

Among the principal effects of the interaction between the matrix and the edge (or surfaces) molecules, reported in this chapter, is the reduction of the energy gap between LS and HS states of surface atoms. In 2D SC nanoparticles, for some particular cases, it may deeply affect the thermal transition and lead to a qualitatively different thermal behavior than usually expected. We demonstrated that a specific weaker ligand field at the surface of SC nanoparticles may lead to the emergence of a thermal hysteresis (i.e., a bistability) at small sizes while it was absent for bigger sizes. This result reactivates the debate about the existence or not of a thermal bistability in finite sized SC nanoparticles. This point is of high importance for potential application of SC nanoparticles as rapid switching devices, since the existence of a bistability is necessary at this scale. One should however underline the important effect of the long-range interactions in the present study, which was considered as insensitive to the system size and which probably deserves a careful examination and developments in further works.

The role of architecture on the hysteretic properties of 2D and 3D SCO systems bordered by molecules blocked in the HS state, was also investigated. Thus, we have analyzed the changes induced in both thermal induced spin state switching properties from a cubic shape to thin film architecture. Our simulations are in good agreement with the experimental data already reported in the literature [9]. Moreover, we have shown that the cooperativity of a SCO system, not only depends on the interactions strength, but it is also strongly dependent

on the system's architecture. These differences in the architecture effect appear from the edge/inner molecules ratio and the missing bonds around ionic centers at the surface.

Further aspects related to the nanoparticle problem remain to be explored: the existence of a re-entrant first-order spin transition on decreasing the particle size will be analyzed using the same ideas developed through the manuscript.

3.8. References

[1] D. Chiruta, J. Linares, M. Dimian, Y. Garcia, European Journal of Inorganic Chemistry 2013 (2013) 951.

[2] C.-M. Jureschi, I. Rusu, E. Codjovi, J. Linares, Y. Garcia, A. Rotaru, Physica B: Condensed Matter 449 (2014) 47.

[3] C.M. Jureschi, J. Linares, A. Rotaru, M.H. Ritti, M. Parlier, M.M. Dîrtu, M. Wolff, Y. Garcia, Sensors (Basel, Switzerland) 15 (2015) 2388.

[4] S. Klokishner, J. Linares, F. Varret, Chemical Physics 255 (2000) 317.

[5] V. Mishra, R. Mukherjee, J. Linares, C. Balde, C. Desplanches, J.F. Letard, E. Collet, L. Toupet, M. Castro, F. Varret, Inorganic Chemistry 47 (2008) 7577.

[6] A. Rotaru, J. Linares, Journal of Optoelectronics and Advanced Materials 9 (2007) 2724.

[7] C. Lefter, R. Tan, J. Dugay, S. Tricard, G. Molnar, L. Salmon, J. Carrey, A. Rotaru, A. Bousseksou, Physical Chemistry Chemical Physics 17 (2015) 5151.

[8] C. Enachescu, H. Constant-Machado, E. Codjovi, J. Linares, K. Boukheddaden, F. Varret, Journal of Physics and Chemistry of Solids 62 (2001) 1409.

[9] F. Volatron, L. Catala, E. Riviere, A. Gloter, O. Stephan, T. Mallah, *Inorganic Chemistry* 47 (2008) 6584.

[10] L. Stoleriu, P. Chakraborty, A. Hauser, A. Stancu, C. Enachescu, Physical Review B 84 (2011) 134102.

[11] D. Chiruta, C.-M. Jureschi, J. Linares, Y. Garcia, A. Rotaru, Journal of Applied Physics 115 (2014).

[12] T. Yamada, K. Otsubo, R. Makiura, H. Kitagawa, Chemical Society Reviews 42 (2013) 6655.

[13] A. Rotaru, F. Varret, A. Gindulescu, J. Linares, A. Stancu, J. Letard, T. Forestier, C. Etrillard, Eur Phys J B 84 (2011) 439

[14] T. Forestier, A. Kaiba, S. Pechev, D. Denux, P. Guionneau, C. Etrillard, N. Daro, E. Freysz, J.F. Letard, Chemistry-a European Journal 15 (2009) 6122.

[15] A. Tokarev, L. Salmon, Y. Guari, G. Molnar, A. Bousseksou, New Journal of Chemistry 35 (2011) 2081.

[16] J. Pavlik, R. Boca, European Journal of Inorganic Chemistry (2013) 697.

[17] J. Tao, R.-J. Wei, R.-B. Huang, L.-S. Zheng, *Chemical Society Reviews* 41 (2012) 703.

[18] G. Molnar, T. Guillon, N.O. Moussa, L. Rechignat, T. Kitazawa, M. Nardone, A. Bousseksou, Chemical Physics Letters 423 (2006) 152.

[19] T. Kosone, I. Tomori, C. Kanadani, T. Saito, T. Mochida, T. Kitazawa, Dalton Transactions 39 (2010) 1719.

[20] K. Nishi, H. Kondo, T. Fujinami, N. Matsumoto, S. Iijima, M.A. Halcrow, Y. Sunatsuki, M. Kojima, European Journal of Inorganic Chemistry (2013) 927.

[21] R. Ohtani, M. Arai, A. Hori, M. Takata, S. Kitao, M. Seto, S. Kitagawa, M. Ohba, Journal of Inorganic and Organometallic Polymers and Materials 23 (2013) 104.

[22] D. Chiruta, J. Linares, Y. Garcia, P.R. Dahoo, M. Dimian, European Journal of Inorganic Chemistry 2013 (2013) 3601.

[23] C. Enachescu, L. Stoleriu, A. Stancu, A. Hauser, Journal of Applied Physics 109 (2011).
[24] P. Chakraborty, C. Enachescu, A. Hauser, European Journal of Inorganic Chemistry (2013) 770.
[25] C. Enachescu, M. Nishino, S. Miyashita, L. Stoleriu, A. Stancu, Physical Review B 86 (2012) 054114.
[26] J.A. Nasser, European Physical Journal B 21 (2001) 3.
[27] J.A. Nasser, K. Boukheddaden, J. Linares, European Physical Journal B 39 (2004) 219.
[28] J. Nasser, L. Chassagne, S. Topçu, J. Linares, Y. Alayli, The European Physical Journal B 87 (2014) 1.
[29] A. Gindulescu, A. Rotaru, J. Linares, M. Dimian, J. Nasser, Journal of Applied Physics 107 (2010) 09A959.
[30] A. Rotaru, J. Linares, S. Mordelet, A. Stancu, J. Nasser, *Journal of Applied Physics* 106 (2009) 043507.
[31] J. Linares, H. Spiering, F. Varret, European Physical Journal B 10 (1999) 271.
[32] K. Boukheddaden, J. Linares, E. Codjovi, F. Varret, V. Niel, J.A. Real, *Journal of Applied Physics* 93 (2003) 7103.
[33] I. Shteto, J. Linares, F. Varret, Physical Review E 56 (1997) 5128.
[34] C. Enachescu, R. Tanasa, A. Stancu, F. Varret, J. Linares, E. Codjovi, *Physical Review B* 72 (2005) 054413.
[35] F. Prins, M. Monrabal-Capilla, E.A. Osorio, E. Coronado, H.S.J. van der Zant, *Advanced Materials* 23 (2011) 1545.
[36] A. Rotaru, I.y.A. Gural'skiy, G. Molnar, L. Salmon, P. Demont, A. Bousseksou, Chemical Communications 48 (2012) 4163.
[37] A. Rotaru, J. Dugay, R.P. Tan, I.A. Gural'skiy, L. Salmon, P. Demont, J. Carrey, G. Molnar, M. Respaud, A. Bousseksou, Advanced Materials 25 (2013) 1745.
[38] G. Felix, K. Abdul-Kader, T. Mahfoud, I.y.A. Gural'skiy, W. Nicolazzi, L. Salmon, G. Molnar, A. Bousseksou, Journal of the American Chemical Society 133 (2011) 15342.
[39] A. Hauser, Spin Crossover in Transition Metal Compounds I, 2004, p. 49.
[40] J. Linares, E. Codjovi, Y. Garcia, Sensors 12 (2012) 4479.
[41] N.F. Sciortino, K.R. Scherl-Gruenwald, G. Chastanet, G.J. Halder, K.W. Chapman, J.-F. Letard, C.J. Kepert, Angewandte Chemie-International Edition 51 (2012) 10154.
[42] D. Chiruta, J. Linares, M. Dimian, Y. Alayli, Y. Garcia, European Journal of Inorganic Chemistry 2013 (2013) 5086.
[43] K. Boukheddaden, J. Linares, H. Spiering, F. Varret, European Physical Journal B 15 (2000) 317.
[44] M.M. Dîrtu, A. Rotaru, D. Gillard, J. Linares, E. Codjovi, B. Tinant, Y. Garcia, Inorganic Chemistry 48 (2009) 7838.
[45] M.M. Dîrtu, C. Neuhausen, A.D. Naik, A. Rotaru, L. Spinu, Y. Garcia, Inorganic Chemistry 49 (2010) 5723.
[46] C. Lochenie, W. Bauer, A.P. Railliet, S. Schlamp, Y. Garcia, B. Weber, Inorganic Chemistry 53 (2014) 11563.
[47] M.M. Dîrtu, F. Schmit, A.D. Naik, I. Rusu, A. Rotaru, S. Rackwitz, J.A. Wolny, V. Schunemann, L. Spinu, Y. Garcia, Chemistry 21 (2015) 5843.
[48] J.A. Real, H. Bolvin, A. Bousseksou, A. Dworkin, O. Kahn, F. Varret, J. Zarembowitch, Journal of the American Chemical Society 114 (1992) 4650.
[49] A. Bousseksou, J. Nasser, J. Linares, K. Boukheddaden, F. Varret, Journal De Physique I 2 (1992) 1381.
[50] J. Wajnflasz, R. Pick, J. Phys. Colloques 32 (1971) C1.
[51] P. Gütlich, A.B. Gaspar, Y. Garcia, Beilstein Journal of Organic Chemistry 9 (2013) 342.

[52] D. Chiruta, C.-M. Jureschi, J. Linares, P.R. Dahoo, Y. Garcia, A. Rotaru, The European Physical Journal B 88 (2015) 1.
[53] C.-M. Jureschi, B.-L. Pottier, J. Linares, P. Richard Dahoo, Y. Alayli, A. Rotaru, Physica B: Condensed Matter 486 (2016) 160.
[54] A. Bousseksou, G. Molnar, L. Salmon, W. Nicolazzi, *Chemical Society Reviews* 40 (2011) 3313.
[55] D. Chiruta, J. Linares, Y. Garcia, M. Dimian, P.R. Dahoo, Physica B: Condensed Matter 434 (2014) 134.
[56] A. Atitoaie, R. Tanasa, C. Enachescu, Journal of Magnetism and Magnetic Materials 324 (2012) 1596.
[57] A. Muraoka, K. Boukheddaden, J. Linares, F. Varret, Physical Review B 84 (2011).
[58] H.J. Shepherd, G. Molnar, W. Nicolazzi, L. Salmon, A. Bousseksou, European Journal of Inorganic Chemistry (2013) 653.
[59] E. Coronado, J.R. Galan-Mascaros, M. Monrabal-Capilla, J. Garcia-Martinez, P. Pardo-Ibanez, *Advanced Materials* 19 (2007) 1359.
[60] L. Catala, D. Brinzei, Y. Prado, A. Gloter, O. Stephan, G. Rogez, T. Mallah, Angewandte Chemie-International Edition 48 (2009) 183.
[61] Y. Raza, F. Volatron, S. Moldovan, O. Ersen, V. Huc, C. Martini, F. Brisset, A. Gloter, O. Stephan, A. Bousseksou, L. Catala, T. Mallah, Chemical Communications 47 (2011) 11501.
[62] Y. Prado, N. Dia, L. Lisnard, G. Rogez, F. Brisset, L. Catala, T. Mallah, Chemical Communications 48 (2012) 11455.
[63] S. Pillet, J. Hubsch, C. Lecomte, European Physical Journal B 38 (2004) 541.
[64] J. Linares, C.-M. Jureschi, A. Boulmaali, K. Boukheddaden, Physica B: Condensed Matter 486 (2016) 164.
[65] G. Felix, W. Nicolazzi, L. Salmon, G. Molnar, M. Perrier, G. Maurin, J. Larionova, J. Long, Y. Guari, A. Bousseksou, Physical Review Letters 110 (2013).
[66] H. Oubouchou, A. Slimani, K. Boukheddaden, Physical Review B 87 (2013).
[67] M. Quesada, F. Prins, E. Bill, H. Kooijman, P. Gamez, O. Roubeau, A.L. Spek, J.G. Haasnoot, J. Reedijk, Chemistry-a European Journal 14 (2008) 8486.
[68] D. Mader, S. Pillet, C. Carteret, M.-J. Stébé, J.-L. Blin, Journal of Dispersion Science and Technology 32 (2011) 1771.
[69] A. Tokarev, L. Salmon, Y. Guari, W. Nicolazzi, G. Molnar, A. Bousseksou, Chemical Communications 46 (2010) 8011.
[70] J. Larionova, L. Salmon, Y. Guarl, A. Tokarev, K. Molvinger, G. Molnar, A. Bousseksou, Angewandte Chemie-International Edition 47 (2008) 8236.

Chapter 4

Analysis of spin crossover nanochains using parabolic approximation in the framework of Atom-phonon coupling model

Contents

4 Analysis of spin crossover nanochains using parabolic approximation in the framework of Atom-phonon coupling model

4.1 Introduction

Considering atoms that are linked by springs characterized by three elastic constants as a function of the atom's state, Nasser *et al*. propose [1,2] the APC model to give a clear and enlarged view of the ST process in the SCO compounds. Although the APC model has only been applied to 1D and 2D systems thus far, different behaviors under various external stimuli, such as: temperature [2-4], pressure [5], light [6,7] have already been reported using APC.

From an experimental point of view, a substantial effort has been directed to the study of 1D (chain) Fe^{II} compounds [8,9] in various research groups. Bridging the gap between theory and experiment is expected to be achieved in the near future by researchers. Thus, correlations between calculations from the models and the observations of the synthetic chemists could be established soon. Physically, it is difficult to control all the parameters which govern the ST process, but it is expected that, understanding the mechanism of ST in molecular chains will be a big step forward in understanding two or three dimensional systems.

In this chapter the atom-phonon coupling model is used to explain and illustrate the behavior of a linear chain of molecules pertaining to SCO compounds. It is well known that apart from the system's cooperativity, which influences the hysteretic behavior of SCO complexes, the size of the system also plays a determinant role. The properties of the system are analyzed using a parabolic algorithm as a new method proposed in order to take into account the phonon contribution. Based on exact calculations, this method is closer to reality and more efficient than the mean-field approximation (MFA). In particular, both the parabolic algorithm and the dynamic-matrix method are tested and compared and the analysis of the system's behavior shows that large size systems can be treated without generating all the system states. We also analyzed the role of degeneracy, and the thermal variation of both the entropy and heat capacity in the ferromagnetic-like coupling case. These studies play an important role in the choice process of SCO compounds for the desired application. Thus, it is known that the compounds that exhibit transition with hysteresis have the main domain of application the memory devices. The compounds with a gradual transition, with a weak cooperativity, are destined to sensors devices. So, before to build a sensor it is important to know how to choose the compound according to the cooperativity and how will be influenced the behavior by interaction with other perturbation factors.

The originality of the APC model comes from the assumption that the neighboring molecules are connected by a spring whose elastic constant depends on the molecular states. Because the intra-molecular vibrations are not taken into account in the model, the SCO molecules are treated as atoms. Thus, the three elastic constants are defined as: $\lambda=C_{LL}$ when both the atoms are in the LS state, $\mu=C_{LH}$ when one atom is in a LS state and the other atom in a HS state, and $\nu=C_{HH}$ when both the atoms are in a HS state (figure 4.1). This makes the Hamiltonian of the system easy to cast.

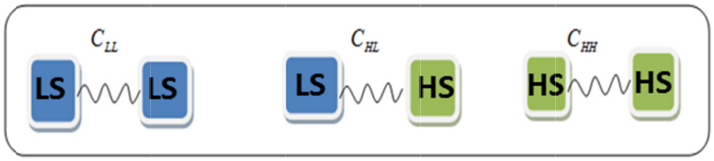

Figure 4.1 Schematic representation of the elastic constants related to the three molecular configurations.

Recently, a theoretical analysis of a two-step transition was performed using both the Ising-like model within the mean-field approximation (MFA) framework by Chiruta *et al*. [10] and the APC model by Nasser *et al*. by Gîndulescu *et al*. [2,4]. The former presented the two-steps behavior as a strong cooperative effect between antiferromagnetic-like short-range interactions and ferromagnetic long-range interactions while, the latter, explained it on the basis of phonon contributions, considering that the elastic constant value of an antiferromagnetic-like configuration, C_{LH} is closer to C_{HH}. Because the long-range interaction (G) in the Ising-like model is actually taking into account the phonon contribution of the APC model, a correspondence between the APC model and the Ising-like model can only be achieved when both the short (J) and long range (G) interactions are considered within the Ising-like model.

The Ising system chains, with contribution from both types of interactions, display a ST transition with different hysteresis loop widths which depend on the interactions (J and G) strength. Furthermore, Chiruta *et al*. [11] showed that, for 1D Ising case, there is a critical value (G_c) of long-range interactions at which the spin conversion curve transforms into a ST curve. The G_c is then a function of Δ (energy gap between the two spin states), short-range interactions (J) parameter, and degeneracy.

In our previous work we showed that: i) a 1D Ising system, with both interaction types, displays a ST transition with hysteresis for different temperature ranges, ii) in a 1D Ising system the two-steps transition is a consequence of the interplay between short and long-range interactions, iii) a two-steps transition can be reproduced with the APC model. In this work our main goal is to apply a new method to solve the APC Hamiltonian and to show that, with this approach, a phase transition with both interactions can be obtained, the same as in the 1D Ising model, and also to study large size systems.

The APC Hamiltonian solved with the dynamic matrix method gives the exact solution for the system. Within MFA, which has been used to solve the Hamiltonian for 1D and 2D systems, we illustrate, for the first time in this paper, how the corresponding Hamiltonian can be solved using the parabolic method. Recall that it is known that the MFA gives different results to those of the dynamic matrix method because the MFA replaces the three elastic constants with only one constant.

In this work we use the parabolic method to solve the Hamiltonian model considering three representative configurations: the "ferromagnetic" LS-LS and HS-HS and the antiferromagnetic LS-HS. We first study the differences between the dynamic-matrix method, the MFA, and this new approximation (the parabolic method). A second part of our work is devoted to the influence of the degeneracy in the parabolic method. Lastly, we study the entropy and the heat capacity starting from a small size (number of molecules N=8, 20) to a larger one (N=100 molecules) for different elastic interaction strengths between the molecules.

4.2 The model

In this section only some aspects of the APC model are considered and so we recall some of the equations which are the prerequisite to describe this work. More details about APC can be found in [2] as fully discussed by Nasser *et al*. To study the behavior of SCO systems in the framework of the APC model, we considered a circular chain of N atoms interconnected by a spring, with elastic constants as already described in the introduction; where $\lambda > \mu > \nu$. To present the electronic state of the atoms, we associate to each electronic state of the atoms a fictitious spin operator σ which has two eigenvalues +1 or -1 as a function of the atom state (HS or LS respectively).

In the framework of the APC model, the thermal variation of the n_{HS} (high spin fraction) is mediated by the competitions between the phonons which favor the HS state and the energy gap Δ, between the HS and the LS states, which favors the LS state. It is worth to note that in this contribution we consider the static spin configurations and we don't take into account the dynamic behavior as it has been done by Bonilla *et al*. [12] and Rikvold *et al*. [13,14].

The total Hamiltonian of the chain can be written as the sum of spin and phonon contributions as:

$$H = H_{spin} + H_{phonon} \tag{4.1}$$

From the definition of Δ which is the difference in energy between the two electronic levels (LS) and (HS), the spin Hamiltonian and phonon Hamiltonian can be expressed as:

$$H_{spin} = \sum \frac{\Delta}{2} \sigma_i \tag{4.2}$$

$$H_{phonon} = \sum g^{nhs} B(f_i) \tag{4.3}$$

where B (f_i) is the Boltzmann factor for each configuration(i).

Then, the Hamiltonian given by equation (4.1) can be solved in three different cases as shown below.

4.3 The methods

4.3.1 Dynamic Matrix method

For a number N of atoms we can generate all the possible configurations as sketched in figure 4.2. In this case we explore all the possibilities which are in good agreement with a real system.

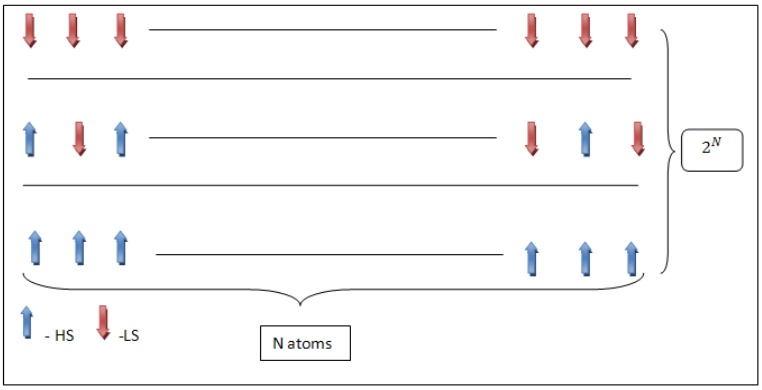

Figure 4.2 Schematic representation of the possible atoms' configurations in the chain.

Taking into account that, when one molecule is changing its state from LS to HS or vice versa, the whole chain is influenced, it is necessary to calculate for each configuration the Boltzmann factor as given by (equation (4.4)):

$$B(f_i) = \exp(-\beta E_i) \tag{4.4}$$

where: $\beta = \frac{1}{k_B T}$, E_i is the energy of state i; k_B is the Boltzmann's constant, and T is the temperature.

The dynamic matrix is determined from the equation of motion of the atoms (equation (4.5)) and the frequency ω_i of each molecule is given by the eigen values of the system formed by equation (4.5) and written as:

$$\begin{cases} m\ddot{u}_1 = C_{1,2}(u_2 - u_1) + C_{1,N}(u_N - u_1) \\ m\ddot{u}_2 = C_{2,3}(u_3 - u_2) + C_{1,2}(u_1 - u_2) \\ m\ddot{u}_i = C_{i,i+1}(u_{i+1} - u_i) + C_{i-1,i}(u_{i-1} - u_i) \end{cases} \tag{4.5}$$

where: $C_{i,i+1}$ represents the elastic constant between two neighbor molecules and which can be any of C_{LL}, C_{HL}, C_{HH}; u_i is the movement of one molecule from any consecutive state i, $i+1$.

Taking u_i and $\ddot{u}_i$:

$$u_i = A_i e^{-i\omega t} \tag{4.6}$$

$$\ddot{u}_i = -\omega^2 A_i e^{-i\omega t} \tag{4.7}$$

and after substitution in equation (4.5), with one of the elastic constants corresponding to the spin states of the atoms, the dynamic matrix is given by:

$$\begin{matrix} \frac{C_{1,2}}{C_{LL}} + \frac{C_{1,N}}{C_{LL}} & -\frac{C_{1,2}}{C_{LL}} & \cdots & \cdots & \cdots & -\frac{C_{1,N}}{C_{LL}} \\ -\frac{C_{1,2}}{C_{LL}} & \frac{C_{1,2}}{C_{LL}} + \frac{C_{2,3}}{C_{LL}} & -\frac{C_{2,3}}{C_{LL}} & \cdots & \cdots & \cdots \\ -\frac{C_{N,1}}{C_{LL}} & \cdots & \cdots & \cdots & -\frac{C_{N-1,N}}{C_{LL}} & \frac{C_{N-1,N}}{C_{LL}} + \frac{C_{N,1}}{C_{LL}} \end{matrix} \tag{4.8}$$

Then one finds the expressions of λ_i and ω_i, the eigenvalues and corresponding frequencies of this dynamic matrix, as expressed in (equations (4.9) and (4.10)):

$$\lambda_i = \frac{\omega_i^2 m}{C_{LL}} \tag{4.9}$$

$$\omega_i = \sqrt{\frac{C_{LL}}{m}}\sqrt{\lambda_i} \tag{4.10}$$

The vibrational frequencies of the molecules are obtained by calculating the eigen values of the system, which depend only on the elastic constant and on the mass m of the atom and can be rewritten (equation (4.12)) in terms of ω_{max} defined by equation (4.11) as:

$$\omega_{max} = 2\sqrt{\frac{C_{LL}}{m}} \tag{4.11}$$

$$\omega_i = \frac{\omega_{max}}{2}\sqrt{\lambda_i} \tag{4.12}$$

The partition function is given by:

$$Z^k = g^{n_{HS_i}}\, e^{-\frac{\beta\Delta}{2}m_i} \prod_{i=1,N} \frac{1}{2\sinh\left(\frac{\hbar\omega_i}{2k_BT}\right)} \tag{4.13}$$

Constructing the dynamic matrix from all the states distribution as sketched in figure 4.2, will result in some configurations which will have the same value of the partition function (Z). To override this aspect we define a parameter *"nbre(n_{HS})"* which is the sum of the configuration with the same "n_{HS}" value and with the same eigen values (frequency). Since we take only the phonon contribution we must divide each partition function corresponding to each configuration by Z_{ph}^1. Z_{ph}^1 is the partition function when the all the molecules in the chain are in the LS state.

$$Z_{ph} = \sum_{k=1,N} \{nbre(n_{HS})Z^k / Z^1\} \tag{4.14}$$

4.3.2 The Parabolic algorithm

Understanding the mechanisms underlying the behavior of complex systems is a priority in various fields whether pertaining to fundamental or applied research. During the last years a significant interest in research has thus been directed to the development of models and methods which can simulate the behavior of different kinds of such complex systems. In the physics of the bistable systems, only few methods exists that allows to solve exactly finite or infinite systems, but fortunately enough, in the case of finite systems, numerical methods can be developed to achieve exact or approximate solutions.

In this respect, we propose a new method, or algorithm, based on a parabolic equation to determine a distribution over the system's states, or energies. This equation is expressed as:

$$f(x) = ax^2 + bx \tag{4.15}$$

For a configuration with an elastic constant between the atoms equal to *K,* the partition function is given by:

$$\prod(K) = \prod_{\alpha=\pm1,\pm2,\ldots,\pm\left(\frac{N}{2}-1\right),\frac{N}{2}} \frac{1}{2\sinh\left(\frac{1}{2t}\sqrt{\frac{K}{\lambda}}\sin\left|\alpha\frac{\pi}{N}\right|\right)} \tag{4.16}$$

where *t* is a reduced parameter expressed as:

$$t = \frac{k_BT}{\hbar w_{\max}(\lambda)} \tag{4.17}$$

In the framework of this parabolic approximation we consider three different situations, namely:

i) when all the molecules are in a LS state, that is with a chain with the following atomic configuration (LS-LS-LS…LS-LS-LS), and with the partition function given by :

$$\prod(\lambda)=\prod_{\alpha=\pm1,\pm2,\ldots,\pm\left(\frac{N}{2}-1\right),\frac{N}{2}}\frac{1}{2\sinh\left(\frac{1}{2t}\sin\left|\alpha\frac{\pi}{N}\right|\right)} \tag{4.18}$$

ii) when all the molecules are connected by a spring ν corresponding to the system's chain with the atomic configuration (HS-HS-HS….HS-HS-HS), and with the partition function given by:

$$\prod(\nu)=\prod_{\alpha=\pm1,\pm2,\ldots,\pm\left(\frac{N}{2}-1\right),\frac{N}{2}}\frac{1}{2\sinh\left(\frac{1}{2t}\sqrt{\frac{\nu}{\lambda}}\sin\left|\alpha\frac{\pi}{N}\right|\right)} \tag{4.19}$$

iii) and finally, the third case, when the chain is a mixture of molecules in LS or HS states for which $K=\mu$, and with the partition function given by:

$$\prod(\mu)=\prod_{\alpha=\pm1,\pm2,\ldots,\pm\left(\frac{N}{2}-1\right),\frac{N}{2}}\frac{1}{2\sinh\left(\frac{1}{2t}\sqrt{\frac{\mu}{\lambda}}\sin\left|\alpha\frac{\pi}{N}\right|\right)} \tag{4.20}$$

We first define a partition function parameter R_{ph} connected only to the phonon contribution. Depending on the molecules' spin state, we define the following parameters:

a) $R_{ph}(\mu)=\frac{\Pi(\mu)}{\Pi(\lambda)}$ when the chain is a mixture of molecules in HS and LS states (HS-LS-HS…LS-HS-LS) with $n_{HS}=N/2$;

b) $R_{ph}(\nu)=\frac{\Pi(\nu)}{\Pi(\lambda)}$ when the chain consists only of molecules in HS state (HS-HS-HS….HS-HS-HS) with $n_{HS}=N$;

In the framework of the "parabolic approximation" the phonon contribution to the partition function R_{ph}, as previously defined, can be written in the parabolic form as follows:

$$\ln\left(R_{ph}\right)=an_{HS}^2+bn_{HS} \tag{4.21}$$

Replacing the partition functions $R_{ph}(\nu)$ and $R_{ph}(\mu)$ in equation (4.21) we obtain a system which takes the following form:

$$\begin{cases}\ln\left(R_{ph}(\mu)\right)=a\ (N/2)^2+b\ (N/2)\\ \ln\left(R_{ph}(\nu)\right)=a\ N^2+b\ N\end{cases} \tag{4.22}$$

from which a and b can be solved as:

$$\begin{cases}a=\dfrac{2\ln\left(R_{ph}(\nu)\right)-4\ \ln\left(R_{ph}(\mu)\right)}{N^2}\\ b=\dfrac{4\ \ln\left(R_{ph}(\mu)\right)-\ln\left(R_{ph}(\nu)\right)}{N}\end{cases} \tag{4.23}$$

From the partition function of equation (4.21) corresponding to different chain's states, the total partition function of the system can then be calculated as:

$$Z_{ph}\left(parabolic\right)=\sum_{nhs}\left\{ g^{nhs}e^{-\frac{\delta}{2t}\left(2\,nhs-N\right)} \quad e^{\ln R_{ph}} \quad e^{\ln\frac{N!}{(N-nhs)!\;nhs!}}\right\} \tag{4.24}$$

where δ is another reduced parameter expressed as:

$$\delta=\frac{\Delta}{\hbar\omega_{\max}\left(\lambda\right)} \tag{4.25}$$

4.3.3 Mean field approximation

It is already known [2,4] that MFA can be applied to solve the APC Hamiltonian. The effective uniform field, *h*, and the effective exchange-like interaction *J*, are used to express the variation of the Hamiltonian H_0 [4]:

$$H_0=H_{0s}\left(h,J\right)+H_{0ph}\left(K\right) \tag{4.26}$$

where

$$H_{0s}=\sum_{i=1}^{N}-h\hat{\sigma}_i+\sum_{i=1}^{N}-J\,\hat{\sigma}_i\hat{\sigma}_{i+1} \tag{4.27}$$

And where the phonon contribution to the Hamiltonian is given by:

$$H_{0ph}\left(K\right)=\sum_{i=1}^{N}\frac{p_i^2}{2m}+\sum_{i=1}^{N}\frac{K}{2}q_i^2 \tag{4.28}$$

Under the assumption that the elastic constant *K* is the same for all atoms. For a configuration given by the fictitious magnetization $m=\langle\sigma_i\rangle$ and spin correlations $s=\langle\sigma_i\,\sigma_j\rangle$, the effective elastic constant *K* determined by this technique is given by [4]:

$$K=\frac{\lambda+2\mu+\nu}{4}+\frac{\nu-\lambda}{2}m+\frac{\lambda-2\mu+\nu}{4}s \tag{4.29}$$

and the phonon part of the Hamiltonian can then be written as:

$$H_{phonon}\left(K\right)=\frac{\hbar w_{max}\left(\lambda\right)}{2}\sqrt{\frac{K}{\lambda}}\;\sum_{\alpha}sin\left|\alpha\frac{\pi}{N}\right|\coth\left(\frac{\hbar w_{max}\left(\lambda\right)}{2}\sqrt{\frac{K}{\lambda}}\;sin\left|\alpha\frac{\pi}{N}\right|\right) \tag{4.30}$$

Thus, the fictitious magnetization, m, and the fictitious spin correlation, s, are given by the following equations, as it has been proposed in Ref [2]:

$$m=\frac{e^{\beta J}\sinh\left[\beta\left(h+kT\frac{\ln g}{2}\right)\right]}{\sqrt{B}} \tag{4.31}$$

$$s=1-\frac{2e^{-2\beta J}}{A\sqrt{B}} \tag{4.32}$$

The parameters A, B, h, J can then be expressed as follows:

$$A=e^{\beta J}\cosh e^{\beta J}\sinh\left[\beta\left(h+kT\frac{\ln g}{2}\right)\right]; \tag{4.33}$$

$$B=e^{\beta J}\,\sin h^2\left[\beta\left(h+kT\frac{lng}{2}\right)\right]+e^{-2\beta J}; \tag{4.34}$$

$$h = -\frac{\Delta}{2} - \frac{\nu - \lambda}{4K}\frac{H_{phonon}[K]}{N}; \tag{4.35}$$

$$J = -\frac{\lambda - 2\mu + \nu}{8K}\frac{H_{phonon}[K]}{N} \tag{4.36}$$

where the elastic constants depend on the spin state of the atoms in the chain as given explicitly in equations (4.35) and (4.36) for the effective uniform field, *h*, and for the effective exchange-like interaction, *J*, respectively.

4.4 Results and discussions

Solving the system's Hamiltonian (equation (4.1)) by using either of the above three mentioned methods, allows the determination of the HS fraction n_{HS} as function of temperature.

Figure 4.3a and figure 4.3b show numerical results concerning the evolution of HS fraction. Before presenting in details the next figure, we recall that the Ising like models lead to phase transitions when the balance between short-range and long-range interactions allow cooperative effects.

In the APC model the x and y reduced parameters are introduced as follows:

$$x = \frac{\nu}{\lambda} \tag{4.37}$$

$$\mu = \frac{\lambda + \nu}{2} + \frac{\lambda - \nu}{2} y \tag{4.38}$$

The parameter y is related to the short-range interaction: y=0 corresponds to the absence of short range interaction. y>0 and y<0 are related to the "ferromagnetic-like" and "anti-ferromagnetic-like" coupling respectively.

Figures 4.3a and 4.3b display the evolution of HS fraction given by the three methods for a chain of N=8 molecules (figure 4.3a) or N=20 molecules (figure 4.3b) with the calculated values plotted as circles, triangles and stars. The circles correspond to the date obtained within the MFA method; the triangles within the parabolic method and the stars within the dynamic matrix method.

For regular interactions strength corresponding to x=0.2 and y=0.2, the variation displayed in figures 4.3a and 4.3b shows that the parabolic method gives the same results as the dynamic matrix method, that is a gradual transition. In the frame-work of the MFA method, the system displays a hysteretic behaviour with a hysteresis width equal to 0.15 for N=8 molecules and 0.2 for N=20 molecules. Furthermore, the critical temperature $T_{1/2}$, which corresponds to n_{HS}=0.5, is shifted to higher temperatures when the system's size is increased. Here it is worth noting that the MFA method gives a hysteretic behavior because it generates artificially infinite long-range interactions.

Motivated by the good agreement between the parabolic method and the dynamic matrix method, the former method has been applied to different cases as described in the next section. The purpose is to find out if the parabolic method always gives the same results as the exact method or if it is influenced by other parameters so as to determine its range of application.

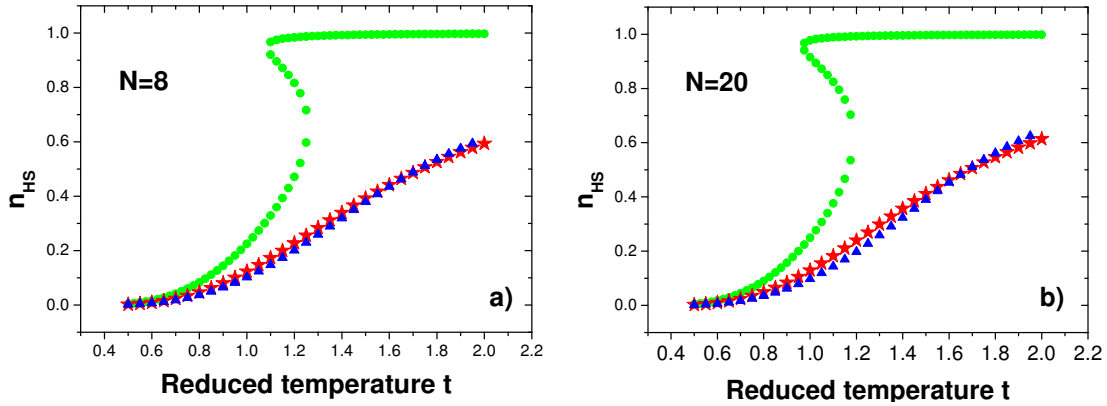

Figure 4.3 The thermal variation of high spin fraction n_{HS} for a 1D SCO compound a) N=8 molecules b) N=20 molecules using the MFA method (circles), the Parabolic method (triangles), the Dynamic matrix (stars). Other parameter are x=0.2, y=0.2, g=5 and δ=4.

4.4.1 Role of parameters in the parabolic algorithm

In this section the main goal is to develop a method to study large systems (high number of molecules) through the parabolic algorithm without having to generate all the state distribution as with the dynamic matrix method. To validate our new method we first study in this section the key factors which influence the curves calculated with the parabolic algorithm by considering only short range interactions on the one hand and then both short and long range interactions on the other.

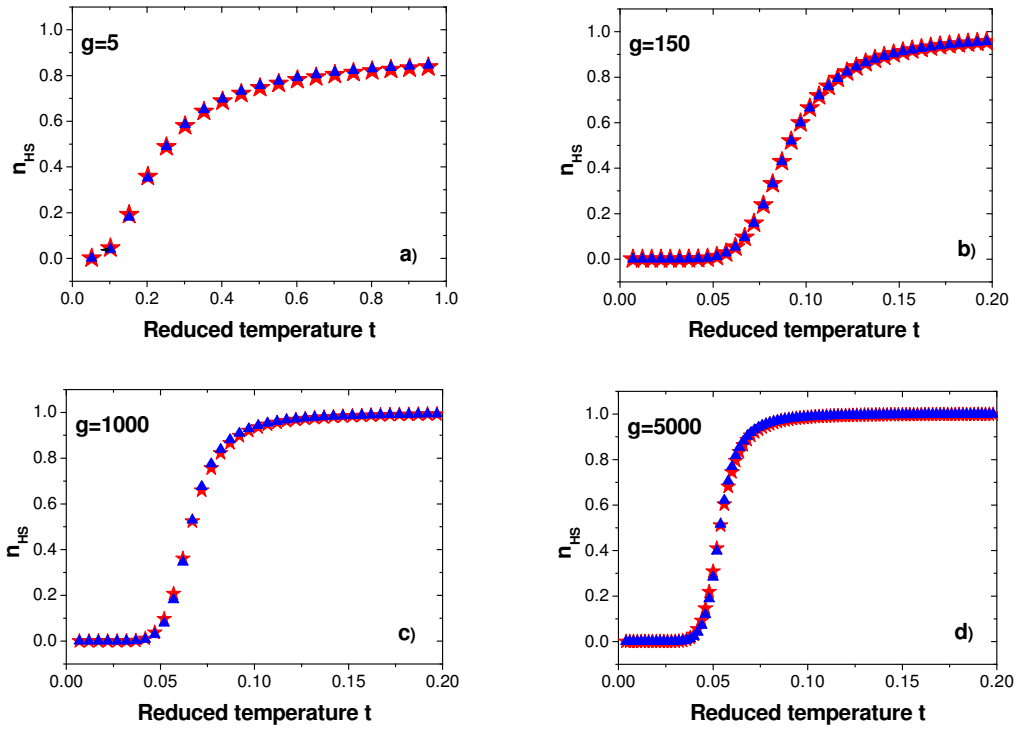

Figure 4.4 The thermal variation of the high spin fraction n_{HS} for a 1D SCO compound (N=8 molecules) for different degeneracies a) g=5 b) g=150 c) g=1000 d) g=5000 using, the Parabolic method (triangles), the Dynamic matrix (stars). Other parameter are x=0.3, y=0, and δ=0.6.

It is known that in SCO compounds, two main typical behaviors can be distinguished in relation to the phenomenological transformations between the LS and HS states: the cooperative case in which the ST transformation occurs abruptly within a limited temperature range of some Kelvin and the other type, non-cooperative case, usually called gradual case, in which the ST takes place gradually over an ample temperature range, typically greater than 50K. To elucidate the factors which contribute to the system's behavior, all the studies carried over the years illustrated different aspects. Thus, besides the influence of the interactions in the system, an important role is played by the variation of the molar entropy ΔS. Taking into account that g= ΔS/R, with R the universal Gas Constant, the thermal evolution of the high spin fraction for different values of degeneracy (g) is displayed in figures 4.4 and 4.5.

The thermal dependence of the HS fraction obtained using both methods: the dynamic matrix and the parabolic method, for various values of the degeneracy is reported in figure 4.4. The presence of short-range interactions has an important contribution on the system's behavior and leads to a gradual spin conversion. The results obtained within both methods are in excellent agreement as shown in figures 4.4.

The system's behavior when both the short-range interactions and long-range interactions are taken into account is shown in figure 4.5 in the limiting case, when the system presents strong interactions (x=0.1, y=0.9).

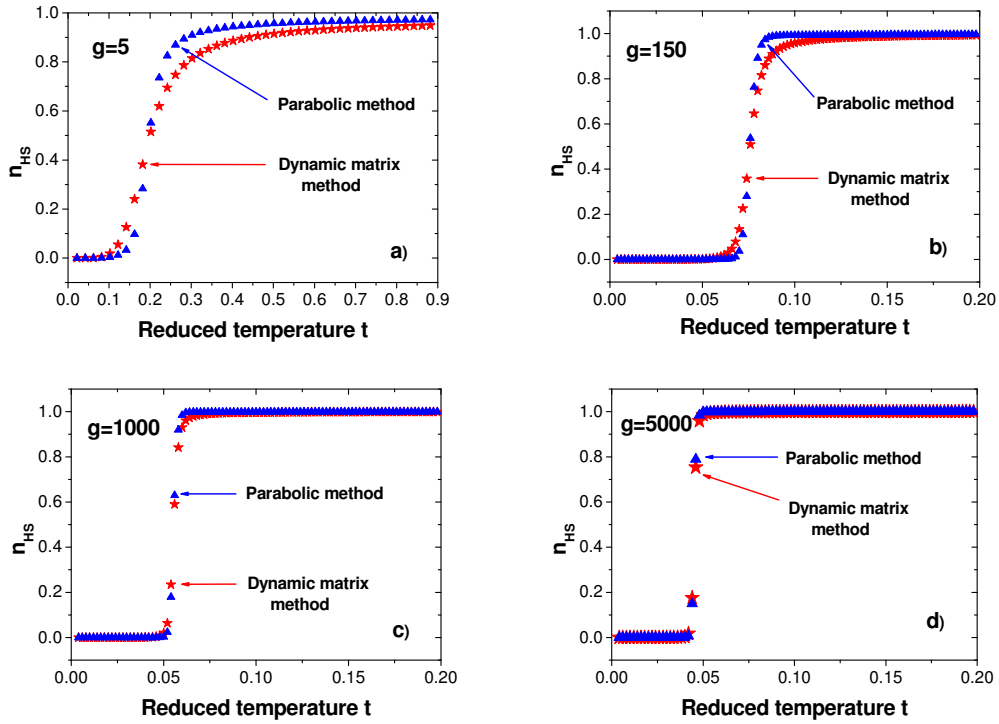

Figure 4.5 The thermal variation of n_{HS} for a 1D SCO compound (N=8 molecules) for different degeneracy values a) g=5 b) g=150 c) g=1000 d) g=5000 using the Parabolic method (triangle curve), the Dynamic matrix (stars curve). The following computational parameters have been used: x=0.1, y=0.9, and δ=0.6.

The following characteristics can be depicted from figures 4.5a) to 4.5d): (i) when the interactions between the molecules (denoted here by x and y) are increased the gradual transition moves to an abrupt one, (ii) at low and high temperatures the values given by both methods are the same, and (iii) for small degeneracies, a difference is noted in the results given by the two methods when the system is characterized by strong interactions between the molecules. Comparing results reported in figure 4.4 and figure 4.5, it can be observed that, for small values of the degeneracy different results have been obtained when both short and long-

range interactions are taken into account. When the degeneracy is increased, as can be seen in figures 4.5c and 4.5d, for g=1000 and g=5000, the curves obtained using the two methods are similar. Thus within the APC model, the choice of the degeneracy parameter is an important point underlining the importance of the phonon contribution. Indeed, it is known that the degeneracy factor takes into account both electronic and vibrational contributions. Note that by increasing the degeneracy value the equilibrium temperature $T_{1/2}$ is decreasing.

4.4.2 Entropy variation and heat capacity using the dynamic matrix method vs. the parabolic method

Following the results given in the previous section showing the good agreement between the exact method (dynamic matrix) and the parabolic method, at high degeneracies, the thermal dependence of the entropy and heat capacity for different interactions and sizes were calculated under these conditions. The system entropy could be calculated as the first derivative of the Gibbs free energy with respect with the temperature $S = -dF/dt$.

Computations were carried for two chains' lengths (N= 8 molecules and N = 20 molecules) and for two cases: when short-range interactions are absent in the systems (y=0) and when the SCO system is characterized by the presence of strong short-range interactions.

Both the parabolic method and the dynamic matrix method lead to the same curves and the same evolution between the LS and HS states as shown in figure 4.6. One may also note the gradual entropy variation in figure 4.6b and figure 4.6d as a consequence of weak or the absence of cooperativity effects in the system. This aspect is expected because short-range interactions being equal to 0, the system is influenced only by long-range interactions.

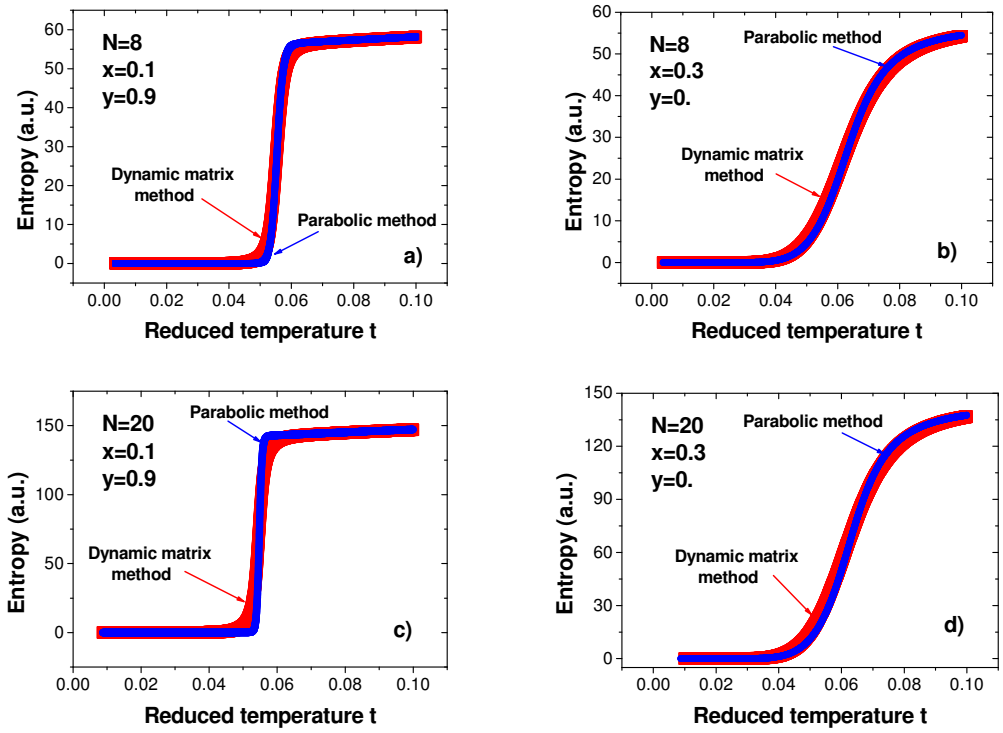

Figure 4.6 Time dependence of the entropy per atom obtained using: the dynamic matrix method (red curve) and the parabolic method (blue curve) for two different sizes and interactions. Other parameter are g=1000 and δ=0.6.

Figure 4.7 display the evolution of the heat capacity as calculated from the relationship, $C = dS/dt$ for a chain which contains 8 molecules (figures 4.7a and 4.7b) and 20 molecules

(figures 4.7c and 4.7d). The two methods, this time show a difference in the evolution of heat capacity in all cases. The heat capacity curves obtained with the exact method have a lower maximum compared with those obtained using the parabolic method because the total free energy of the system for a given temperature obtained using the exact method is less than the total free energy of the system given by the parabolic method.

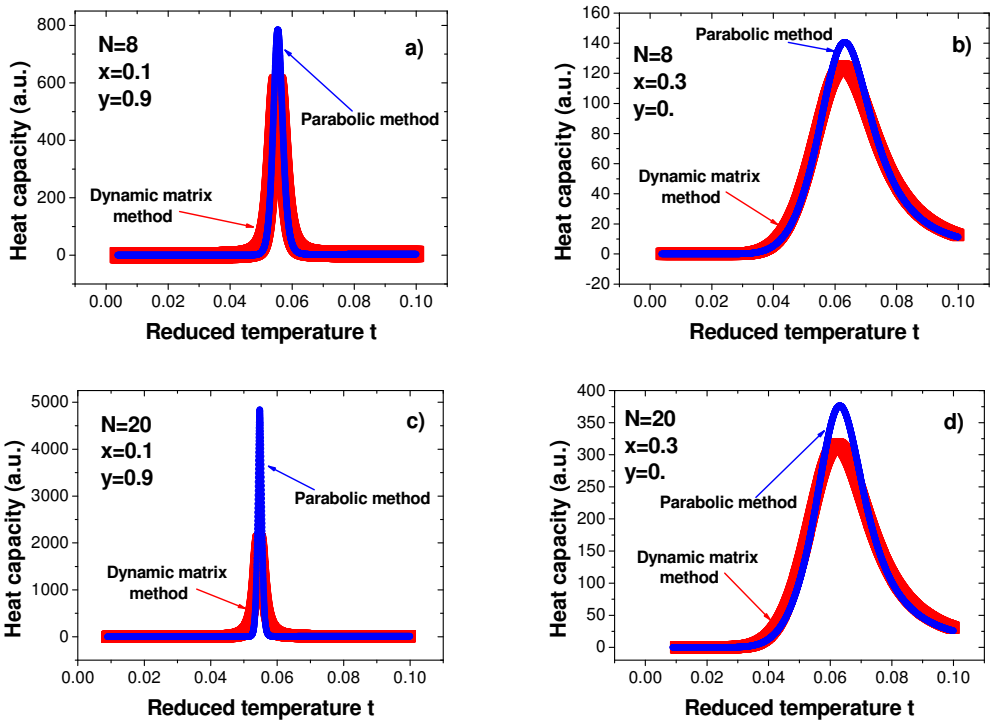

Figure 4.7 Time dependence of the heat capacity obtained using: the dynamic matrix method (red curve) and the parabolic method (blue curve) for two different sizes and interactions. Other parameter are g=1000 and δ=0.6.

The dynamic matrix method needs a higher computation power than the parabolic one, because it is necessary to generate all the 2^N (N = number of molecules) states of the system. For large systems, the parabolic method becomes more attractive and easier to apply from this point of view and in the next figures (4.8 and 4.9) are given the variation of entropy and heat capacity using parabolic method for N=50 molecules and N=100 molecules.

As was expected in the evolution of the entropy even if the size is big (N=100 molecules), for small interactions (figures 4.8b and 4.8d) the system does not present an abrupt thermal variation of the entropy as for large interactions (figures 4.8a and 4.8c). This aspect between the systems behavior is also a characteristic of the heat capacity evolution where for (x=0.1 and y=0.9) appears a dominant peak around T_c compared with results obtained with (x=0.3 and y=0.).

Finally, lets remark that the abrupt entropy which appears around T_c (in figure 4.8a and 4.8d) has been observed experimentally for $[Fe(phen)_2 (NCS)_2]$ and $[Fe(phen)_2 (NCSe)_2]$ compounds as can be found in some reviewed papers [15-18]. The anomalous large peak of the heat capacity around T_c reported in figures 4.9a and 4.9d has also been observed for the first time by Sorai and Seki [18] and was attributed to a phase transition.

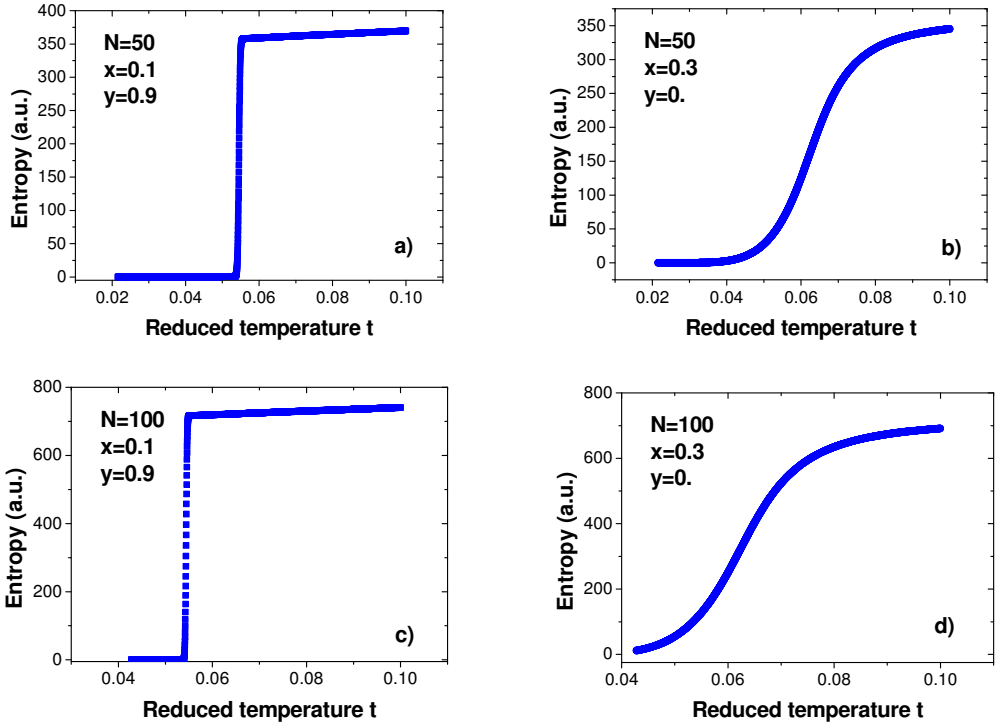

Figure 4.8 Thermal dependence of the entropy per atom obtained using parabolic method for two different sizes and interactions. Other parameter are g=1000 and δ=0.6.

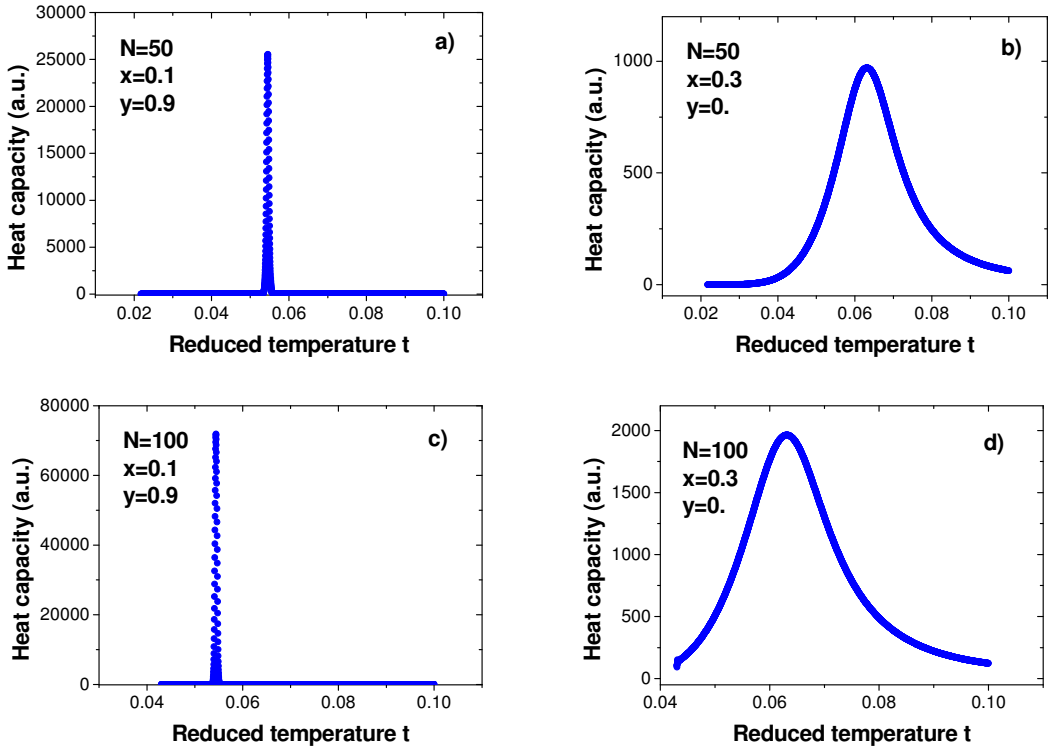

Figure 4.9 Thermal dependence of the heat capacity obtained using the parabolic method for two different size and interactions. The computational parameters used in the simulations are: g=1000 and δ=0.6.

4.5 The role of edge atoms using the dynamic matrix transfer and the free energy methods

Using Monte Carlo Metropolis (MCM) algorithm described in [19] the switching probability between the old state and the new state, P, is given by the following equation:

$$P_{state} = \frac{g^{nhs_{new}} e^{-\frac{\beta\Delta}{2}m_{new}} \prod_{i=1,N}\left[2\sinh\left(\frac{\hbar\omega_{new}}{2k_BT}\right)\right]^{-1}}{g^{nhs_{old}} e^{-\frac{\beta\Delta}{2}m_{old}} \prod_{i=1,N}\left[2\sinh\left(\frac{\hbar\omega_{old}}{2k_BT}\right)\right]^{-1}} \tag{4.39}$$

In the free energy method the magnetization M is calculated as follows:

$$M = \frac{\sum m_i \deg\xi_i}{\sum \deg\xi_i}\frac{1}{N} \tag{4.40}$$

where *deg* is the number of configurations with the same eigen value.
The high spin fraction n_{HS} giving the ratio between the number of atoms in the high spin state and the total number of atoms is defined as:

$$n_{HS} = (1+M)/2 \tag{4.41}$$

Using the following formula to calculate the free energy, F, we are able to study the stability of the system's state:

$$F(n_{HS}) = -Tln\left(\sum_{i=1}^{N}\xi_i\right) \tag{4.42}$$

To explain the role of edge atoms two types of systems were considered: an **A** type system in which the molecules are either HS and (or) LS and a **B** type system in which we add and fix at the beginning and at the end, one atom in the HS state to an **A** type system. In this case the system **A** can be **HS**……**HS-LS**……**LS** while the system **B** is of the form **HS+LS**……**HS-LS**……**LS+HS**. Figure 4.10 a) and b) show the evolution of the HS fraction, n_{HS}, as a function of temperature and the free energy for three different temperatures. In figure 4.10 a) besides the red curve, when the temperature is increasing and the blue curve when the temperature is decreasing (obtained by the transfer matrix method and the MCM algorithm), the results obtained by the numerical calculation previously described are plotted in black.

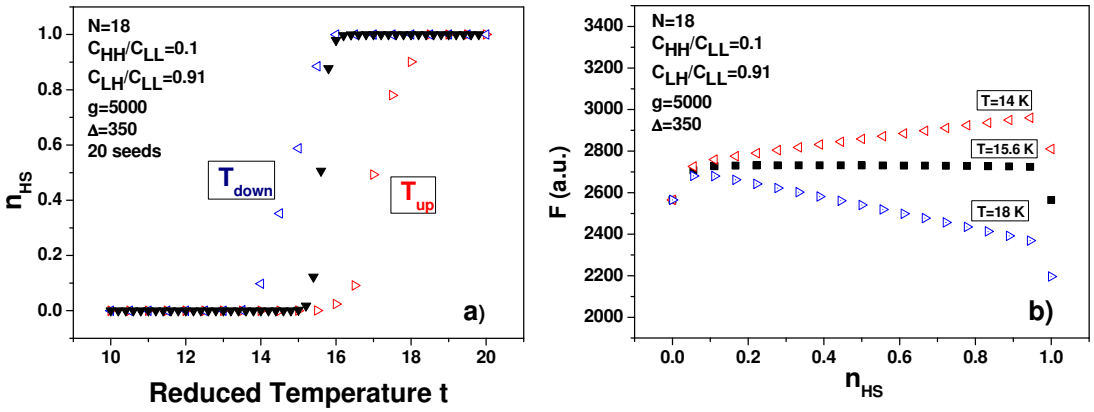

Figure 4.10 a) the simulated HS fraction, n_{HS}, as a function of the temperature and b) the free energy for three different temperatures for an **A** type system.

In figures 4.11 a) and b) are reported the HS fraction and the free energy for three different temperatures for a **B** type system. The comparison of the results reported in figure 4.10 a) with figure 4.11 a) shows that by adding and fixing the edge atoms in the HS state, the transition temperature is shifted to a lower temperature and the width of the hysteresis loop is decreased. Moreover the transition is more abrupt.

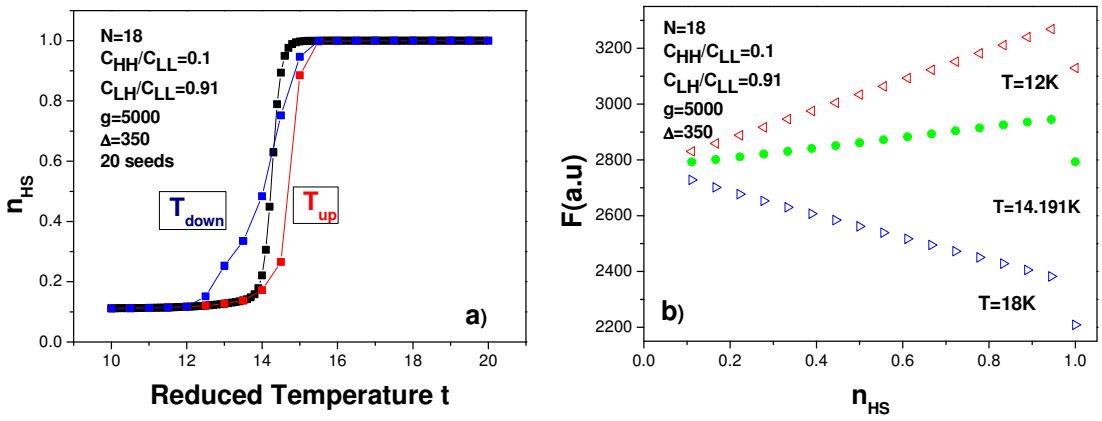

Figure 4.11 a) the simulated HS fraction, n_{HS}, as a function of the temperature and b) the free energy for three different temperatures for a **B** type system.

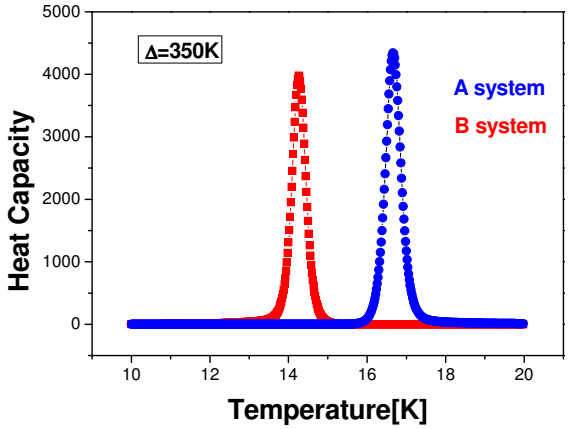

Figure 4.12 Thermal dependence of the heat capacity. The computational parameters are the same as those of figure 4.11.

4.6 Conclusion

In this chapter is presented a new method to describe the phonons contribution on the thermal behavior of SCO compounds using the APC model. Besides the use of the exact dynamical matrix method, the MFA approximation and the parabolic algorithm have been used, in order to simulate the thermal behavior when various parameters that play an important role on the spin crossover behavior are varied. We give herein a systematic comparison between the dynamic matrix and parabolic methods. For small N values, the exact method and the parabolic approximation give qualitatively the same behavior. Indeed, as reported in figure 4.3, the MFA leads to a hysteretic behavior in the thermal variation of the HS fraction, n_{HS}, while using the dynamic matrix and parabolic methods a thermal spin conversion is obtained. The parabolic method leads to the same thermal behavior of the SCO system as that obtained with the dynamic matrix method, especially for small sized system. However, for large systems, the entropy contribution plays an important role and a close correspondence between results given by these two methods is obtained only for high values

of the degeneracy ratio. For example, for N=8, this discrepancy disappears for g higher than 1000, that is when the variation of the entropy at the transition temperature is higher than $R\ln(g) = 57.9$ Joule K^{-1} mol^{-1}. This entropy variation value is common in SCO systems.

In conclusion, using the parabolic method we have reproduced the thermal evolution of the HS fraction and the entropy variation in 1D SCO systems. We established that, the thermal variation of the heat capacity is in good agreement with the results reported by Sorai and Seki [18] confirming that the SCO system presents a first order phase transition. The phase transition obtained using APC model confirms also the results already obtained using Ising-like models with both short-range and long-range interactions [20].

4.7 References

[1] J.A. Nasser, European Physical Journal B 21 (2001) 3.
[2] J.A. Nasser, K. Boukheddaden, J. Linares, European Physical Journal B 39 (2004) 219.
[3] J.A. Nasser, European Physical Journal B 48 (2005) 19.
[4] A. Gindulescu, A. Rotaru, J. Linares, M. Dimian, J. Nasser, Journal of Applied Physics 107 (2010) 09A959.
[5] A. Rotaru, J. Linares, E. Codjovi, J. Nasser, A. Stancu, *Journal of Applied Physics* 103 (2008) 07B908.
[6] J.A. Nasser, S. Topçu, L. Chassagne, M. Wakim, B. Bennali, J. Linares, Y. Alayli, *Eur. Phys. J. B* 83 (2011) 115.
[7] A. Rotaru, A. Graur, G.-M. Rotaru, J. Linares, Y. Garcia, *Journal of Optoelectronics and Advanced Materials* 14 (2012) 529
[8] A.P. Railliet, A.D. Naik, P. Castanho-Vaz, A. Rotaru, M. Grigoras, N. Lupu, J. Marchand-Brynaert, Y. Garcia, Hyperfine Interactions 217 (2013) 67.
[9] M.M. Dîrtu, C. Neuhausen, A.D. Naik, A. Rotaru, L. Spinu, Y. Garcia, Inorganic Chemistry 49 (2010) 5723.
[10] D. Chiruta, J. Linares, P.R. Dahoo, M. Dimian, Journal of Applied Physics 112 (2012).
[11] D. Chiruta, J. Linares, M. Dimian, Y. Garcia, European Journal of Inorganic Chemistry 2013 (2013) 951.
[12] L.L. Bonilla, A. Carpio, A. Prados, R.R. Rosales, Physical Review E 85 (2012) 031125.
[13] P.A. Rikvold, Z Physik B 26 (1977) 195.
[14] P.A. Rikvold, Z Physik B 30 (1978) 339.
[15] P. Gutlich, J. Jung, Nuovo Cimento Della Societa Italiana Di Fisica D-Condensed Matter Atomic Molecular and Chemical Physics Fluids Plasmas Biophysics 18 (1996) 107.
[16] P. Gütlich, A. Hauser, H. Spiering, *Angewandte Chemie-International Edition* 33 (1994) 2024.
[17] J. Zarembowitch, New Journal of Chemistry 16 (1992) 255.
[18] M. Sorai, S. Seki, J. Phys. Chem. Solids 35 (1974) 555.
[19] A. Rotaru, A. Carmona, F. Combaud, J. Linares, A. Stancu, J. Nasser, *Polyhedron* 28 (2009) 1684.
[20] D. Chiruta, J. Linares, S. Miyashita, K. Boukheddaden, Journal of Applied Physics 115 (2014) 194309.

Chapter 5

Pressure effect in molecular spin crossover compounds

Contents

5 Pressure effect in molecular spin crossover compounds

5.1 Analysis of the P-T-n_{HS} phase diagram of [Fe(hyptrz)]$A_2 \cdot H_2O$ spin crossover 1D coordination polymer

The increasing demand regarding safety and security rules lead to applications that involve advanced sensors with higher sensitivity, better technical specifications, lower dimensions andand low energy consumption. A special class of sensors is represented by temperature and pressure solid state sensors that allow direct or remote detection. This kind of sensing devices can be realized by developing new multifunctional materials exhibiting appropriate properties that can be controlled at the atomic or molecular level. Interesting properties that could be used in these applications are exhibited by molecular spin crossover (SCO) materials. The SCO phenomenon is a molecular process which combines an electronic transformation and atomic displacements in the coordination sphere of a central metal ion $3d^4$ –$3d^7$. Thus, the SCO usually occurs between a diamagnetic low-spin (LS) state and a paramagnetic high-spin (HS) state, which can be triggered by various external perturbations such as temperature, pressure, light or magnetic field [1-3]. In the course of the SCO phenomenon, physical properties (magnetic, optical, electrical, vibrational, etc.) of the material change dramatically and make possible to follow the process by various detection techniques (magnetic, optical, electrical, etc.) [1,2,4-6]. Among the various SCO systems available, 1D Fe(II) 1,2,4-triazole coordination polymers play a growing role, not only because this family of molecules can display both hysteretic and non-hysteretic behaviors, but also exhibits a very good optical contrast [7-10]. The last property is very important in optical detection of temperature or pressure variations [11]. However, due to both temperature and pressure sensitivity of a SCO material, the study of the pressure-temperature (p-T) phase diagram is mandatory. In this context, we present an experimental and theoretical study on the (p-T) phase diagram of a 1D SCO compound in order to find the optimal conditions of its use as temperature and pressure sensor in special environments such as cryogenic temperatures and/or high pressures. Indeed, there is a current need of temperature and pressure sensors with non-contact detection that could work at cryogenic temperatures and high pressure, respectively in a temperature/pressure range as large as possible.

One remarkable successful model used in the description of bistable SCO systems is the Ising-like model, which describes interacting two-level units; the energy levels having different energies and degeneracies [12]. In this chapter, the Ising-like model was used for describing both static and dynamic properties of SCO compounds under different external stimuli such as temperature and pressure [13,14].

Described in the chapter 1, in this chapter are recalls only some important equations of Ising like model. So, the Ising Hamiltonian can be written as follows:

$$H = \frac{\Delta - k_B T \ln g}{2} \sum_i \hat{\sigma}_i - J_{i,j} \sum_{\langle i,j \rangle} \hat{\sigma}_i \hat{\sigma}_j - G \sum_{<i>} \hat{\sigma}_i \langle \hat{\sigma} \rangle \tag{5.1}$$

where $\hat{\sigma}$ is the fictitious spin operator with the eigen values $+1$ (when the molecule is in the HS state) and -1 (when the molecule is in the LS state); $\sum_{\langle i,j \rangle}$ - denotes the sum over nearest neighbouring spins; the gap energy, $\Delta = E(HS) - E(LS)$ is the internal energies differences between the HS and LS; the term $k_B T \ln g$ take into account the entropy contribution (g is the degeneracy ratio); $J_{i,j}$ stands for the short-range interaction parameter that represents the

cooperative interaction that only exists between the nearest neighboring pairs ($J_{i,j}$ includes the nearest neighbors number) and finally G is long range interaction parameter.
The equilibrium temperature $T_{1/2}$ for which $n_{HS} = n_{LS} = 1/2$ corresponds to a zero effective field, irrespectively of the interactions: $T_{1/2} = \Delta / k_B \ln g$.

5.1.1 Pressure effect

Over the last few years an important effort has been done by different laboratories to explain, experimentally [15-23] or theoretically [24-28], different unusual behaviors of SCO complexes under an external applied pressure. Due to the change in the metal-ligand bond length when the SCO occurs, these materials are highly sensitive to an external applied pressure. The bistable properties at the molecular level are adequately described through a molecular configurational diagram, i.e. a plot of the adiabatic energy vs. the distortion coordinate of the molecular system. Indeed, it is already known that by applying an external pressure the energy gap is increasing, due to the decrease of the metal-ligand bond length, and by consequence the activation energy, E_a will decrease (see figure 5.1) and the LS state will be stabilized.

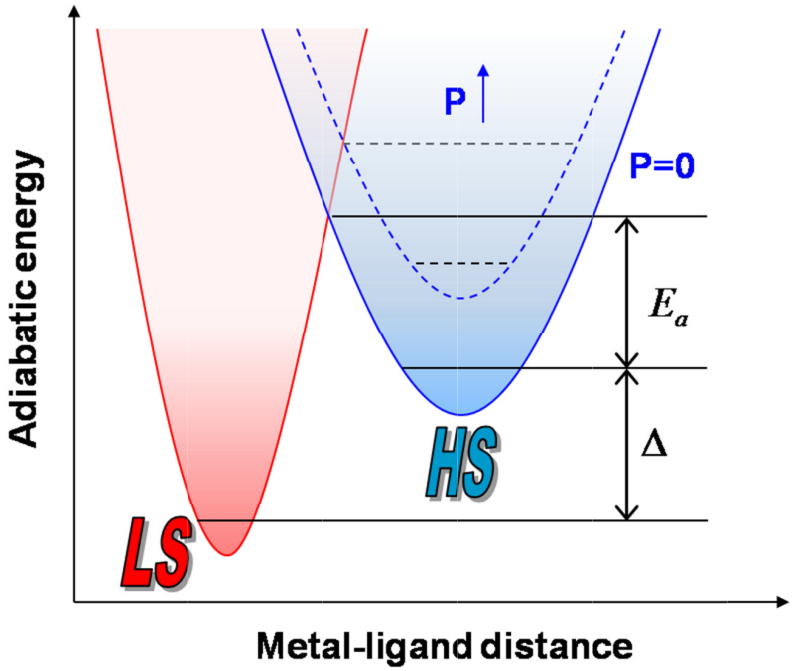

Figure 5.1. Pressure effect on the configurational diagram of a bistable SCO system.

The pressure dependence of the energy gap is:

$$\Delta(T, p) = \Delta(T, p = 0) + p\delta V \tag{5.2}$$

where δV is the volume variation and p is the external applied pressure.

Assuming that all sites are equivalent, the mean field treatment is performed as usual, so that the one-site mean field Hamiltonian can be written as:

$$H_{equiv} = \frac{\Delta(T, p)}{2}\hat{\sigma} - (qJ + G)\hat{\sigma} < \hat{\sigma} > \tag{5.3}$$

where q is the nearest neighbors number, $< \hat{\sigma} >= m$ is the „fictious magnetization", that can be written as:

$$< \hat{\sigma} >= m = \tanh\left(\frac{(qJ+G)m}{k_B T} + \frac{k_B T \ln g - \Delta(T,p)}{2k_B T} \right) \tag{5.4}$$

For the sake of simplicity, in calculations we used the following reduced parameters: the reduced energy gap, $\Delta = \Delta(T,p)/k_B$, reduced interaction parameter $\Gamma = (qJ+G)/k_B$, (which contains the short and long range contribution) and reduced volume variation, $\alpha = \frac{\delta V}{k_B} 10^{-5}$ (the factor 10^{-5} stands for the pressure units conversion from Pascal to Bar).

The HS fraction is usually expressed as a function of a fictious magnetization m: $n_{HS} = (m+1)/2$.

Equation (5.4) allows to plot both thermal and pressure dependence of the HS fraction, as shown in figure 5.2.

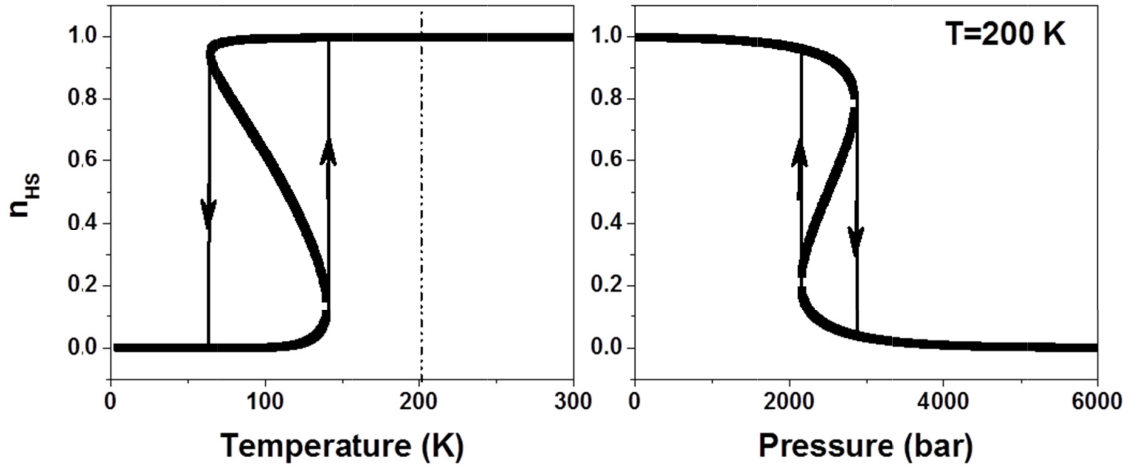

Figure 5.2 Simulated thermal hysteresis loop, at ambient pressure (a) and pressure hysteresis loop, recorded at 200 K (b). The values of the parameters used in calculations are: Δ/k_B=800K, Γ/k_B = 300 K, $ln(g)$ = 7 and δV=13.2 Å^3.

In order to use SCO molecular systems in temperature and pressure sensing devices the system's output signal (HS fraction in our case) should be linearly dependent on the input perturbation, i.e. temperature and/or pressure variation in our case [11]. Thus, the best characteristics will be demonstrated by a very low cooperative SCO system, which exhibits a gradual spin conversion as linear as possible. However, we will show hereafter that, in some critical conditions (high temperature and/or high pressure), even SCO materials with a large hysteresis at ambient pressure could be used, not only in differential pressure measuring as it was stated in [11], but also as a pressure gauge (or temperature sensor) in a continuous detection range.

5.1.2 Results and discussions

Due to the fact that SCO materials are both thermal and pressure sensitive, it is very important to analyze the pressure-temperature (p-T) phase diagram. Regarding this issue, very few attempts have been noticed to record the (p-T) phase diagram by using various detection techniques such as optical reflectivity [19-21,29-31], magnetic techniques [15-18,32-34], X-ray and neutron diffraction [35-39]. This lack of data could be explained by the difficulty to obtain small variations in the applied pressure in both loading and unloading processes, at variable temperatures. A solution to this issue makes use of gas pressure cells that have already proved their capacity to increase and decrease pressure with rather small steps (~10

bar). Moreover, the hydrostatic character of a gas pressure cell is kept in the whole temperature range, contrary to other pressure cells type (such as clamp type or DAC), that uses silicone oil, Flourinert FC70/77, NaCl, etc. as pressure transmitting medium which freezes at cryogenic temperatures and the hydrostaticity might be lost. An exhaustive study on the evaluation of pressure-transmitting media for cryogenic experiments is given in reference [40].

5.1.3 Pressure-Temperature (p-T) phase diagram

The color change associated to the spin state switching of some SCO complexes makes possible to track the HS molar fraction evolution under the influence of different stimuli by optical methods. We used a gas pressure cell equipped with a safire optical window and a cryostat. The experimental setup has been described elsewhere [19,31], as well as the synthesis of the thermochromic 1D SCO coordination polymer [Fe(hyptrz)]$A_2 \cdot H_2O$ (hyptrz=4-(3'-hydroxypropyl)-1,2,4-triazole and A = 4-chloro-benzenesulfonate) [41].

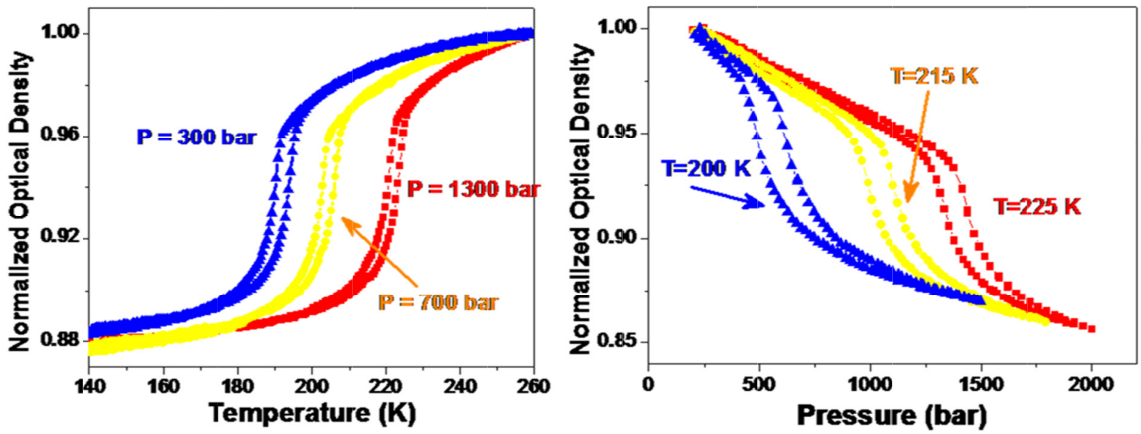

Figure 5.3 Selected thermal (left) and pressure (right) hysteresis loops recorded at several pressures and temperatures, respectively for [Fe(hyptrz)]$A_2 \cdot H_2O$.

Several thermal hysteresis loops under different pressures and pressure hysteresis loops taken at different temperatures have been successfully recorded for [Fe(hyptrz)]$A_2 \cdot H_2O$ (Figures 5.3 and 5.4). Figure 5.3 illustrates the thermo- and piezochromic behavior of the 1D polymer under an external applied pressure. When the pressure is increased, the transition temperatures shift higher with 33 K/kbar and the hysteresis width decreases progressively (figure 5.4). A similar effect is observed for the pressure hysteresis loop where the hysteresis width is decreasing with the increase of temperature (figure 5.3). These results allow us to plot the experimental 2D (p-T) phase diagram (figure 5.4).

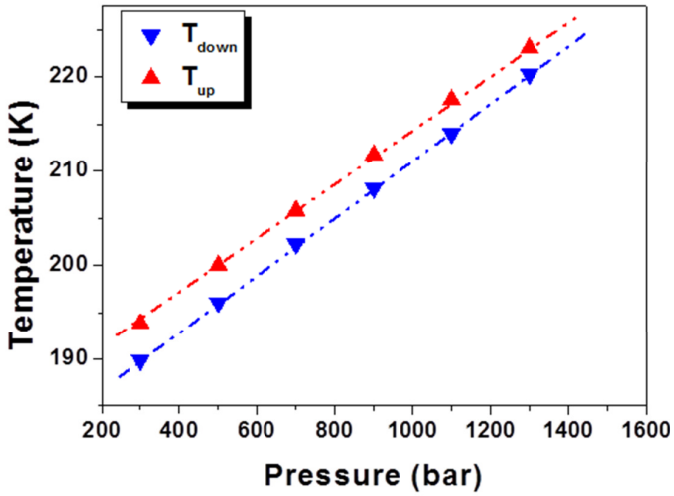

Figure 5.4 Experimental 2D p-T phase diagram recorded on [Fe(hyptrz)]$A_2 \cdot H_2O$.

Figure 5.5 displays the experimental 3D (p-T-n_{HS}) phase diagram recorded by diffuse reflectivity, which is only partial because of the limitation of our experimental setup (the maximum reached pressure was ~2 kbar). However our setup allowed us to change the pressure in small steps of about 10 bars in both loading (increasing pressure) and unloading (decreasing) modes. We should mention herein that the pressure effect on this SCO complex has been already studied elsewhere by using a clamp type pressure cells [32,41]. In this study a reentrance phenomenon under pressure of [Fe(hyptrz)]$A_2 \cdot H_2O$ was revealed. However, in this work the authors resumed their study to record the thermal behavior at different external pressures. This unusual effect has been explained in the frame-work of the atom-phonon coupling model by considering that the elastic constant value of an antiferromagnetic configuration (HS-LS) is closer to the value of the elastic constant of a HS-HS configuration [26].

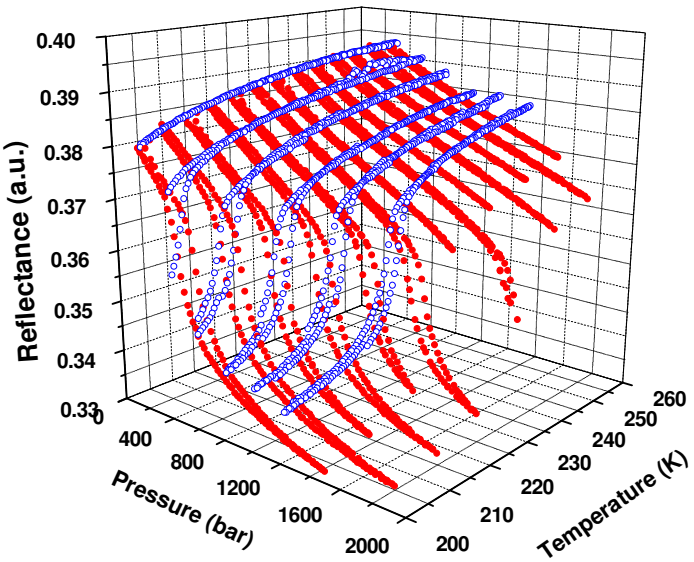

Figure 5.5 Incomplete experimental 3D (p-T-n_{HS}) phase diagram recorded on [Fe(hyptrz)]$A_2 \cdot H_2O$.

In order to get more information on the pressure effect and to identify the best properties of a SCO complex that should be used in temperature and pressure sensing applications, we extended our work with a theoretical study of the 3D phase diagram.

The phase diagram in (p-T-n_{HS}) units of an isolate system (uncooperative), described by a null effective interaction parameter Γ=0, is displayed in figure 5.6. By increasing the applied pressure, we note that the thermal dependence becomes more gradual. A similar effect is observed in the pressure dependence of the HS fraction recorded under increasing pressures. This kind of behaviors is suited for temperature and pressure sensors. By recording the optical density in both HS and LS spin states and its corresponding temperatures, the device could be calibrated in order to be used as a temperature or pressure sensor.

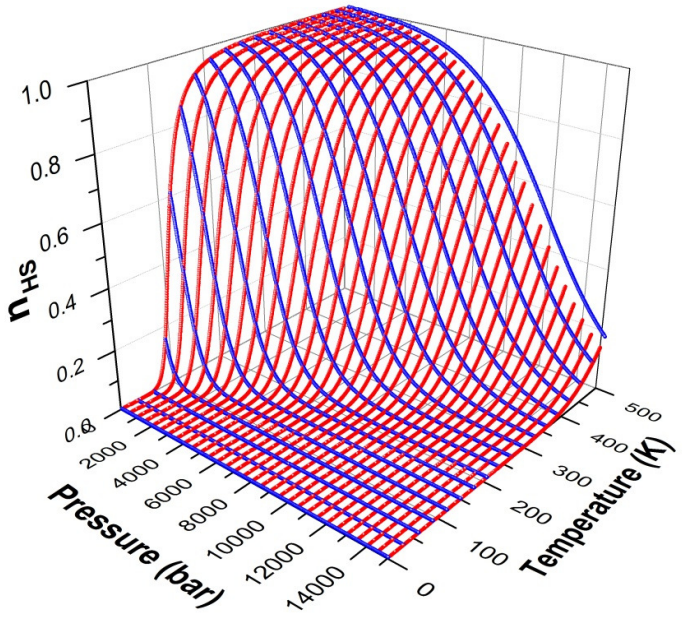

Figure 5.6 Simulated 3D (p-T-n_{HS}) phase diagram characteristic to a non-cooperative SCO system. The values of the parameters used in calculations are: Δ/k_B = 800 K, Γ/k_B = 0 K, ln(g) = 7 and δV=13.2 Å^3.

When the intermolecular interactions are taken into account i.e. $\Gamma \neq 0$, above a critical value of Γ, the spin transition occurs with a hysteresis (see figure 5.7). Despite these properties could be exploited in technological applications such as molecular switches or as recording media, these are not appropriate for temperature and pressure sensing applications. However, getting profit from pressure effect, we show that even an highly cooperative system could be used as temperature and pressure sensor. Indeed, when the applied pressure is increased the hysteresis width decreases until it completely vanishes (see figure 5.7). The critical curve that separates the hysteretic behavior from the non-hysteretic one is known as spinodal curve. Thus, starting from the equation (5.4), we write:

$$\operatorname{artanh}(m) = \frac{1}{2}\ln\left(\frac{1+m}{1-m}\right) = \frac{2\Gamma m + T\ln g - \Delta}{2T} \tag{5.5}$$

Thus, we obtain the dependence of temperature *T* as a function of *m*:

$$T = \frac{2\Gamma m - \Delta}{\ln\left(\frac{1+m}{1-m}\right) - \ln g} \tag{5.6}$$

The spinodal curve can be founded by computing $dT/dm = 0$ (or $dp/dm = 0$). Thus, the spinodal curve will be described by the following expression:

$$\frac{dT}{dm} = \frac{\Gamma\left[\left(m^2-1\right)\left(\ln\left(\frac{1+m}{1-m}\right)-\ln g\right)+2m\right]-2\Delta}{\left[\ln g-\ln\left(\frac{1+m}{1-m}\right)\right]^2\left(m^2-1\right)} = 0 \qquad (5.7)$$

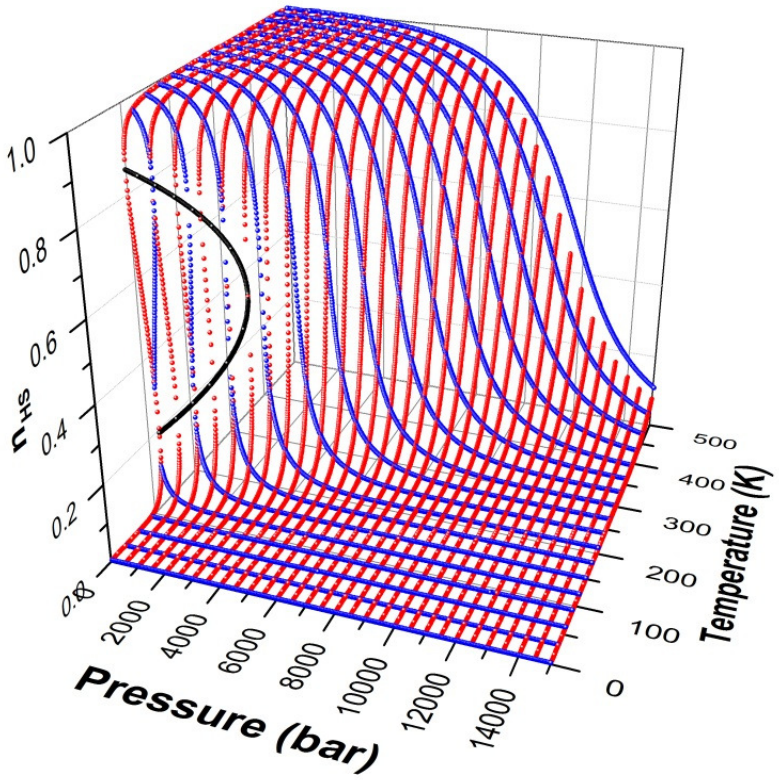

Figure 5.7 The phase diagram (p-T-n_{HS}) calculated for a cooperative system characterized by a short-range interaction parameter of Γ/k_B = 200 K. The black curve represents the spinodal curve. The values of the parameters used in calculations are: Δ/k_B = 800 K, Γ/k_B = 300 K, ln(g) = 7 and δV=13.2 $\dot{A}^3$.

Of course, the spinodal curve is a function of interaction parameter, Γ, i.e. the larger is the Γ-value, the more extended will be the hysteretic region (see figure 5.8).

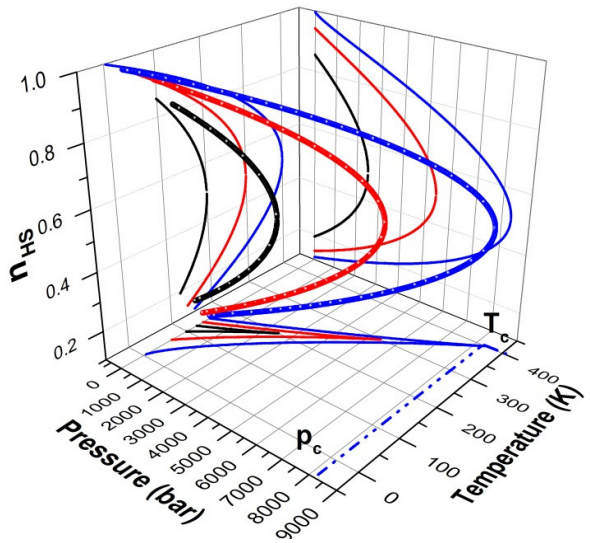

Figure 5.8 Simulated 3D P-T-n_{HS} spinodal curve and its projections on the coordination planes for various values of the interaction parameter: from left to right: Γ/k_B = 200 K, Γ/k_B = 300 K, Γ/k_B = 400 K. The values of the parameters used in calculations are: Δ/k_B = 800 K, lng = 7 and δV=13.2 Å^3.

Indeed, for pressures and/or temperature higher than the critical value (p_c and T_c respectively) the SCO system loose the hysteretic behavior and the spin transition from one spin state to another occurs gradually, property suited in specific sensors applications [8].

5.2 Impact detection using SCO materials

The continuous developments of chemical systems allows the selection of the best SCO systems with special requirements concerning the SCO temperature region, which need to be located around room temperature region as well as the width of their bistability domain which need to be as large as possible. Following these conditions, we decided to focus on the 1D chain $[Fe(hyetrz)_3]I_2 \cdot H_2O$ (hyetrz = 4-(2'-hydroxyethyl)-1,2,4-triazole) as a suitable candidate. This material is known to exhibit a cooperative and thermo chromic spin transition from LS (S = 0, violet) to HS (S = 2, white) around the room temperature region [42]. In this work we show that $[Fe(hyetrz)_3]I_2 \cdot H_2O$ can be used as a visual detector of strong mechanical contact pressure from 25 MPa to 250 MPa. This result is supported by thermal dependence of the optical reflectivity measurements, ^{57}Fe Mössbauer spectroscopy and differential scanning calorimetry. A correlation of SCO properties with the pressure contact is made thanks to an Ising-like model. These results provide the basis for the construction of a marker pressure device.

5.2.1 Results and discussions

The colour change of the sample from white (HS) to violet (LS) was monitored through variable-temperature optical reflectivity measurements in a dry nitrogen atmosphere at 2 K/min. The thermal dependence of the diffuse reflectance has been recorded, simultaneously, spectroscopically and at a quasi-monochromatic wavelength of λ = 550(50) nm (see figure 5.9).

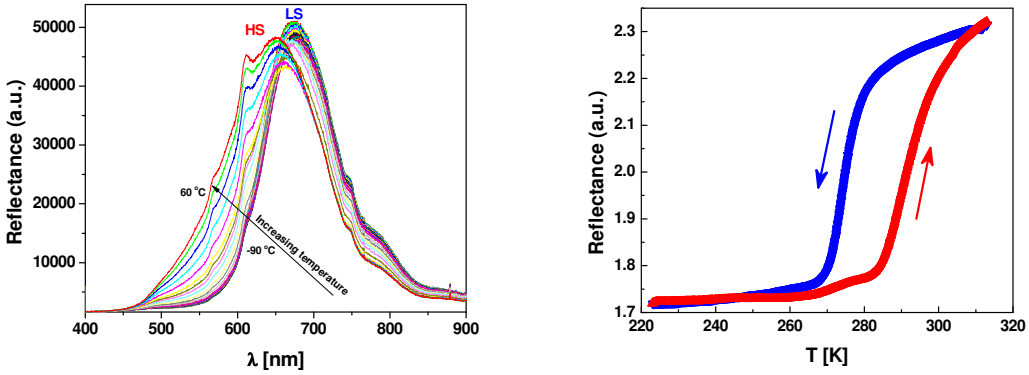

Figure 5.9 Thermal evolution of reflectance spectra recorded on $[Fe(hyetrz)_3]I_2 \cdot H_2O$ in the solid state (left) and of the optical density at λ = 550 nm (right).

The hysteretic SCO behaviour around room temperature is confirmed for $[Fe(hyetrz)_3]I_2 \cdot H_2O$ at $T_c^{\uparrow}$ = 292 K and $T_c^{\downarrow}$ = 275 K by optical reflectivity measurements (figure 5.9). The high colour contrast of the sample, between the two spin states, can be tracked by recording temperature dependence of the reflectance spectra. figure 5.9 (left) displays the temperature dependence of the diffuse reflectance, recorded in cooling mode. In these measurements was used a 100 W halogen bulb, which is installed on the optical microscope. At the lowest temperature, the reflectance spectrum shows a band centred on 680 nm which is assigned to the LS state, in good agreement with the pink colour of the sample. With increasing the temperature, a blue shift of the spectrum maximum is observed, followed by a broadening of the reflectance spectrum, in good agreement as well with the white colour of the sample in the HS state. It is worth noting that the reflectance spectra display an important background from the light source light, which is however constant for all experiments ensuring that the observed changes originate from the sample's colour change. By integration of these spectra using a photodiode, for each temperature, the SCO curve as a function of temperature could be obtained (figure 5.9-right). The optical characterization has been completed by differential scanning calorimetric (DSC) measurements which were undertaken to confirm the spin transition temperature range as well as to determine, quantitatively, the thermodynamic parameters to be used in our Ising model described hereafter.

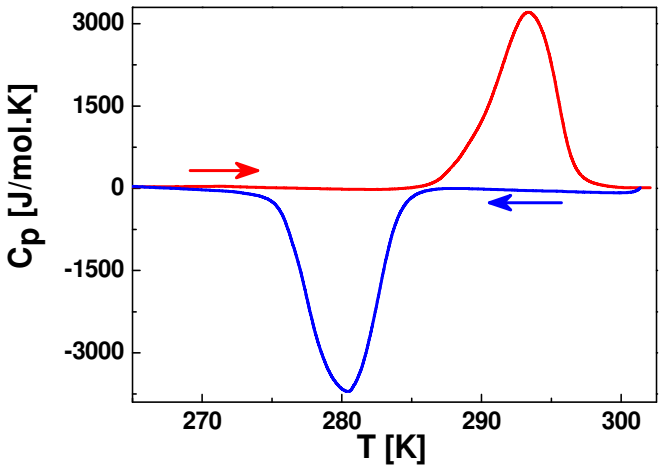

Figure 5.10 DSC curves for $[Fe(hyetrz)_3]I_2 \cdot H_2O$ over the 265-303 K temperature range.

The DSC curve, recorded at 10 K/min in the heating and cooling modes (figure 5.10), shows an endothermic peak at $T_{max}^{\uparrow}$ = 293 K and an exothermic peak at $T_{max}^{\downarrow}$ = 280 K, in fair agreement with the transition temperatures observed from optical measurements. The difference seen in the lower branch of the spin transition curve is associated to the lower scan rate (2K/min) used for the optical measurements. The enthalpy and entropy variations were determined as ΔH = 16.42 kJmol^{-1} and ΔS = 57.42 J.mol^{-1}K^{-1}. The experimentally measured entropy variation accounts for an electronic contribution, Rln5 = 13.4 J.mol^{-1}K^{-1}, and a vibrational contribution of 41.77 J.mol^{-1}K^{-1}. These values were corrected taking into account the active sites fraction associated with the spin transition which was accurately determined from complimentary Mössbauer spectroscopy measurements detailed below. Indeed on cooling to 78 K, a single quadrupole doublet with isomer shift δ^{LS} = 0.50(1) mm.s^{-1} was observed indicating 100% LS ions. The presence of a quadrupole splitting ΔE_Q^{LS} = 0.24(1) mm.s^{-1}, indicates a distortion of the octahedral as expected within a 1D chain [43]. At 318 K, the temperature for which the compound is expected to have undergone the spin transition, according to optical reflectivity measurements (figure 5.9), the spectrum shows a major quadrupole doublet (87%) attributed to HS Fe^{II} (δ = 0.99(1) mm.s^{-1} and ΔE_Q = 2.49(2)mm.s^{-1}) and a minor one (13%) corresponding to LS Fe^{II} (δ = 0.36 mm.s^{-1} and ΔE_Q = 0.17(5)mm.s^{-1}). Thus [Fe(hyetrz)$_3$]I$_2$·H$_2$O undergoes an incomplete ST on warming with 13% of non switching sites, which need to be taken into account for the enthalpy determination associated with the spin state change.

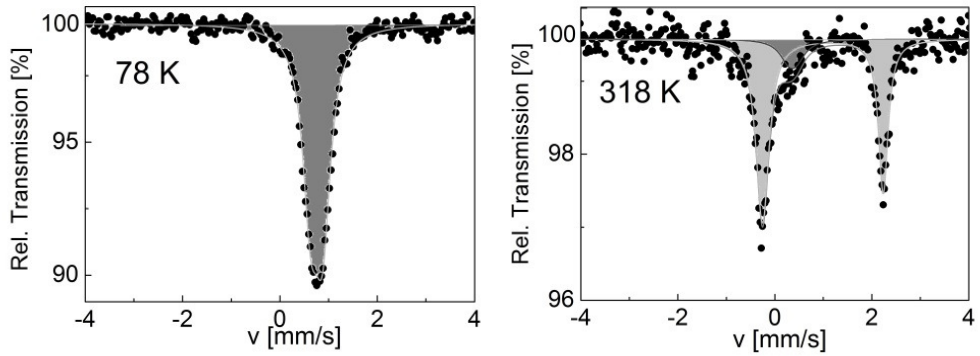

Figure 5.11 ^{57}Fe Mössbauer spectra for [Fe(hyetrz)$_3$]I$_2$·H$_2$O at 78 K (left) and 318 K (right).

Pressure experiments were carried out on a home-made micromechanical device. The sample was deposited on a metal plate and covered with a scotch tape (figure 5.12).

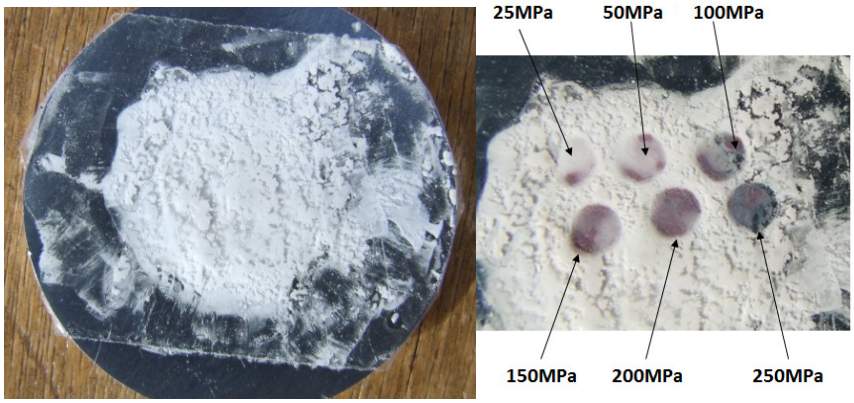

Figure 5.12 (Left): sample holder showing the SCO compound at room temperature on its sample holder covered with a scotch tape. (Right): Enlarged view of the sample evidencing colour change to pink at room temperature for various applied pressures (25 MPa, 50 MPa, 100 MPa, 150 MPa, 200 MPa and 250 MPa).

As shown in figure 5.12, the material is white at room temperature and ambient pressure which is characteristic of the HS state. The pressure was applied at selected spots on the sample, released and a photograph was taken again. As it can be seen, for a threshold value of the applied pressure of ca. 30 MPa, the SCO powder switches from white (HS) to pink (LS) and retain its colour (spin state) when pressure is released. On warming to 303 K, the powder switches back to white (HS state), making the sensor reusable.

From the DSC measurements, and taking into account 87% of spin switching determined by Mössbauer measurements, the entropy value calculated $\Delta S = 57.42\ J.mol^{-1}K^{-1}$ gives a degeneracies ratio state of the two spin state, *g,* such as $lng = 6.906$ and the enthalpy variation give a gap energy $\Delta_0/k_B = 1978.6\ K$. For the volume variation (δV) during the spin transition (LS→HS, HS→LS), we used a typical value of volume change $\delta V = 100\ A^3$.

The thermal and pressure dependence of the HS molar fraction, n_{HS}, at ambient pressure and temperature, computed for $[Fe(hyetrz)_3]I_2 \cdot H_2O$, i.e. for a complex displaying a hysteretic spin transition around room temperature is displayed in figure 5.13. The transition temperatures at atmospheric pressure are $T_c^{\uparrow}$ = 292.5 K and $T_c^{\downarrow}$ = 278.8 K, which are in excellent agreement with the ones detected by optical reflectivity (figure 5.9). The transition pressures at 300 K are $P_c^{\downarrow}$ = 17.5 MPa and $P_c^{\uparrow}$ = 8.2 MPa.

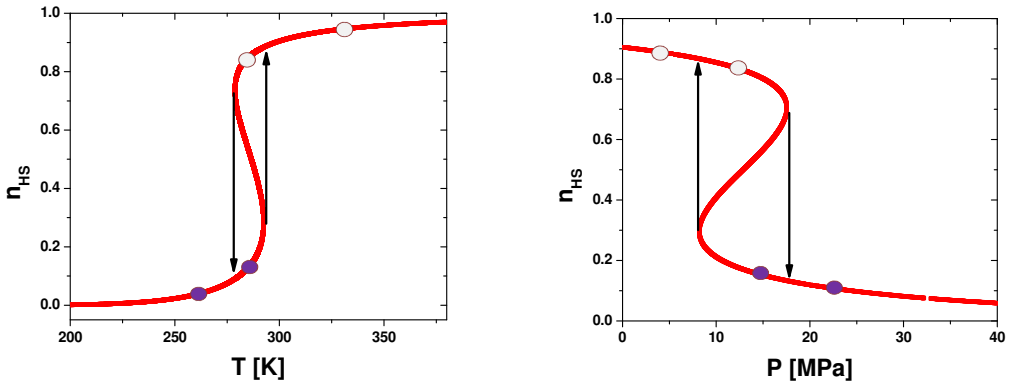

Figure 5.13 Thermal dependence at 1 bar (left) and pressure dependence at 300 K (right) of the HS molar fraction, n_{HS}, as derived from the Ising like model. The parameters values are Δ_0/k_B = 1978.6 K, δV = 100 A^3, ln(g) = 6.906 and Γ/k_B = 360 K.

A (P-T) phase diagram was generated to better understand the influence of temperature and pressure on the SCO behaviour. The calculated phase diagram in pressure-temperature coordinates using the same parameters as in figure 5.13, is displayed in figure 5.14.

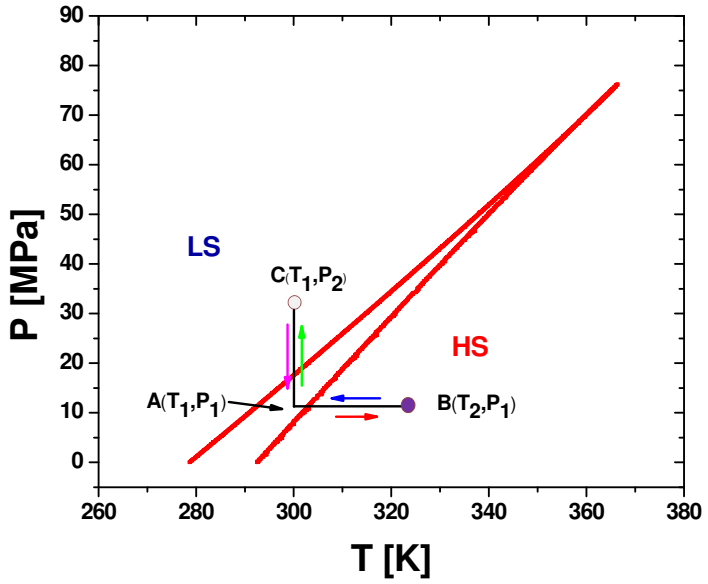

Figure 5.14 Pressure-temperature phase diagram calculated for a SCO system switching around the room temperature region using the following parameters values: Δ_0/k_B = 1978.6 K, δV = 100 A^3, ln(g) = 6.906 and Γ/k_B = 360 K.

As can be seen from figure 5.14, the transition from the HS to the LS state can be achieved either by decreasing the temperature or by increasing the pressure. When the SCO compound located at point **A**, i.e. at given temperature $\mathbf{T_1}$ and pressure $\mathbf{P_1}$, is heated until it reaches point **B** of temperature $\mathbf{T_2 \geq T_{up}}$ at a constant pressure $\mathbf{P_1}$, a switch back to the HS state is observed. From **B**, if the temperature is decreased until it gets back to point **A** ($\mathbf{T_1, P_1}$) then the compound remains in the HS state. By applying a pressure, the compound switches from HS to LS states at point **C** ($\mathbf{T_1, P_2 > P_{down}}$). If now the pressure is lowered back to $\mathbf{P_1}$ (point **A**), the compound will remain in the LS state. In other words, inside the hysteresis width, the compound will keep the state of origin. When coming from the LS state it will remain in the LS state and when coming from the HS state it will retain the HS state as shown in figure 5.15.

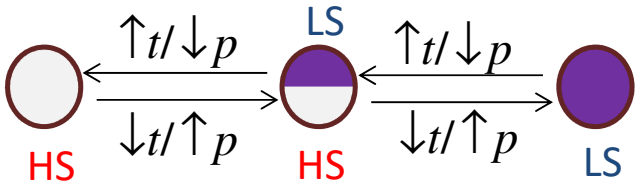

Figure 5.15 Representation of the switching mechanism induced by temperature and/or by pressure.

5.3 Sensor concept

The use of SCO compounds as active components in thermal and pressure sensor devices was discussed in a few papers [9,11,44], but did not yet considered the attractive possibility to monitor at the same time both pressure and temperature due to the existence of multiple sets of *T*, *P* solutions that results from the p-T phase diagram. In this subsection is presented a novel concept for spin crossover-based sensors that allow the concomitant detection of both temperature and pressure using two different SCO materials that exhibit

gradual transitions. So, let's to consider two SCO materials characterized by de following parameters:

- compound 1: $\Delta_1^{'}, \delta V, g_1$ *and* Γ_1;
- and compound 2: $\Delta_2^{'}, \delta V, g_2$ *and* Γ_2.

The fictitious magnetizations, according with equation (5.4), of the two compounds can be written as:

$$\begin{cases} \langle\sigma_1\rangle = \tanh\left(-\dfrac{\Delta_1^{'} + pc\delta V - T\ln g_1 - 2\Gamma_1\langle\sigma_1\rangle}{2T}\right) \\ \langle\sigma_2\rangle = \tanh\left(-\dfrac{\Delta_2^{'} + pc\delta V - T\ln g_2 - 2\Gamma_2\langle\sigma_2\rangle}{2T}\right) \end{cases} \tag{5.8}$$

where c is a constant equal to 0.0724, when the external applied pressure, p, is expressed in MPa and the volume variation of the molecule, δV, is expressed in Å^3.
Now, by solving the system of Equations (5.8), the expressions for T and p can be written as:

$$\begin{cases} T = \dfrac{2\Gamma_1\langle\sigma_1\rangle - \Delta_1^{'} - 2\Gamma_2\langle\sigma_2\rangle + \Delta_2^{'}}{2\tanh^{-1}\langle\sigma_1\rangle - \ln g_1 - 2\tanh^{-1}\langle\sigma_2\rangle + \ln g_2} \\ p = \dfrac{\left(2\Gamma_1\langle\sigma_1\rangle - \Delta_1^{'}\right)*\left(2\tanh^{-1}\langle\sigma_1\rangle - \ln g_1 - 2\tanh^{-1}\langle\sigma_2\rangle + \ln g_2\right) - \left(2\Gamma_1\langle\sigma_1\rangle - \Delta_1^{'} - 2\Gamma_2\langle\sigma_2\rangle + \Delta_2^{'}\right)*\left(2\tanh^{-1}\langle\sigma_1\rangle - \ln g_1\right)}{c\delta V*\left(2\tanh^{-1}\langle\sigma_1\rangle - \ln g_1 - 2\tanh^{-1}\langle\sigma_2\rangle + \ln g_2\right)} \end{cases} \tag{5.9}$$

From the system of Equations (5.9) we can find simultaneously both values of temperature and pressure knowing the values of $<\sigma_1>$ and $<\sigma_2>$. These values can be obtained by identifying the optical densities of each complex. The projected device must be initially calibrated using their optical densities. Compounds that could be adapted to this device should exhibit gradual transitions. Practically, our concept can be described as follows. A monochromatic light source (green light = 540 nm) is sent to both compounds. The "scattered" or reflected light by the compounds are directed on the detector (see Figure 5.16). The detector, calibrated previously, will assign the $<\sigma_1>$ and $<\sigma_2>$ that corresponds to the lights coming from both compounds. The temperature and pressure values are obtained by replacing the $<\sigma_1>$ and $<\sigma_2>$ in Equations (5.9). The challenge for chemists will be to synthesize SCO compounds with a good optical contrast and which will be thermally, pressure and time stable. In other words, to elaborate samples which keep the same color over time at a defined temperature and pressure set. This objective looks not too far to be achieved considering recent developments in the SCO field.

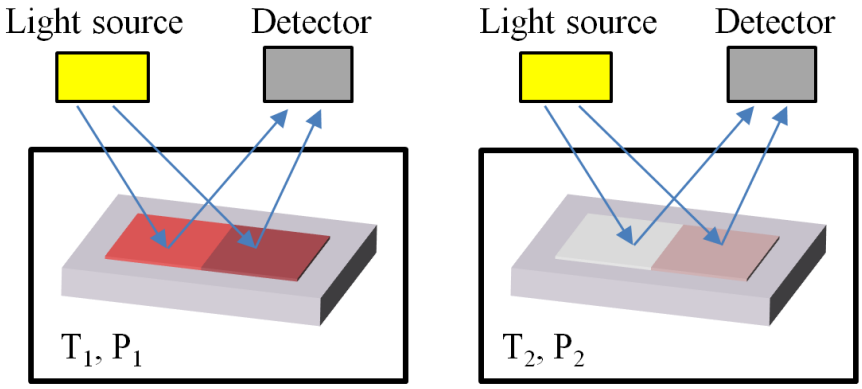

Figure 5.16 Principle of measuring simultaneously temperature and pressure using two SCO compounds with optical reflectivity detection.

5.4 Conclusions

In this chapter two experimental studies was presented. In the first study the thermo-and piezochromic properties of the [Fe(hyptrz)]$A_2 \cdot H_2O$ spin crossover 1D chain have been analyzed. The experimental study was completed by a theoretical investigation to predict the bistability region for this compound.

In the second part of this chapter was proved the feasibility of pressure detection using a molecular spin crossover based sensor/marker operating at ambient temperature. For the SCO compound $[Fe(hyetrz)_3]I_2 \cdot H_2O$, we obtained a threshold value of the contact pressure of about 30 MPa to irreversibly induce the color change of the molecular material, due to the spin state switching form HS to LS state. Noticeably, the possibility to switch back the color using another stimulus (temperature) was demonstrated making this sensor reusable. As in a previously case, a theoretical investigation in the framework of the Ising-like model has been presented. These results open important perspectives for molecular materials in pressure sensing applications, making possible their insertion in piezo- and thermo-chromic paints that will allow the visual detection of mechanical collisions, a very important issue in the aeronautic and automotive industries.

The chapter ends with a proposal of concept for spin crossover-based sensors that allow the concomitant detection of both temperature and pressure using two different SCO materials.

5.5 References

[1] A. Domingo, M. Verot, F. Mota, C. de Graaf, J.J. Novoa, V. Robert, Physical Chemistry Chemical Physics 15 (2013) 6982.

[2] M.A. Halcrow, *Spin-Crossover Materials. Properties and Applications.*, John Wiley & Sons, Ltd., 2013.

[3] P. Gütlich, A.B. Gaspar, Y. Garcia, Beilstein Journal of Organic Chemistry 9 (2013) 342.

[4] A. Rotaru, I.y.A. Gural'skiy, G. Molnar, L. Salmon, P. Demont, A. Bousseksou, Chemical Communications 48 (2012) 4163.

[5] A. Bousseksou, G. Molnar, L. Salmon, W. Nicolazzi, *Chemical Society Reviews* 40 (2011) 3313.

[6] A. Rotaru, J. Dugay, R.P. Tan, I.A. Gural'skiy, L. Salmon, P. Demont, J. Carrey, G. Molnar, M. Respaud, A. Bousseksou, Advanced Materials 25 (2013) 1745.

[7] M.M. Dîrtu, A. Rotaru, D. Gillard, J. Linares, E. Codjovi, B. Tinant, Y. Garcia, Inorganic Chemistry 48 (2009) 7838.

[8] M.M. Dîrtu, C. Neuhausen, A.D. Naik, A. Rotaru, L. Spinu, Y. Garcia, Inorganic Chemistry 49 (2010) 5723.

[9] M.M. Dîrtu, F. Schmit, A.D. Naik, A. Rotaru, J. Marchand-Brynaert, Y. Garcia, International Journal of Molecular Sciences 12 (2011) 5339.

[10] B. Weber, W. Bauer, T. Pfaffeneder, M.M. Dîrtu, A.D. Naik, A. Rotaru, Y. Garcia, European Journal of Inorganic Chemistry 2011 (2011) 3193.

[11] J. Linares, E. Codjovi, Y. Garcia, Sensors 12 (2012) 4479.

[12] A. Bousseksou, J. Nasser, J. Linares, K. Boukheddaden, F. Varret, Journal De Physique I 2 (1992) 1381.

[13] F. Varret, S.A. Salunke, K. Boukheddaden, A. Bousseksou, E. Codjovi, C. Enachescu, J. Linares, Comptes Rendus Chimie 6 (2003) 385.

[14] K. Boukheddaden, J. Linares, E. Codjovi, F. Varret, V. Niel, J.A. Real, *Journal of Applied Physics* 93 (2003) 7103.

[15] Y. Garcia, P.J. van Koningsbruggen, R. Lapouyade, L. Fournes, L. Rabardel, O. Kahn, V. Ksenofontov, G. Levchenko, P. Gütlich, Chemistry of Materials 10 (1998) 2426.
[16] V. Ksenofontov, H. Spiering, A. Schreiner, G. Levchenko, H.A. Goodwin, P. Gutlich, Journal of Physics and Chemistry of Solids 60 (1999) 393.
[17] Y. Garcia, V. Ksenofontov, G. Levchenko, G. Schmitt, P. Gütlich, Journal of Physical Chemistry B 104 (2000) 5045.
[18] P. Gütlich, A.B. Gaspar, V. Ksenofontov, Y. Garcia, Journal of Physics-Condensed Matter 16 (2004) S1087.
[19] J. Jeftic, N. Menendez, A. Wack, E. Codjovi, J. Linares, A. Goujon, G. Hamel, S. Klotz, G. Syfosse, F. Varret, Measurement Science & Technology 10 (1999) 1059.
[20] E. Codjovi, N. Menendez, J. Jeftic, F. Varret, Comptes Rendus De L Academie Des Sciences Serie Ii Fascicule C-Chimie 4 (2001) 181.
[21] A. Rotaru, F. Varret, E. Codjovi, K. Boukheddaden, J. Linares, A. Stancu, P. Guionneau, J.F. Letard, *Journal of Applied Physics* 106 (2009) 053515.
[22] A. Rotaru, J. Linares, F. Varret, E. Codjovi, A. Slimani, R. Tanasa, C. Enachescu, A. Stancu, J. Haasnoot, Physical Review B 83 (2011) 224107.
[23] A. Bhattacharjee, M. Roy, V. Ksenofontov, J.A. Kitchen, S. Brooker, P. Gütlich, European Journal of Inorganic Chemistry (2013) 843.
[24] C.P. Slichter, H.G. Drickamer, J. Chem. Phys. 56 (1972) 2142.
[25] A. Rotaru, J. Linares, E. Codjovi, J. Nasser, A. Stancu, *Journal of Applied Physics* 103 (2008) 07B908.
[26] A. Rotaru, J. Linares, S. Mordelet, A. Stancu, J. Nasser, *Journal of Applied Physics* 106 (2009) 043507.
[27] Y. Konishi, H. Tokoro, M. Nishino, S. Miyashita, Physical Review Letters 100 (2008).
[28] S. Klokishner, J. Linares, F. Varret, Chemical Physics 255 (2000) 317.
[29] G. Levchenko, G.V. Bukin, S.A. Terekhov, A.B. Gaspar, V. Martinez, M.C. Munoz, J.A. Real, Journal of Physical Chemistry B 115 (2011) 8176.
[30] V. Martinez, Z.A. Castillo, M.C. Munoz, A.B. Gaspar, C. Etriard, J.F. Letard, S.A. Terekhov, G.V. Bukin, G. Levchenko, J.A. Real, European Journal of Inorganic Chemistry (2013) 813.
[31] R. Tanasa, A. Stancu, J.F. Letard, E. Codjovi, J. Linares, F. Varret, Chemical Physics Letters 443 (2007) 435.
[32] Y. Garcia, V. Ksenofontov, P. Gütlich, *Hyperfine Interactions* 139 (2002) 543.
[33] P. Gutlich, A.B. Gaspar, Y. Garcia, V. Ksenofontov, Comptes Rendus Chimie 10 (2007) 21.
[34] P.A. Szilagyi, S. Dorbes, G. Molnar, J.A. Real, Z. Homonnay, C. Faulmann, A. Bousseksou, Journal of Physics and Chemistry of Solids 69 (2008) 2681.
[35] A. Tissot, H.J. Shepherd, L. Toupet, E. Collet, J. Sainton, G. Molnar, P. Guionneau, M.L. Boillot, European Journal of Inorganic Chemistry (2013) 1001.
[36] H.J. Shepherd, P. Rosa, L. Vendier, N. Casati, J.-F. Letard, A. Bousseksou, P. Guionneau, G. Molnar, Physical Chemistry Chemical Physics 14 (2012) 5265.
[37] V. Legrand, F. Le Gac, P. Guionneau, J.-F. Letard, Journal of Applied Crystallography 41 (2008) 637.
[38] P. Guionneau, M. Marchivie, Y. Garcia, J.A.K. Howard, D. Chasseau, Physical Review B 72 (2005).
[39] A. Marbeuf, S.F. Matar, P. Negrier, L. Kabalan, J.F. Letard, P. Guionneau, Chemical Physics 420 (2013) 25.
[40] A. Lapresta-Fernandez, M. Pegalajar Cuellar, J. Manuel Herrera, A. Salinas-Castillo, M. del Carmen Pegalajar, S. Titos-Padilla, E. Colacio, L. Fermin Capitan-Vallvey, Journal of Materials Chemistry C 2 (2014) 7292.

[41] Y. Garcia, P.J. vanKoningsbruggen, E. Codjovi, R. Lapouyade, O. Kahn, L. Rabardel, Journal of Materials Chemistry 7 (1997) 857.
[42] Y. Garcia, P.J. van Koningsbruggen, R. Lapouyade, L. Rabardel, O. Kahn, M. Wieczorek, R. Bronisz, Z. Ciunik, M.F. Rudolf, Comptes Rendus De L Academie Des Sciences Serie Ii Fascicule C-Chimie 1 (1998) 523.
[43] M.M. Dîrtu, Y. Garcia, M. Nica, A. Rotaru, J. Linares, F. Varret, *Polyhedron* 26 (2007) 2259.
[44] C.M. Jureschi, J. Linares, A. Rotaru, M.H. Ritti, M. Parlier, M.M. Dîrtu, M. Wolff, Y. Garcia, Sensors (Basel, Switzerland) 15 (2015) 2388.

General Conclusions

The continuous development of new equipment and machinery that require more advanced sensors with improved technical characteristics constitutes the motivation behind the results presented in this thesis. A special class of new sensors is based on spin-crossover materials. The main advantages of these materials, such as the ability to be controlled at the molecular level, color changing during the transition between the two states, hysteresis, and high sensitivity to changes in external perturbing factors, opened up the possibility for new applications: temperature and/or pressure sensors, chemical sensors, memory, displays, fast switching devices. Throughout this thesis both theoretical and experimental studies on the possibility of using these materials in the manufacture of temperature sensors and pressure were presented. Using a Ising-like model, we begin with a theoretical investigation of the role of cooperativity in a SCO system, the interactions of surface molecules with their environment, architecture and size effects. We continued the theoretical study using a Atom Phonon coupling model and showed the efficiency of the parabolic method in solving for the system's Hamiltonian. We also performed experimental studies to point out the thermal and piezo-chromic properties of the SCO compounds $[Fe(hyptrz)]A_2 \cdot H_2O$ and $[Fe(hyetrz)_3]I_2 \cdot H_2O$.

The theoretical studies on the role of a system's cooperativity were carried out using a Ising-like model in combination with a Monte Carlo Entropic Sampling method used to generate all system states. We have shown that behind a multi step transition there are three types of interactions: the short-range interactions, long-range interactions and interactions of surface molecules with their environment. These results are important for the construction of a SCO materials based device. It is also very important to take into account the interactions that can occur between the molecules on the surface with their environment. For example, in the manufacturing process of a SCO based sensor it is important to take into account the interactions that occur between SCO and the support material used to deposit the SCO to, and interactions between SCO and the polymer material used to enclose the SCO material. Interactions between surface molecules and their environment are more important, especially when the system is set up so that the number of molecules at the surface is greater than that of the entire system. We have shown that a 1D system, where the edge only has two molecules, requires a large value of edge interactions in order to play a significant role in SCO system behavior. 2D and 3D systems, where the number of surface molecules is much higher, the SCO system behavior is influenced even for lower values of edge interactions. The influence of edge effect is all the greater as the ratio of molecules on the surface and within the system is higher. These studies were done considering the surface molecules as active molecules.

Important results were obtained from the analysis of the role of system architecture. Considering the same number of molecules we showed that a quadratic system is more cooperative than a rectangular ladder system which in turn is more cooperative than a chain-type system. This is evidenced by the width of the hysteresis loop of each system. It was also revealed that the edge effect shift the transition temperatures to lower values.

Using the Atom Phonon coupling model the results were compared using three different methods of solving the Hamiltonian: mean field approximation, dynamic matrix and the parabolic approximation. Thus we showed that the parabolic approximation method is superior to the approximation of the mean field and that the results obtained by this method are very close to reality. This is because this method uses exact calculation.

The parabolic method leads to the same thermal behavior of the SCO system as that obtained with the dynamic matrix method, especially for small sized system. However, for large

systems, the entropy contribution plays an important role and a close correspondence between results given by these two methods is obtained only for high values of the degeneracy ratio. For example, for N=8, this discrepancy disappears for g higher than 1000, that is when the variation of the entropy at the transition temperature is higher than $R\ln(g) = 57.9$ Joule K^{-1} mol^{-1}. This entropy variation value is common in SCO systems.

Experimental studies were conducted on two SCO compounds: $[Fe(hyptrz)]A_2 \cdot H_2O$ and $[Fe(hyetrz)_3]I_2 \cdot H_2O$ respectively, indicating the thermal and piezo-chromic character of the systems. In the thermal analysis of the external pressure behavior of the first compound, a gas pressure cell was used. This type of cell has the advantage to maintain the hydrostatic nature over the entire range of temperature. Thus it was shown that, by applying an external pressure, the transition temperatures are translated to higher values and the width of the hysteresis loop decreases and eventually disappears after which the transition occurs without hysteresis. The second compound was characterized using several techniques: optical characterization, DSC, Mössbauer spectroscopy and a home-made micromechanical device. We proved the feasibility of pressure detection using a molecular spin crossover based sensor/marker operating at ambient temperature. For the SCO compound $[Fe(hyetrz)_3]I_2 \cdot H_2O$, we obtained a threshold value of the contact pressure of about 30 MPa to irreversibly induce the color change of the molecular material, due to the spin state switching form HS to LS state. Moreover, the possibility of switching back the color using another stimulus (temperature) was demonstrated, making this sensor reusable. As in the previous case, a theoretical investigation in the framework of the Ising-like model has been presented. These results open important perspectives for molecular materials in pressure sensing applications, suggesting the possibility of their insertion in piezo- and thermo-chromic paints that will allow the visual detection of mechanical collisions, a very important issue in the aeronautic and automotive industries.

Taking into account the above mentioned results we proposed a new type of sensor with optical detection that would allow the concomitant detection of both temperature and pressure. This new type of sensor is based on two SCO compounds that exhibit gradual transitions. Considering recent developments in the SCO field this objective could be achievable in the near future.

List of publications

1. **Catalin Maricel Jureschi**, Ionela Rusu, Epiphane Codjovi, Jorge Linares, Yann Garcia, Aurelian Rotaru, *Thermo- and piezochromic properties of [Fe(hyptrz)]A2·H2O spin crossover 1D coordination polymer: Towards spin crossover based temperature and pressure sensors*, Physica B: Condensed Matter, 449 (2014) 47-51.

2. Daniel Chiruta, **Catalin Maricel Jureschi**, Jorge Linares, Yann Garcia, Aurelian Rotaru, *Lattice architecture effect on the cooperativity of spin transition coordination polymers*, Journal of Applied Physics, 115 (2014).

3. Daniel Chiruta, **Catalin Maricel Jureschi**, Jorge Linares, Adrian Graur, Mihai Dimian, Aurelian Rotaru, *Analysis of Architecture Effect on Hysteretic Behavior of 3-D Spin Crossover Nanostructures*, Magnetics, IEEE Transactions on, 50 (2014) 1-4.

4. **Catalin Maricel Jureschi**, Jorge Linares, Aurelian Rotaru, Marie Helene Ritti, Michel Parlier, Marinela M. Dîrtu, Mariusz Wolff, Yann Garcia, *Pressure sensor via optical detection based on a 1D spin transition coordination polymer*, Sensors (Basel, Switzerland), 15 (2015) 2388-2398.

5. Daniel Chiruta, **Catalin Maricel Jureschi**, Jorge Linares, Jamil Nasser, Aurelian Rotaru, *Analysis of spin crossover nanochains using parabolic approximation in the framework of atom–phonon coupling model*, Physica B: Condensed Matter, 476 (2015) 61-70.

6. Daniel Chiruta, **Catalin Maricel Jureschi**, Jorge Linares, Pierre Richard Dahoo, Yann Garcia, Aurelian Rotaru, *On the origin of multi-step spin transition behaviour in 1D nanoparticles*, The European Physical Journal B, 88 (2015) 1-5.

7. **Catalin Maricel Jureschi**, Benjamin-Louis Pottier, Jorge Linares, Pierre Richard Dahoo, Yasser Alayli, Aurelian Rotaru, *Simulation of multi-steps thermal transition in 2D spin-crossover nanoparticles*, Physica B: Condensed Matter, 486 (2016) 160-163.

8. Jorge Linares, **Catalin Maricel Jureschi**, Ayoub Boulmaali, Kamel Boukheddaden, *Matrix and size effects on the appearance of the thermal hysteresis in 2D spin crossover nanoparticles*, Physica B: Condensed Matter, 486 (2016) 164-168.

9. Damir A. Safin, Koen Robeyns, Maria G. Babashkina, Yaroslav Filinchuk, Aurelian Rotaru, **Catalin Maricel Jureschi**, Mariusz P. Mitoraj, James Hooper, Mateusz Brela, Yann Garcia, *Polymorphism driven optical properties of an anil dye*, Crystengcomm, 18 (2016) 7249-7259.

10. **Catalin Maricel Jureschi**, Jorge Linares, Ayoub Boulmaali, Pierre Dahoo, Aurelian Rotaru, Yann Garcia, *Pressure and Temperature Sensors Using Two Spin Crossover Materials*, Sensors, 16 (2016) 187.

11. **Catalin Maricel Jureschi**, Jorge Linares, Aurelian Rotaru, Yann Garcia, *Multi-Step in 3D Spin Crossover Nanoparticles Simulated by an Ising Model Using Entropic Sampling Monte Carlo Technique*, Magnetochemistry, 2 (2016) 13.

12. Jorge Linares, **Catalin Maricel Jureschi**, Kamel Boukheddaden, *Surface Effects Leading to Unusual Size Dependence of the Thermal Hysteresis Behavior in Spin-Crossover Nanoparticles*, Magnetochemistry, 2 (2016) 24.

13. **Catalin Maricel Jureschi**, Jorge Linares, Pierre-Richard Dahoo, Yasser Alayli, *Monte Carlo entropic sampling applied to Ising-like model for 2D and 3D systems*, Journal of Physics: Conference Series, 738 (2016) 012051.

14. Jorge Linares, Daniel Chiruta, **Catalin Maricel Jureschi**, Yasser Alayli, C. O. Turcu, Pierre-Richard Dahoo, *Simulations of Edge Effect in 1D Spin Crossover Compounds by Atom-Phonon Coupling Model*, Journal of Physics: Conference Series, 738 (2016) 012052.

15. Salim Guerroudj, Rafael Caballero, Francisco De Zela, **Catalin Maricel Jureschi**, Jorge Linares and Kamel Boukheddaden - *Monte Carlo - Metropolis Investigations of Shape and Matrix Effects in 2D and 3D Spin-Crossover Nanoparticles*, Journal of Physics Series Conference, 738 (2016) 012068.

List of conferences

1. **Catalin Maricel Jureschi**, Adrian Graur, Gelu Rotaru, Jorge Linares, Yann Garcia, Aurelian Rotaru**,** - 6th International Workshop on Multi-Rate Processes and Hysteresis (MURPHYS 2012), 21-24 May 2012, Suceava, Romania

2. **Catalin Maricel Jureschi**, Epiphane Codjovi, Jorge Linares, Yann Garcia, Aurelian Rotaru **-** 2nd International Conference on Advanced Complex Inorganic Nanomaterials – ACIN 2013, 15-19 July 2013, Namur

3. Daniel Chiruta, **Catalin Maricel Jureschi**, Jorge Linares, Yann Garcia, Aurelian Rotaru - DdR MCM2-Magnetism and molecular switches, 10-12.12.2013, Dourdan

4. Daniel Chiruta, **Catalin Maricel Jureschi**, Jorge Linares, Adrian Graur, Mihai Dimian, Aurelian Rotaru - IEEE International Magnetics Conference (INTERMAG 2014), 4-8 May 2014, Dresden, Germany

5. Ionel Rusu, **Catalin Maricel Jureschi,** Corneliu Octavian Turcu, Aurelian Rotaru - 10th International Conference on Physics of Advanced Materials – ICPAM 2014, 22-28 September 2014, Iasi, Romania

6. Daniel Chiruta, **Catalin Maricel Jureschi**, Jorge Linares, Pierre-Richard Dahoo, Yann Garcia, Aurelian Rotaru - 10th Internation Symposium on Hysteresis Modeling and Micromagnetics (HMM), 18/-20 May 2015 Iasi, Romania